UNIVERSITY OF CALIFORNIA

Santa Barbara

Tuning The Optical, Charge Injection, and Charge Transport Properties of Organic Electronic Devices

A dissertation submitted in partial satisfaction of the
requirements for the degree Doctor of Philosophy
in Chemistry

by

Peter Zalar

Committee in charge:
Professor Thuc-Quyen Nguyen, Chair
Professor Guillermo C. Bazan
Professor Horia Metiu
Dr. Alexander Mikhailovsky, Associate Researcher
Professor Fred Wudl

June 2014

The dissertation of Peter Zalar is approved.

Guillermo Carlos Bazan

Horia Metiu

Alexander Mikhailovsky

Fred Wudl

Thuc-Quyen Nguyen, Committee Chair

May 2014

Tuning The Optical, Charge Injection, and Charge Transport Properties of Organic Electronic Devices

by

Peter Zalar

ACKNOWLEDGEMENTS

It is at this point in the thesis where it is required to give a final word of acknowledgment to those people which made the work contained herein possible, either in a practical or metaphysical way. Naturally, it is entirely possible (and likely) that some people were forgotten in the following text, and for this I apologize in advance.

I feel it is necessary to first thank the University of California, Santa Barbara (UCSB), for affording me a range of opportunities throughout both my bachelor and doctoral studies. During my bachelor studies, through the Materials Research Laboratory, I had the opportunity to participate in an international research exchange; joining the research group of Professor E. W. Meijer at The Eindhoven University of Technology (TU/e). I mainly attribute this experience as being the primary driving force for my interest in even pursuing any kind of post-graduate studies. The interaction with students, professors, and the immense amount of knowledge I gained there is something I strongly cherish. It is my hope that future University of California and specifically UCSB students will continue to have access to these powerful and wonderful programs.

I also wish to acknowledge the quality and availability of all the shared facilities at UCSB. The instrumentation and staff there really elevate the quality and rate at which researchers can do their work. In this regard, not many universities, even those who are perceived as more highly ranked or even more prestigious can even compare.

I would like to thank my advisor, Professor Thuc-Quyen Nguyen for giving me the opportunity to perform my doctoral studies in her group. Professor Quyen always made sure that I had the resources and facilities to perform my work to the fullest; this is a luxury that many students, research groups, and universities unfortunately cannot enjoy. I will always remember her for her absolute support of her students and her incredible sixth sense on recruiting students to formulate a group of compatible and friendly people. I'm also grateful for when Professor Quyen sent me to the group of Professor Paul W. M. Blom at the University of Groningen. There I learned an incredible amount about how to fabricate and test organic electronic devices. In addition, I also met a lot of great people there who I consider great friends to this day.

Next, I would like to thank my dissertation committee, who has been with me from the beginning to the end of my studies: Professor Guillermo C. Bazan, Professor Horia Metiu, Associate Researcher Alexander Mikhailovsky, and Professor Fred Wudl. I'm honored to have such a distinguished group of people in my dissertation committee. I’m grateful that you all have taken time out of your busy schedules to take part in all stages of my qualification to a doctorate.

I'm thankful for the chance to collaborate with the groups of Professor Guillermo C. Bazan and Professor Fred Wudl on many interesting projects, some of which do not even appear in this document. However, without their material and intellectual support, much of this work wouldn't have even been possible. In regards to these collaborations, I wish to specifically thank Professor Lei Ying (now at South China

University of Technology), Professor Gregory C. Welch (now at Dalhousie University), Dr. Zhao Chen, Dr. Toan V. Pho, and Dr. Zachary B. Henson.

I want to also collectively thank all members of the Nguyen Group, past and present - a list of people that is too long to mention here. Specifically, I owe a lot to Dr. Chunki Kim, Dr. Martijn Kuik, and Dr. Yuan Zhang. Chunki was an excellent motivator, who sometimes helped give me the optimism and determination to push through difficulties and fatigue. He was also an excellent teacher, asking me difficult questions to challenge me and broaden my knowledge. In Yuan, I found a friend and colleague who helped give me a strong basis in device fabrication and device physics. His sense of humor always lightens the mood in the office and is something I will truly miss when I leave UCSB. For nearly the first two years of my PhD, Chunki, Yuan, and myself had lunch and dinner together almost every day; a strong testament to the bond and friendship that can be had between coworkers. I first met Martijn during my visit in Groningen. It seemed that almost immediately, Martijn and I became friends. This friendship naturally translated well in our work, where we worked closely on several projects that resulted in high quality publications that I am very proud of. Martijn was an excellent teacher, acting sometimes as a "coach", giving me advice on my work, on communicating my work, and on the basketball court. I truly believe that in Martijn I have found a lifelong friend.

I also want to specially acknowledge my office-mates through the years: Dr. Yuan Zhang, Dr. Chunki Kim, Dr. Mananya Tantiwiwat, Dr. Daniel Salvador Tordera, Daniel Kamkar, Zhi Li, and Hung Phan. I know that our office sometimes had the reputation of being social and rowdy, but we all found a way to output a lot of good work. I will really miss you guys and wish you the greatest success in your career and life.

I believe it’s also important to acknowledge my friends outside of the group. If you’re reading this, I think you should know who you are. I feel very lucky to have your love and encouragement during the course of my studies.

In saving the most important for last; I wish to acknowledge my parents. Their unconditional love is the most important feeling and means the entire world to me. Knowing you have unwavering support and love is a valuable asset in life.

VITA OF PETER ZALAR

MAY 2014

Education	Sep. 2010 – Jun. 2014 University of California, Santa Barbara Doctor of Materials Chemistry Advisor: Professor Thuc-Quyen Nguyen, Department of Chemistry & Biochemistry Sep. 2006 – Mar. 2010 University of California, Santa Barbara Bachelor of Science, Chemistry
Professional Experience	*Mar. 2010 – Present* Graduate Student Researcher - **University of California, Santa Barbara** Center for Polymers and Organic Solids Topic: Investigation of the electronic and optical properties of π-conjugated polymers and small molecules, and quantum dots for use in organic electronic devices such as light-emitting diodes, solar cells, and field-effect transistors. Advisor: Professor Thuc-Quyen Nguyen, Department of Chemistry & Biochemistry Collaborations: Professor Guillermo C. Bazan, Professor Fred Wudl, Professor Alan Heeger (Nobel Prize Laureate), Mitsubishi Chemical Company (Japan) *Mar. 2011 – Apr. 2011* Visiting Researcher – **University of Groningen (RuG), The Netherlands** Zernike Institute for Advanced Materials Topic: Device physics of π-conjugated polyelectrolytes and Lewis acid modified polymers. Advisor: Professor Paul W. M. Blom, Department of Molecular Electronics & Director Max Planck Institute for Polymer Research (Mainz, Germany) *Jun. 2008 – Sep. 2008* Visiting Researcher - **Eindhoven University of Technology (TU/e) The Netherlands** Institute for Complex Molecular Systems Topic: Synthesis and study of supramolecular and charge transfer properties in self-assembled π-conjugated porphyrin derivatives. Advisor: Professor E. W. (Bert) Meijer, Department of Chemical Engineering & Chemistry

Journal Publications ***(Peer Reviewed)***

1. “Effects of Processing Conditions on the Recombination Reduction in Small Molecule Bulk Heterojunction Solar Cells,” Zalar, P.; Kuik, M., Ran, N. A.; Love, J. A.; Nguyen, T.-Q. *Adv. Energy Mater.* **2014**, doi: 10.1002/aenm.201400438.

2. “Effect of Backbone Regioregularity on the Structure and Orientation of a Donor-Acceptor Semiconducting Copolymer,” Perez, L. A.; Zalar, P.; Ying, L.; Schmidt, K.; Toney, M. F.; Nguyen, T.-Q.; Bazan, G. C.; Kramer, E. J. *Macromolecules*, **2014**, *47*, 1403-1410.

3. “Increased Mobility Induced by Addition of a Lewis Acid to a Lewis Basic Conjugated Polymer,” Zalar, P.; Kuik, M.; Henson, Z. B.; Zhang, Y.; Sharenko, A.; Bazan G. C.; Nguyen, T.-Q. *Adv. Mater.* **2014**, *26*, 724-727.

4. “A Structure-Property Performance Investigation of Perylenediimides as Electron Accepting Materials in Organic Solar Cells,” Guide, M.; Pla, S.; Sharenko, A.; Zalar, P.; Fernández-Lázaro, F.; Sastre-Santos, Á.; Nguyen, T.-Q. *Phys. Chem. Chem. Phys.* **2013**, *15*, 18894-18899.

5. “Towards Environmentally Friendly Processing in Molecular Semiconductors,” Henson, Z. B.; Zalar, P.; Chen, X.-F.; Welch, G. C.; Nguyen, T.-Q.; Bazan, G. C. *J. Mater. Chem. A.* **2013**, *1,* 11117-11120.

6. “High Light Intensity Effects on Nanoscale Open-Circuit Voltage for Three Common Donor Materials in Bulk Heterojunction Solar Cells,” Zhang, Y.; Dang, X.-D.; Kuik, M.; Cowan, S. R.; Zalar, P.; Kim, C.; Nguyen, T.-Q. *Energy Environ. Sci.* 2013, *6*, 1766-1771.

7. “Optimization of Energy Levels by Molecular Design: Evaluation of Bis-Diketopyrrolopyrrole Molecular Donor Materials for Bulk Heterojunction Solar Cells,” Walker, B.; Liu, J.-H.; Kim, C.; Welch, G. C.; Park, J. K.; Lin, J.; Zalar, P.; Proctor C. M.; Seo, J.-H.; Bazan G. C.; Nguyen, T.-Q. *Energy Environ. Sci.* **2013**, *6*, 952-962.

8. “All Cojugated Triblock Polyelectrolytes,” Ying, L.; Zalar, P.; Collins, S. D.; Chen, Z.; Mikhailovsky, A. A.; Nguyen, T.-Q.; Bazan, G. C. *J. Am. Chem. Soc.* **2012**, *24*, 6496-6501.

9. “DNA Interlayers Enhance Charge Injection in Organic Field-Effect Transistors,” Zhang, Y.; Zalar, P.; Kim, C.; Collins, S.; Bazan, G. C.; Nguyen, T.-Q. *Adv. Mater.* **2012**, *24*, 4255-4260.

10. “Color Tuning in Polymer Light-Emitting Diodes with Lewis Acids,” Zalar, P.; Henson, Z. B.; Welch, G. C.; Bazan, G. C.; Nguyen, T.-Q. *Angew. Chem. Int. Ed.* **2012**, *51*, 7495-7498.

11. “Regioregular Pyridal[2,1,3]thiadiazole pi-Conjugated Copolymers,” Ying, L.; Hsu, B. B. Y.; Zhan, H. M.; Welch, G. C.; Zalar, P.; Perez, L. A.; Kramer, E. J.; Nguyen, T.-Q.; Heeger, A. J.; Wong, W. Y.; Bazan, G. C. *J. Am. Chem. Soc.* **2011**, *133*, 18538-18541.

12. “Optical and Charge Transport Properties of Water/Alcohol-Soluble Quinacridone Derivatives for Application in Polymer Light Emitting Diodes,” Zalar, P.; Pho, T. V.; Garcia, A.; Walker, B.; Walker, W.; Wudl, F.; Nguyen, T.-Q. *J. Phys. Chem. C.* **2011**, *115*, 17533-17539.

13. “DNA Electron Injection Interlayers for Polymer Light-Emitting Diodes,” Zalar, P.; Kamkar, D.; Naik, R.; Ouchen, F.; Grote, J. G.; Bazan, G. C.; Nguyen T.-Q. *J. Am. Chem. Soc.* **2011**, *133*, 11010-11013.

14. “Controlling Ion Motion in Polymer Light Emitting Diodes Containing Conjugated Polyelectrolyte Electron Injection Layers,” Garcia, A.; Bakus, R. C.; Zalar, P.; Hoven, C. V.; Brzezinski, J. Z.; Nguyen, T.-Q. *J. Am. Chem. Soc.* **2011**, *133*, 2492-2498.

15. “Electron Injection Barrier Reduction for Organic Light Emitting Devices by Quinacridone Derivatives,” Pho, T. V.; Zalar, P.; Garcia, A.; Nguyen, T.-Q.; Wudl, F. *Chem. Commun.* **2010**, *46*, 8210-12.

16. “Effect of Thermal Annealing on Polymer Light Emitting Diodes Utilizing Cationic Conjugated Polyelectrolytes as Electron Injection Layers,” Lin, C.-Y.; Garcia, A.; Zalar, P.; Brzezinski, J. Z.; Nguyen, T.-Q. *J. Phys. Chem. C.* **2010**, *114*, 15786-15790.

17. “Nanoscale Phase Separation and Photovoltaic Efficiency in Solution-Processed, Small-Molecule Bulk Heterojunction Solar Cells,” Walker, B.; Tamayo, A. B.; Dang, X. D.; Zalar, P.; Seo, J. H.; Garcia, A.; Tantiwiwat, M.; Nguyen, T.-Q. *Adv. Funct. Mater.* **2009**, *19*, 3063-3069.

Patents

1. “Processing Additive For Single-Component Solution Processed Organic Field-Effect Transistors,” Bazan, G. C.; Nguyen, T.-Q.; Ying, L.; Zalar, P.; Zhang, Y. U.S. Patent App. 13/869,498.

2. “Conjugated Copolymers Chiral Side Chain For Organic Thin Film Transistors,” Bazan, G. C.; Nguyen, T.-Q.; Ying, L.; Zalar, P. U.S. Patent App. 13/869,533.

Book Chapters	1. Zalar, P.; Nguyen, T.-Q. Charge Injection Mechanism in PLEDs and Charge Transport in Conjugated Polyelectrolytes. In *Conjugated Polyelectrolytes: Fundamentals and Applications*; Liu, B. and Bazan, G. C. Eds.; Wiley: Weinheim, **2013**
Selected Presentations	1. "Color Tuning in Polymer Light-Emitting Diodes With Lewis Acids," Poster, Electronic Processes in Organic Materials. **Lucca, Italy**, June 3-8, 2012. 2. "Efficient Electron Injection in OLEDs Utilizing Water/Alcohol Soluble Quinacridone Derivatives," Oral Presentation, International Workshop for Advanced Materials Science and Nanotechnology. **Hanoi, Vietnam**, November 10, 2010. 3. "Efficient Electron Injection in OLEDs Utilizing Water/Alcohol Soluble Quinacridone Derivatives," Oral Presentation, South China University of Technology Workshop. **Guangzhou, People's Republic of China**, October 13, 2010.
Teaching	- CHEM 153 "Advanced Analytical Techniques" (Spring 2010, Spring 2011) - CHEM 116BL "Inorganic Synthesis and Physical Characterization Laboratory" (Fall 2014) - CHEM 116AL "Quantitative Analytical and Physical Methods Laboratory" (Winter 2014) - CHEM 116CL "Advanced Physical Chemistry Laboratory" (Spring 2014)

ABSTRACT

Tuning The Optical, Charge Injection, and Charge Transport Properties of Organic Electronic Devices

by

Peter Zalar

Since the early 1900's, synthetic insulating polymers (plastics) have slowly taken over the role that traditional materials like wood or metal have had as basic components for construction, manufactured goods, and parts. Plastics allow for high throughput, low temperature processing, and control of bulk properties through molecular modifications. In the same way, π-conjugated organic molecules are emerging as a possible substitute for inorganic materials due to their electronic properties. The semiconductive nature of π-conjugated materials make them an attractive candidate to replace inorganic materials, primarily due to their promise for low cost and large-scale production of basic semiconducting devices such as light-emitting diodes, solar cells, and field-effect transistors.

Before organic semiconductors can be realized as a commercial product, several hurdles must be cleared. The purpose of this dissertation is to address three distinct properties that dominate the functionality of devices harnessing these materials:

(1) optical properties, (2) charge injection, and (3) charge transport. First, it is shown that the electron injection barrier in the emissive layer of polymer light-emitting diodes can be significantly reduced by processing of novel conjugated oligoelectrolytes or deoxyribonucleic acid atop the emissive layer. Next, the charge transport properties of several polymers could be modified by processing them from solvents containing small amounts of additives or by using regioregular and enantiopure chemical structures.

It is then demonstrated that the optical and electronic properties of Lewis basic polymer structures can be readily modified by interactions with strongly electron-withdrawing Lewis acids. Through red-shifted absorption, photoluminescence, and electroluminescence, a single π-conjugated backbone can be polychromatic. In addition, interaction with Lewis acids can remarkably *p*-dope the hole transport of the parent polymer, leading to a two-orders of magnitude increase in the hole mobility. Finally, the hole, electron, and double carrier transport in solar cell devices are studied in a bid to examine the correlations between bulk morphologies and free carrier recombination.

The sum of these works help to create new pathways for the synthesis and design of new π-conjugated materials and device architectures. All of this is in hopes of achieving higher performance and more stable devices to rival inorganic systems.

TABLE OF CONTENTS

LIST OF FIGURES

1.0 Introduction

1.1 Organic Semiconductors

The story of organic semiconductors begins primarily with a breakthrough in 1977, when Heeger, MacDiarmid, and Shirakawa demonstrated that polyacetylene's conductivity could be controlled over a range of 11 orders of magnitude by chemical doping using a range of halogens.[1] Eventually, Heeger, MacDiarmid, and Shirakawa were awarded with the Nobel Prize in Chemistry in 2000 for their contributions.[2] Before this discovery, most research focused on 'curious' organic crystals and dyes such as anthracene and perylene which displayed surprising properties such as electroluminescence.[3–8] As a result of these discoveries and early work, molecules based on alternating single and double bonds – conjugated materials – comprise the framework through which conducting and semi-conducting organic materials are now synthesized. Technologies based on this framework now makes up a nearly \$8.2 billion dollar industry that continuously dazzles the public mind with new futuristic products.[9]

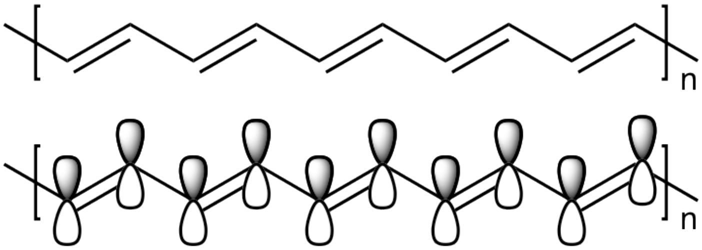

Figure 1.1 The chemical structure and organization of *p*-orbitals in polyactylene.

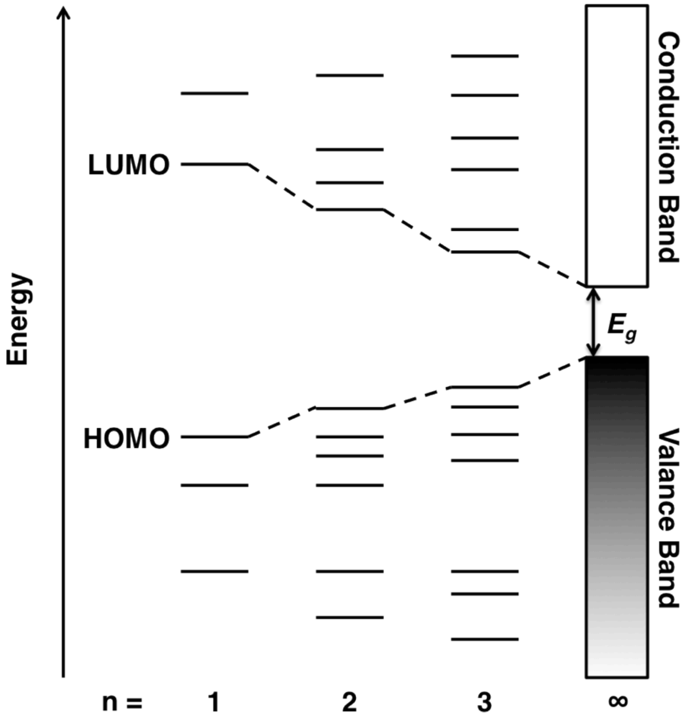

Figure 1.2 Schematic showing the (frontier) energy levels of oligothiophenes with n = 1, 2, 3, and ∞. Adapted from reference 10.

Conjugated systems are by definition, a delocalization of electrons through a system of overlapping *p*-orbitals.[11] This concept is demonstrated in Figure 1.1, using the simplest of π-conjugated systems - polyactylene.[12–14] Interestingly, the electronic structures of conjugated systems have a lot in common with inorganic semiconductors. The electrons in both systems are not organized in discrete energy levels (*quanta*), but are instead distributed in bands. A classic example of this concept is the calculated energy levels of oligothiophenes.[10] As the number of thiophene units increases, the number of energetic states in the highest occupied molecular orbital (HOMO) and lowest unoccupied molecular orbital (LUMO) increases to the point where discrete levels no longer exist forming what would be analogous to a conduction and valance band in inorganic semiconductors. This is conceptually shown in Figure 1.2. The difference in energy between the conduction and valance band is called the 'band-gap', E_g. The E_g is estimated from the absorption and emission from the π to π^* orbitals along the conjugated backbone. The E_g of organic semiconductors is typically between one and four eV, giving rise to their semiconducting nature.

Modern synthetic chemistry allows for nearly limitless modification of chemical structure, giving researchers incredible control over the band gap and thus the electronic properties and function of the organic semiconductor. The notion of band gap control and thus electronic structure control in π-conjugated materials is the basis by which molecular design and device design begins.[15,16]

1.2 Charge Transport in Organic Semiconductors

Inorganic semiconductors are advantageous because of the variety of properties they have such as their tunable conductivities, ability to form depletion regions, ease of doping, and the possibility to absorb or emit light.[17] The main difference between inorganic semiconductors and organic semiconductors lies in the presence of long-range order and strong electronic coupling. This difference manifests itself in the stark difference in charge carrier mobility in pure inorganic semiconductors (10^{-1} m^2/Vs) versus organic semiconductors ($10^{-3} – 10^{-8}$ m^2/Vs).

While inorganic semiconductors are often held together by strong covalent interactions, organic semiconductors are held together by weak Van der Waals forces. This weak electronic coupling between molecules results in an enhanced sensitivity to defects and impurities that create a significant amount of structural and energetic disorder. Sources of this energetic disorder are typically attributed to synthetic impurities and twists or kinks in the molecular structures. This energetic disorder strictly limits the charge-carrier mobilities of these materials and thus the ultimate performance of devices that are based on them. Consequently, charge transport models developed for crystalline inorganic semiconductors break down and do not apply to disordered organic systems.

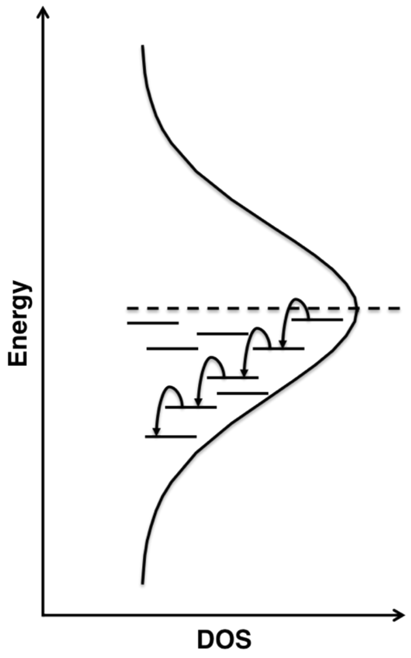

Figure 1.3 Gaussian density of states (GDOS) containing localized sites. The hopping and relaxation process is here shown for electrons.

Since organic semiconductors do not have well-defined three-dimensional lattices, the localized states in the HOMO or LUMO play a primary role in outlining the underlying transport mechanism. While attempting to understand how conduction occurs in extremely impure inorganic semiconductors, Mott and Conwell proposed charge carriers must "hop" between localized states – absorbing and emitting phonons between successive hops.[18,19] This mechanism for conduction was later applied to organic semiconductors by Bässler in 1993.[20] Bässler proposed that the landscape of energetic sites that carriers hop between could be approximated using a Gaussian density of states (GDOS). This energetic landscape was primarily inspired by the absorption spectra of amorphous conjugated polymers, such as substituted polyphenylene vinylenes. This idea is schematically shown in Figure 1.3. As a consequence of this work, one can generalize that organic semiconductors with higher charge carrier mobilities have narrower GDOS widths, meaning that the energetic barrier between hopping sites is lower.[20]

Recently, researchers have expanded on the GDOS basis laid by Bässler by developing the extended Gaussian disorder model (EGDM), which takes into account carrier density (ρ) dependence of the carrier mobility while still including the temperature (T) and electric field dependence (E), thus $\mu(T,E,\rho)$.[21] It is evident from the work of Blom *et al.* that this carrier density dependence of mobility cannot be neglected.[22] With the EGDM, a nearly complete description of the carrier density, temperature, and electric field in disordered organic semiconductors can be achieved.[21]

1.3 Application of Organic Semiconductors

Organic semiconductors, owing to their properties such as optical transparency, low mobilities, and ease of low-cost and large-scale processing, have primarily found a niche in semiconducting device classes including light-emitting diodes (LEDs), solar cells, and field-effect transistors (FETs). Before discussing device structures and device fabrication, it is imperative to remember that the energetic positions of the HOMO and LUMO of the π-conjugated material that is used in as the active material in these devices determines the function of the device processed from it. For example, for polymer LEDs, chemical synthesis of various structures enables the tuning of emission maxima ($\lambda_{e\text{-}max}$) over the virtually the entire visible spectrum.

With classic structures like poly(9,9-di-n-octylfluorenyl-2,7-diyl) (PFO, $\lambda_{e\text{-}max}$ = 417 nm), poly[(9,9-di-n-octylfluorenyl-2,7-diyl)-alt-(benzo[2,1,3]thiadiazol-4,8-diyl)] (F8BT, $\lambda_{e\text{-}max}$ = 515 nm), and poly[2-methoxy-5-(2-ethylhexyloxy)-1,4-phenylenevinylene] (MEH-PPV, $\lambda_{e\text{-}max}$ = 554 nm) the fabrication of full color displays are possible.[15] These materials are desirable for LED applications primarily because of their band gaps and high photoluminescence quantum yields. Figure 1.4 illustrates the variety of band gaps that can be realized through chemical modification.

Figure 1.4 Volumetric flasks containing various organic semiconductors for light-emitting diode applications. This image is copyright Cambridge Display Technologies.

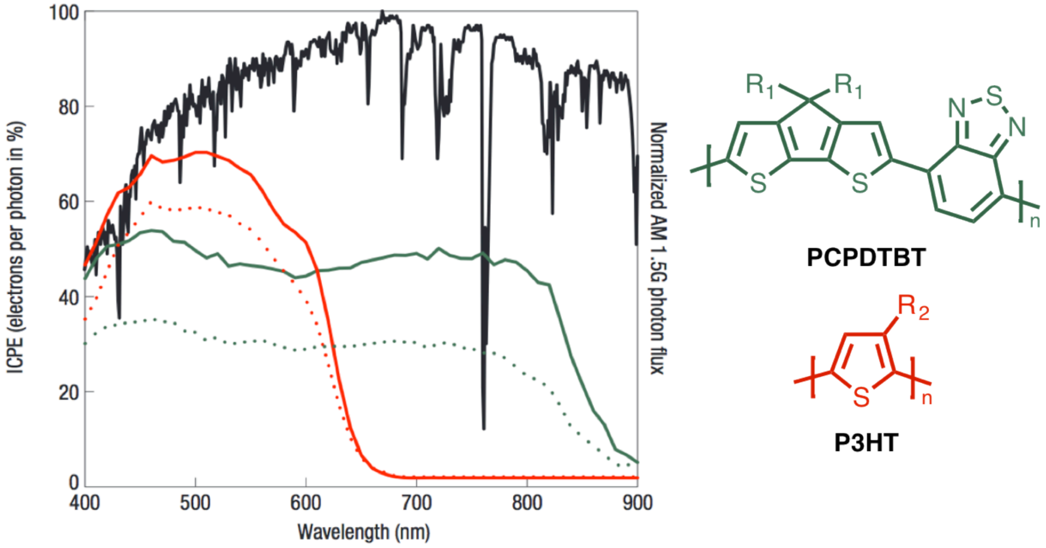

Figure 1.5 Internal photon collection efficiency (IPCE) versus wavelength for P3HT (red) and PCPDTBT (green) based organic solar cells. By lowering of the band gap, more effective overlap with the solar spectrum can be achieved. The result is higher short-circuit currents and thus higher efficiencies. R_1 = 2-ethylhexyl and R_2 = n-hexyl. This figure was adapted from reference 23.

However, materials designed for LEDs are typically unsuitable for solar cell applications, due to their poor absorption overlap with the air mass 1.5 (AM1.5G) solar spectrum. This concept was clearly demonstrated by Peet *et al.* where short-circuit currents of organic bulk heterojunction (BHJ) solar cells were significantly improved by extending the absorption overlap of the π-conjugated system with the solar spectrum by lowering the band gap (Figure 1.5). BHJ solar cells were fabricated using poly(3-hexylthiophene-2,5-diyl) (P3HT) or poly[2,6-(4,4-bis-(2-ethylhexyl)-4H-cyclopenta[2,1-b;3,4-b′]dithiophene)-alt-4,7(2,1,3-benzothiadiazole)] (PCPDTBT) as the electron donor materials blended with 6,6]-Phenyl C61 butyric acid methyl ester (PCBM) as the electron acceptor material.[23] Still, while PCPDTBT found application in solar cells, the optical gap and the quantum yield are far too low for LEDs.

For organic FETs, the energetic positions of the HOMO and LUMO and also the optical gap have a significant influence on whether the transistor operates in the *p*-channel, *n*-channel, or ambipolar modes.[24–26] By modifying the energetic position of the HOMO or LUMO relative to the source electrode (typically Au), the injection of holes or electrons can be more, less, or equally favorable.[24] In a *p*-channel transistor, holes are readily injected but electrons are not. The converse is true in the *n*-channel device. For the ambipolar device, both carriers are readily injected. Control over the operation mode of the transistor enables the fabrication of more complex circuits and functional devices.

A. Organic Light Emitting Diodes

Organic LEDs (OLEDs) have arguably been the main driving force for early research into organic semiconductors since Tang and Van Slyke demonstrated the first OLED device in 1987 at Eastman Kodak.[27,28] Shortly after, the discovery of electroluminescence in polyphenylene vinylenes in 1990 further boosted research efforts.[29,30] The standard and very basic device structure for a single layer OLED is shown in Figure 1.6. The device consists of a patterned transparent conductive oxide (TCO) atop a glass substrate. The most used TCO is indium-tin-oxide and it acts the anode for the device. Atop the anode, a light-emitting material film is deposited either by solution or vacuum methods with a thickness on the nanometer length scale. Finally, a low work function metal such as barium or calcium or an inorganic salt such as lithium fluoride serves as the cathode.[30] Usually a capping layer of aluminum is used to slow oxidation of the cathode to extend device lifetimes.

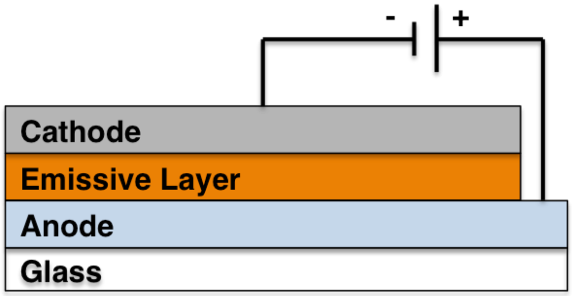

Figure 1.6 The basic device structure of a single-layer organic light-emitting diode.

As discussed earlier, the emissive layer will determine the color of the light output. Three main processes, however, will govern the electrical performance of the device. These three processes are charge injection, charge transport, and charge recombination.[31] The efficiency of these processes will depend on the energetics of the emissive layer, the charge transport properties of the emissive layer, and the choice of anode and cathode. To achieve high efficiencies, one needs an emissive layer with a high photoluminescent quantum yield and balanced and un-trapped electron and hole transport. Upon the application of a positive bias, holes will be injected from the anode and electrons will be injected from the cathode. These charges will then successively hop through the HOMO (holes) and LUMO (electrons) until they meet each other to recombine and produce light at the wavelength characteristic of the band gap of the emissive layer. Classic materials for this purpose are the ones mentioned above, PFO (blue light), F8BT (green light), and MEH-PPV (red light).[32]

Modern vacuum processed OLEDs benefit from the usage of several doped layers and phosphorescent emitters, achieving internal-quantum-efficiencies (IQEs) that approach unity.[33] Fabricating multilayer structures is less feasible in solution processed OLEDs because of limitations on the availability of solution processable dopants and difficulties of processing multilayers atop one another from solution. For this reason, polymer LEDs are usually made using only of a hole-transporting layer. In later chapters, this basic diode structure forms the basis for fundamental studies of the electronic material properties of new materials. By modeling the current an understanding of the carrier mobility and trapping behavior can be readily determined.

B. Organic Solar Cells

Photon absorption in organic materials typically results in the formation of tightly bound electron-hole pairs that can only be separated at energies larger than *k*T.[34] Inspired by the natural process of photosynthesis, one can use a donor-acceptor system to effectively split these electron and hole pairs. This splitting of the exciton is made relatively easy because the transfer process is energetically favorable. This is due to the energetic offset between the electron donor (low electron affinity) and the electron acceptor (high electron affinity). This electron transfer process is shown in Figure 1.7.

In 1986, C. W. Tang and coworkers successfully made the first solar cell by taking advantage of this donor-acceptor methodology.[28,35,36] They fabricated bilayer cells *in vacuo* using copper phtalocyanine as the electron donor and perelyne tetracarboxylic acid as the electron acceptor. The final power conversion efficiency was only 1%. This is mostly due to the fact that harvestable excitons only exist at the small interface of the bilayer formed by the two materials. Nonetheless, this proof of concept paved the way to all modern research on this topic. The next big discovery for organic solar cell happened in 1995 when A. J. Heeger and coworkers invented the BHJ solar cell.[37–39] In this type of device, an electron donor and electron acceptor are mixed in solution and then spin-coated atop a transparent anode. This results in an intimately mixed network of donor and acceptor materials, giving many more effective interfaces than afforded by the bilayer configuration. Presently, this class of solar cell device structure is yielding power conversion efficiencies of ~10%.[40]

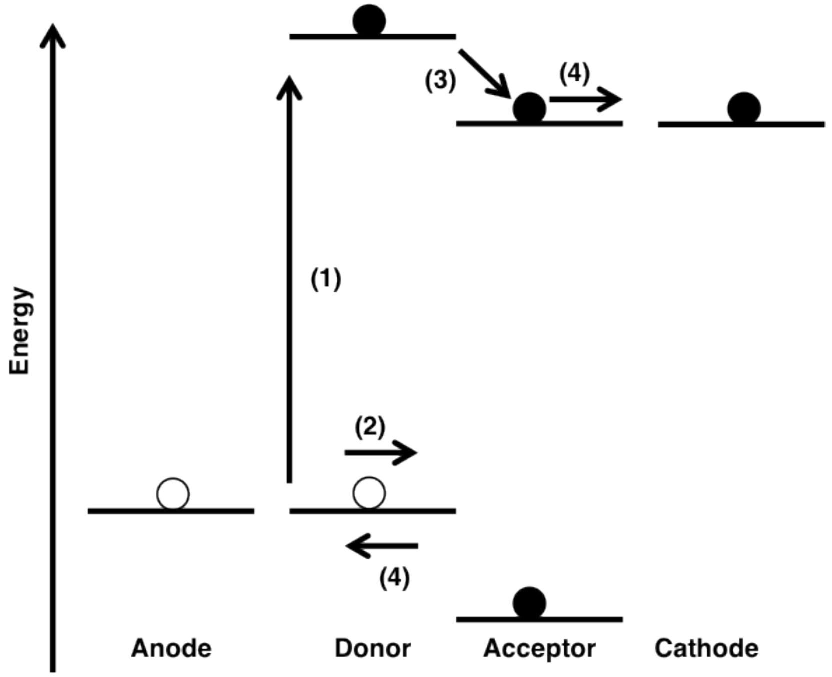

Figure 1.7 The basic device structure and operation mechanism of an organic solar cell, the solid circles are electrons and the open circles are holes. The processes are (1) photon absorption/exciton generation, (2) diffusion of an exciton to the donor-acceptor interface, (3) electron transfer, and (4) diffusion of free charges to the electrodes. The operation of an OLED can be considered as the reverse of these processes.

The first step in an organic solar cell's operation consists of absorption of a photon by the electron donor material (Figure 1.7, process (1)).[41] This event results in the promotion of an electron from the donor's HOMO to its LUMO. The probability of the absorption event of an incoming photon with a certain energy is governed by the band gap (minimum photon energy) and oscillator strength of the electron donor. The absorption of excess energy results in rapid relaxation to the lowest LUMO energy, resulting in heat loss. Due to the small dielectric constant of organic materials, the exciton that forms then has to rapidly find the electron acceptor (2) – hopefully resulting in the separation of charges (3).[42] With the help of the device's internal electrical field, the separated charges (electron and hole) are able to overcome their Coulombic attraction and be transported to the electrodes (4).

The device structure of organic BHJ solar cells is largely the same as the LED structure shown in Figure 1.6. The donor:acceptor blend takes the place of the emissive layer. Typical electron donor materials have ranged from typical light-emitting diode polymers discussed earlier, like MEH-PPV, PFO, F8BT, but also includes polythiophenes. In short, any conjugated molecule with suitable energy levels relative to the chosen electron acceptor is suitable for use in an organic solar cell. The most ubiquitous electron acceptor in organic solar cells has been chemical derivatives of fullerenes. Fullerene derivatives are ideal because of their excellent solubility in common organic solvents and electron mobility. The most used fullerene derivative in academic and industrial research has been [6,6]-phenyl-C_{61}-butyric acid methyl ester – synthesized by J. C. Hummelen in the group of Professor Fred Wudl in 1995 at UCSB.[43]

C. Organic Field-Effect Transistors

Even though FETs were first patented in 1925,[44] it took many years before they were actually industrially produced.[45] Metal-oxide (or metal-insulator) semiconductor FETs MOSFET (or MISFET) is currently the most used structure in organic electronic devices. It consists of a gate electrode that is electrically insulated from the conducting channel by an insulator (also called dielectric). The conductive channel is formed by the space between source and drain electrodes. By applying a voltage on the gate electrode, the amount of current that flows between the source and drain can be modulated. In organic semiconductors, FETs have only thus far been operated in accumulation mode and mostly in *p*-mode. The basic structure of a FET device is shown in Figure 1.8.[17]

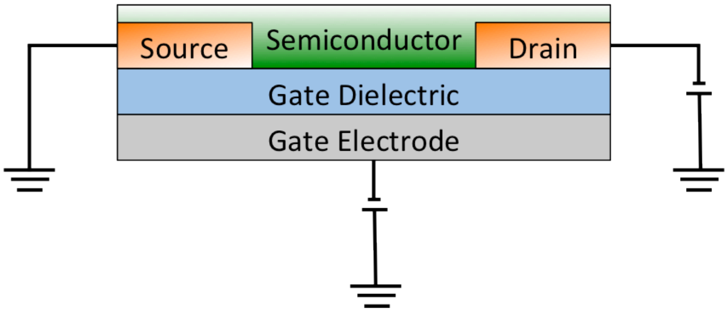

Figure 1.8 The basic device structure of a MOSFET. The channel length is defined by the distance between the source and drain electrodes.

For the basic operation of an organic transistor in the in unipolar/*p*-mode, a negative voltage on the gate electrode is applied, V_g. Under this condition, holes accumulate at the semiconductor-dielectric interface. Alternatively, one could deplete the holes at the interface using a positive gate bias. This accumulation of holes successfully forms a conducting pathway along the entirety of the channel.[46] As means of material characterization, the so-called output (sweep drain voltage, V_d, as a function of fixed gate voltages, V_g) and transfer curves (sweep V_g at fixed V_d) can be collected. With these curves, classic analytical MOSFET equations can be used to determine the carrier mobility in either the linear or saturation regimes. The reader is referred to references [17,47,48] for a complete description of the operation modes and equations that define MOSFET operation.

Recently, research has focused on obtaining higher and higher charge mobilities so that application in advanced technologies such as switching backplanes and electronic paper can be realized. Most of this effort has centered on semiconductor and gate dielectric material design. State-of-the-art OFETs have unipolar mobilities on the order of ~ 40 cm^2/Vs for holes and ~ 10 cm^2/Vs for electrons.[47]

1.4 Electrical Contacts to Organic Semiconductors

Since organic semiconductors cannot be readily doped, forming ohmic contacts is challenging, since it requires that the metal contact's work function matches well with the HOMO (for hole injection) or LUMO (for electron injection).[49] The choice and behavior of organic semiconductor-metal contacts is the subject of intense research, since it largely determines the final device performance and characteristics of the device. Generally, one prefers that a device operate in the bulk limited (also referred to as recombination limited) rather than in a contact limited regime.[50–54] However, one can take advantage of contact effects to fabricate carrier-selective diodes, a concept that will be discussed in Chapter 2.

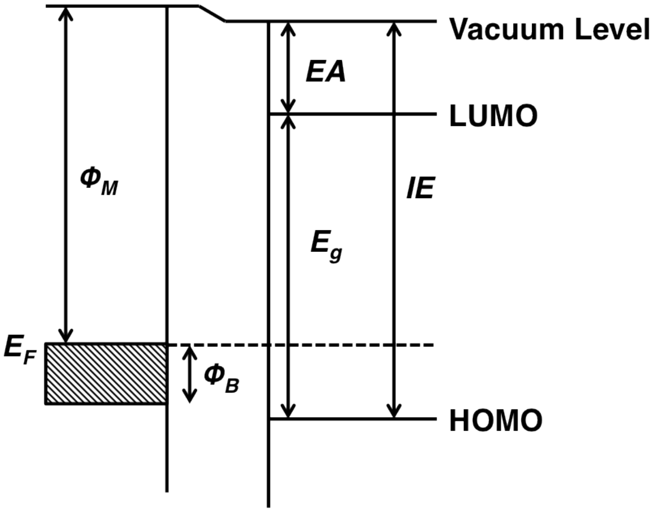

Figure 1.9 Basic important energy levels at the metal-organic semiconductor interface.

Figure 1.9 shows the important energy levels that dictate the behavior of a metal-organic semiconductor interface. In this figure, ϕ_m is the metal work function, E_g is the band gap of the semiconductor *IE* is the ionization energy of the semiconductor, *EA* is the electron affinity of the semiconductor and ϕ_b is the injection barrier.[55] The charge carrier, ϕ_b, is equal to the energetic difference between the metal's Fermi level and the HOMO (hole injection) or LUMO (electron injection). As a rule of thumb, the ϕ_b should be less than 0.3 eV to achieve ohmic contact to the organic semiconductor.[52] Effects such as image forces, interfacial dipoles, bulk and interfacial doping are what govern these energetic barriers at metal-organic interfaces, but these energetics are incredibly difficult to study due to their complex nature. In addition, surface science (i.e. high vacuum studies such as ultra-violet photoelectron spectroscopy) often cannot reflect the true behavior in real device fabrication environments (i.e.

glove boxes).[49] The complexities of injection barriers in organic semiconductors even goes beyond these effects, requiring special models that even must take into account the shape and width of the semiconductor's density of states.[56]

Nonetheless, despite these complexities, methodologies have been used to lower energetic barriers and improve the device performance of all classes of organic semiconductors. One of these approaches requires insertion of inorganic salts such as LiF between the semiconductor and the cathode.[57] However, the true working mechanism of these salts is still unclear. Another methodology necessitates the solution processing a thin layer of ion-bearing polymer between the semiconductor and cathode, such as deoxyribonucleic acid (DNA) or substituted polyfluorenes having quaternized ammonium cations on their side chains.[58–62] It has been hypothesized that these materials induce an interfacial dipole or that their ions lead to enhanced charge injection. Even in this case, this working mechanism is still under debate.[58,63–66]

The final common approach would follow from molecular doping. Doping induces free charge. By taking advantage of image forces, the injection barrier can be significantly lowered.[67] This methodology is a cornerstone of modern vacuum processed OLED architectures, allowing those devices to push theoretical limits on device efficiency. For solution-processed devices, this effect was neatly exploited in *p*-doped polyphenylene vinylenes in reference [68]. One common theme in this thesis lies in modifying these barriers, and is the subject of several chapters where conjugated electrolytes and novel approaches to *p*-doping are shown to reduced interfacial injection barriers.[69]

1.5 Band-Gap Engineering

The simplest of π-conjugated materials and one of the most studied in early work is trans-polyacetylene (**Figure 1.1**) whose synthesis was already described in 1974.[12] Controlling the structure and morphology of polyactylene was always a struggle – although the so-called "Durham" route to synthesizing polyacetylene alleviated some of these problems by affording processability from a soluble precursor.[14] Owing to the poor processability of polyaceteylenes and other early conjugated materials, a quantum leap was made with the development of solution processable polymers, such as the substituted polyphenylene vinylenes like MEH-PPV.[70–74] By attaching alkyl chains along the polymer backbone, solubility in organic solvents can be achieved without significantly disrupting the electronic properties of the polymer.

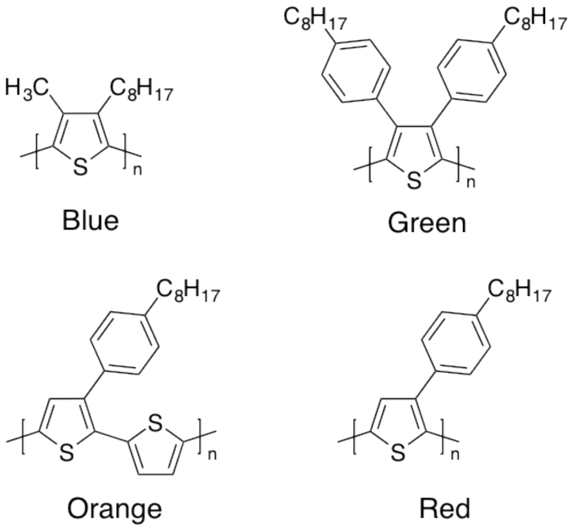

Figure 1.10 Various substituted polythiophenes with different electronic band-gaps.

A greater challenge lies in actually controlling the electronic band-gap of the material (since as discussed before, this determines the function of the material) and for this a variety of approaches exist.[15,16] One example approach lies in the modulation of conjugation length by modifying the degree of coplanarity along the polymer backbone, causing hypsochromic shifts in the luminescence spectrum. Alternatively, introduction of conjugated solubilizing groups cause bathochromic shifts by extending the conjugation. Examples of substituted polythiophenes with various electronic gaps are shown in Figure 1.10.[75]

Another approach to band-gap modulation is the exploitation of qunioidal structures. In brief, this method takes advantage of stabilizing the lower-in-energy quinoid form of an aromatic structure. To exemplify this best, polyisothianaphthene (PITN) and polythiophene are used as examples (Figure 1.11).[76,77] In these structures, resonance with the quinoid form is less stable due to the loss of aromaticity on the thiophene unit. Contrary to this, the quinoidal form of PITN is stabilized by the gain of aromaticity of the fused benzene ring. The stabilization of the quinoidal form results in an effectively lowered band gap relative to the polythiophene.

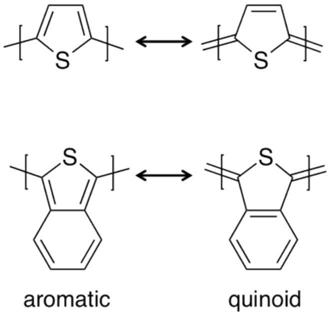

Figure 1.11 The aromatic and quinoidal forms of polythiophene and PITN.

One of the most common approaches to achieve band-gap modulation is the "donor-acceptor" method. Synthesis of alternating electron-donor and electron-acceptor units results in a narrowed band-gap through stabilization of quinoidal structures through intramolecular charge-transfer interactions. Quantum mechanical calculations on donor-acceptor monomers show that hybridization of the HOMO and LUMO levels give rise to small electronic band-gaps (Figure 1.12).[78–82] As shown earlier, increasing the conjugation length would then further reduce the band-gap.

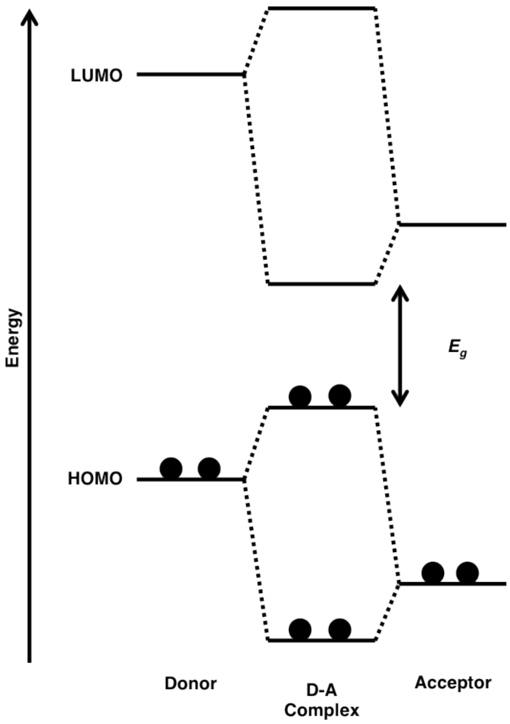

Figure 1.12 Schematic showing the hybridization of the donor and acceptor HOMO/LUMO, resulting in the "D-A complex" with an effectively smaller band-gap. E_g is the resultant energy gap of the D-A system.

This method has been ruthlessly employed in a variety of polymer and oligomer-based organic BHJ solar cells in the search of larger short circuit currents that are a direct result from the reduced band-gaps. For BHJ solar cells, design of new electron rich and electron deficient units dominate research, typically in hopes of obtaining more favorable kinetic or thermodynamically favorable morphologies that result in high efficiencies. A classic example of the D-A methodology was shown in Figure 1.3.2, where the poly[2,6-(4,4-bis-(2-ethylhexyl)-4H-cyclopenta [2,1-b;3,4-`]dithiophene)-alt-4,7(2,1,3-benzothiadiazole)] co-polymer afforded greater performance relative to poly(3-hexylthiophene-2,5-diyl) mostly due to the enhanced short-circuit current afforded by the reduced band-gap.[23] By combining donors and acceptors of various donating and accepting strengths, one can have incredibly control over electronic band gaps.

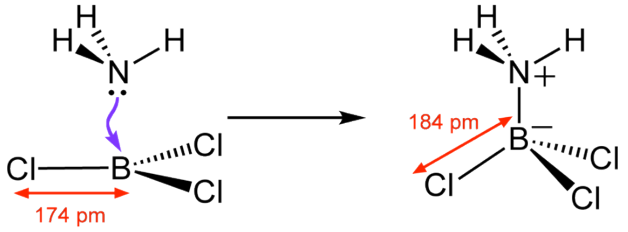

Figure 1.13 Formation of a Lewis acid-base adduct between ammonia and BCl_3. The nitrogen on ammonia has a lone pair of electrons that strongly interact with the vacant p_z orbital on boron.

In the same vein as the donor-acceptor methodology to tune optical gaps, one can also use Lewis acid-base interactions to modulate the electron affinity of various acceptor units. A classic example of a Lewis acid-base interaction is the association of ammonia and a boron trihalide, such as BCl_3 (Figure 1.13).[83,84] To illustrate this effect in a real π-conjugated system, consider a simple D-A copolymer having a repeat unit consisting of electron donor-benzothiadiazole (BT) units (Figure 1.14). Clearly, the sulfur and nitrogen atoms posses lone pairs of electrons that can interact with the vacant p_z orbital of a Lewis acid, much like the ammonia:BCl_3 example.

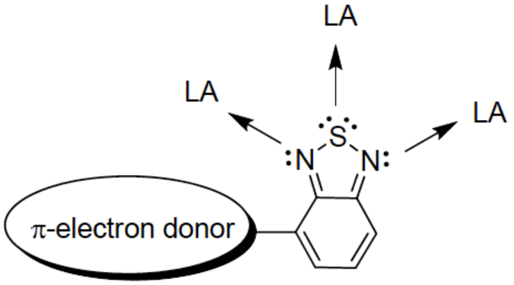

Figure 1.14 Hypothetical donor-acceptor polymer with a benzothiadiazole unit. The arrows represent potential Lewis acid (LA) binding sites.

Through binding of a Lewis acid to one of the Lewis basic atoms, the optical gap of the parent copolymer can be reduced.[85,86] The favorability of adduct formation is a result of a combination of energetics (Lewis basicity of the electron donor/Lewis acidity of the lone pair acceptor) and sterics (size and accessibility of the binding site). The reduced band gap in the model D-A system shown above is the result of a combination of effects: removal of electron density from the BT, increased electron affinity of the BT, and stabilization of the intramolecular charge-transfer excited state. In chapters 7 and 8, this methodology will be used to modulate the optical and electronic properties in two π-conjugated D-A type copolymers.[69,87]

1.6 References

(1) Shirakawa, H.; Louis, E. J.; MacDiarmid, A. G.; Chiang, C. K.; Heeger, A. J. *J. Chem. Soc. Chem. Commun.* **1977**, 578.

(2) Shirakawa, H. *Rev. Mod. Phys.* **2001**, *73*, 713–718.

(3) Bernanose, A.; Vouaux, P. *J. Chim. Phys. Phys.-Chim. Biol.* **1953**, *50*, 261–&.

(4) Bernanose, A.; Comte, M.; Vouaux, P. *J. Chim. Phys. Phys.-Chim. Biol.* **1953**, *50*, 64–68.

(5) Kallmann, H.; Pope, M. *J. Chem. Phys.* **1960**, *32*, 300.

(6) Pope, M.; Kallmann, H. P.; Magnante, P. *J. Chem. Phys.* **1963**, *38*, 2042.

(7) Sano, M.; Pope, M.; Kallmann, H. *J. Chem. Phys.* **1965**, *43*, 2920.

(8) Helfrich, W.; Schneider, W. *Phys. Rev. Lett.* **1965**, *14*, 229–231.

(9) Global Organic Electronics Market - Industry Analysis, Market Size, Share, Growth And Forecast 2012 - 2018 http://www.prweb.com/releases/2013/10/prweb11236639.htm (accessed Mar 20, 2014).

(10) Salzner, U.; Pickup, P. G.; Poirier, R. A.; Lagowski, J. B. *J. Phys. Chem. A* **1998**, *102*, 2572–2578.

(11) Wade, L. G. *Organic chemistry*; 8th ed.; Pearson: Boston, 2013.

(12) Ito, T.; Shirakawa, H.; Ikeda, S. *J. Polym. Sci. Polym. Chem. Ed.* **1974**, *12*, 11–20.

(13) Edwards, J. H.; Feast, W. J. *Polymer* **1980**, *21*, 595–596.

(14) Edwards, J. H.; Feast, W. J.; Bott, D. C. *Polymer* **1984**, *25*, 395–398.

(15) Grimsdale, A. C.; Chan, K. L.; Martin, R. E.; Jokisz, P. G.; Holmes, A. B. *Chem. Rev.* **2009**, *109*, 897–1091.

(16) Cheng, Y.-J.; Yang, S.-H.; Hsu, C.-S. *Chem. Rev.* **2009**, *109*, 5868–5923.

(17) Sze, S. M. *Physics of semiconductor devices*; 3rd ed.; Wiley-Interscience: Hoboken, N.J, 2007.

(18) Mott, N. F. *Can. J. Phys.* **1956**, *34*, 1356–1368.

(19) Conwell, E. M. *Phys. Rev.* **1956**, *103*, 51.

(20) Bässler, H. *Phys. Status Solidi B* **1993**, *175*, 15–56.

(21) Pasveer, W.; Cottaar, J.; Tanase, C.; Coehoorn, R.; Bobbert, P.; Blom, P.; de Leeuw, D.; Michels, M. *Phys. Rev. Lett.* **2005**, *94,* 206601.

(22) Tanase, C.; Meijer, E. J.; Blom, P. W. M.; de Leeuw, D. M. *Phys. Rev. Lett.* **2003**, *91*, 216601.

(23) Peet, J.; Kim, J. Y.; Coates, N. E.; Ma, W. L.; Moses, D.; Heeger, A. J.; Bazan, G. C. *Nat. Mater.* **2007**, *6*, 497–500.

(24) Anthopoulos, T. D.; Setayesh, S.; Smits, E.; Cölle, M.; Cantatore, E.; de Boer, B.; Blom, P. W. M.; de Leeuw, D. M. *Adv. Mater.* **2006**, *18*, 1900–1904.

(25) Bijleveld, J. C.; Zoombelt, A. P.; Mathijssen, S. G. J.; Wienk, M. M.; Turbiez, M.; de Leeuw, D. M.; Janssen, R. A. J. *J. Am. Chem. Soc.* **2009**, *131*, 16616–16617.

(26) Yuen, J. D.; Kumar, R.; Zakhidov, D.; Seifter, J.; Lim, B.; Heeger, A. J.; Wudl, F. *Adv. Mater.* **2011**, *23*, 3780–3785.

(27) Tang, C. W.; VanSlyke, S. A. *Appl. Phys. Lett.* **1987**, *51*, 913–915.

(28) Tang, C. W. Organic electroluminescent cell. US4356429 A, October 26, 1982.

(29) Burroughes, J. H.; Bradley, D. D. C.; Brown, A. R.; Marks, R. N.; MacKay, K.; Friend, R. H.; Burns, P. L.; Holmes, A. B. *Nature* **1990**, *347*, 539–541.

(30) Friend, R. H.; Gymer, R. W.; Holmes, A. B.; Burroughes, J. H.; Marks, R. N.; Taliani, C.; Bradley, D. D. C.; Dos Santos, D. A.; Bredas, J. L.; Lögdlund, M. *Nature* **1999**, *397*, 121–128.

(31) Kuik, M.; Wetzelaer, G.-J. A. H.; Nicolai, H. T.; Craciun, N. I.; De Leeuw, D. M.; Blom, P. W. M. *Adv. Mater.* **2014**, *26*, 512–531.

(32) Ying, L.; Ho, C.-L.; Wu, H.; Cao, Y.; Wong, W.-Y. *Adv. Mater.* **2014**, DOI: 10.1002/adma.201304784.

(33) *Organic light-emitting diodes (OLEDs): materials, devices and applications*; Buckley, A., Ed.; Woodhead Publishing series in electronic and optical materials; Woodhead Publishing: Oxford, 2013.

(34) Knupfer, M. *Appl. Phys. A* **2003**, *77*, 623–626.

(35) Marchetti, A. P.; Tang, C. W.; Young, R. H. Organic photovoltaic elements. US4125414 A, November 14, 1978.

(36) Tang, C. W. *Appl. Phys. Lett.* **1986**, *48*, 183–185.

(37) Yu, G.; Heeger, A. J. *J. Appl. Phys.* **1995**, *78*, 4510–4515.

(38) Yu, G.; Gao, J.; Hummelen, J. C.; Wudl, F.; Heeger, A. J. *Sci.-AAAS-Wkly. Pap. Ed.* **1995**, *270*, 1789–1790.

(39) Halls, J. J. M.; Walsh, C. A.; Greenham, N. C.; Marseglia, E. A.; Friend, R. H.; Moratti, S. C.; Holmes, A. B. *Nature* **1995**, *376*, 498–500.

(40) He, Z.; Zhong, C.; Su, S.; Xu, M.; Wu, H.; Cao, Y. *Nat. Photonics* **2012**, *6*, 593–597.

(41) Thompson, B. C.; Fréchet, J. M. J. *Angew. Chem. Int. Ed.* **2008**, *47*, 58–77.

(42) Sariciftci, N. S.; Smilowitz, L.; Heeger, A. J.; Wudl, F. *Science* **1992**, *258*, 1474–1476.

(43) Hummelen, J. C.; Knight, B. W.; LePeq, F.; Wudl, F.; Yao, J.; Wilkins, C. L. *J. Org. Chem.* **1995**, *60*, 532–538.

(44) Edgar, L. J. Method and apparatus for controlling electric currents. US1745175 A, January 28, 1930.

(45) Dawon, K. Electric field controlled semiconductor device. US3102230 A, August 27, 1963.

(46) Zaumseil, J.; Sirringhaus, H. *Chem. Rev.* **2007**, *107*, 1296–1323.

(47) Sirringhaus, H. *Adv. Mater.* **2014**, *26*, 1319–1335.

(48) Brondijk, J. J. Device physics of organic field-effect transistors, Rijksuniversiteit Groningen, 2012, ISBN: 978-90-367-5667-9.

(49) Shen, Y.; Hosseini, A. R.; Wong, M. H.; Malliaras, G. G. *ChemPhysChem* **2004**, *5*, 16–25.

(50) Blom, P. W. M.; De Jong, M. J. M. *IEEE J. Sel. Top. Quantum Electron.* **1998**, *4*, 105–112.

(51) Van der Holst, J.; Uijttewaal, M.; Ramachandhran, B.; Coehoorn, R.; Bobbert, P.; de Wijs, G.; de Groot, R. *Phys. Rev. B* **2009**, *79*.

(52) Asadi, K.; de Boer, T. G.; Blom, P. W. M.; de Leeuw, D. M. *Adv. Funct. Mater.* **2009**, *19*, 3173–3178.

(53) Campbell, A. J.; Bradley, D. D. C.; Antoniadis, H.; Inbasekaran, M.; Wu, W. W.; Woo, E. P. *Appl. Phys. Lett.* **2000**, *76*, 1734.

(54) Nicolai, H. T.; Wetzelaer, G. A. H.; Kuik, M.; Kronemeijer, A. J.; de Boer, B.; Blom, P. W. M. *Appl. Phys. Lett.* **2010**, *96*, 172107.

(55) Ishii, H.; Sugiyama, K.; Ito, E.; Seki, K. *Adv. Mater.* **1999**, *11*, 605–625.

(56) Novikov, S.; Malliaras, G. *Phys. Rev. B* **2006**, *73*.

(57) Mihailetchi, V. D.; Blom, P. W. M.; Hummelen, J. C.; Rispens, M. T. *J. Appl. Phys.* **2003**, *94*, 6849.

(58) Hoven, C. V.; Yang, R.; Garcia, A.; Crockett, V.; Heeger, A. J.; Bazan, G. C.; Nguyen, T.-Q. *Proc. Natl. Acad. Sci. U. S. A.* **2008**, *105*, 12730–12735.

(59) Hoven, C. V.; Garcia, A.; Bazan, G. C.; Nguyen, T.-Q. *Adv. Mater.* **2008**, *20*, 3793–3810.

(60) Zalar, P.; Kamkar, D.; Naik, R.; Ouchen, F.; Grote, J. G.; Bazan, G. C.; Nguyen, T.-Q. *J. Am. Chem. Soc.* **2011**, *133*, 11010–11013.

(61) Zhang, Y.; Zalar, P.; Kim, C.; Collins, S.; Bazan, G. C.; Nguyen, T.-Q. *Adv. Mater.* **2012**, *24*, 4255–4260.

(62) Zhang, Y.; Wang, M.; Collins, S. D.; Zhou, H.; Phan, H.; Proctor, C.; Mikhailovsky, A.; Wudl, F.; Nguyen, T.-Q. *Angew. Chem. Int. Ed.* **2014**, *53*, 244–249.

(63) Tan, Z.-K.; Vaynzof, Y.; Credgington, D.; Li, C.; Casford, M. T. L.; Sepe, A.; Huettner, S.; Nikolka, M.; Paulus, F.; Yang, L.; Sirringhaus, H.; Greenham, N. C.; Friend, R. H. *Adv. Funct. Mater.* **2014**, *24*, 3051-3058.

(64) Akatsuka, T.; Roldán-Carmona, C.; Ortí, E.; Bolink, H. J. *Adv. Mater.* **2014**, *26*, 770–774.

(65) Tordera, D.; Meier, S.; Lenes, M.; Costa, R. D.; Ortí, E.; Sarfert, W.; Bolink, H. J. *Adv. Mater.* **2012**, *24*, 897–900.

(66) Lenes, M.; Garcia-Belmonte, G.; Tordera, D.; Pertegás, A.; Bisquert, J.; Bolink, H. J. *Adv. Funct. Mater.* **2011**, *21*, 1581–1586.

(67) Pfeiffer, M.; Leo, K.; Zhou, X.; Huang, J. .; Hofmann, M.; Werner, A.; Blochwitz-Nimoth, J. *Org. Electron.* **2003**, *4*, 89–103.

(68) Zhang, Y.; de Boer, B.; Blom, P. W. M. *Adv. Funct. Mater.* **2009**, *19*, 1901–1905.

(69) Zalar, P.; Kuik, M.; Henson, Z. B.; Woellner, C.; Zhang, Y.; Sharenko, A.; Bazan, G. C.; Nguyen, T.-Q. *Adv. Mater.* **2014**, *26*, 724–727.

(70) Srdanov, G.; Wudl, F. Conducting polymer formed of poly(2-methoxy,5-(2'-ethyl-hexyloxy)-p-phenylenevinylene). US5189136 A, February 23, 1993.

(71) Askari, S.; Rughooputh, S.; Wudl, F. *Synth. Met.* **1989**, *29*, E129–E134.

(72) Hoger, S.; Mcnamara, J.; Schricker, S.; Wudl, F. *Chem. Mater.* **1994**, *6*, 171–173.

(73) Sarnecki, G.; Burn, P.; Kraft, A.; Friend, R.; Holmes, A. *Synth. Met.* **1993**, *55*, 914–917.

(74) Braun, D.; Heeger, A. J. *Appl. Phys. Lett.* **1991**, *58*, 1982–1984.

(75) Andersson, M. R.; Thomas, O.; Mammo, W.; Svensson, M.; Theander, M.; Inganas, O. *J. Mater. Chem.* **1999**, *9*, 1933–1940.

(76) Kobayashi, M.; Chen, J.; Chung, T.; Moraes, F.; Heeger, A.; Wudl, F. *Synth. Met.* **1984**, *9*, 77–86.

(77) Bredas, J.; Heeger, A.; Wudl, F. *J. Chem. Phys.* **1986**, *85*, 4673–4678.

(78) Havinga, E.; Tenhoeve, W.; Wynberg, H. *Polym. Bull.* **1992**, *29*, 119–126.

(79) Havinga, E.; Tenhoeve, W.; Wynberg, H. *Synth. Met.* **1993**, *55*, 299–306.

(80) Brocks, G. *J. Phys. Chem.* **1996**, *100*, 17327–17333.

(81) Brocks, G.; Tol, A. *J. Phys. Chem.* **1996**, *100*, 1838–1846.

(82) Brocks, G.; Tol, A. *Synth. Met.* **1996**, *76*, 213–216.

(83) Piers, W. E. In *Advances in Organometallic Chemistry, Vol 52*; West, R.; Hill, A. F., Eds.; Elsevier Academic Press: Amsterdam, The Netherlands, 2005; 1–76.

(84) Miessler, G. L. *Inorganic chemistry*; Fifth edition.; Pearson: Boston, 2014.

(85) Welch, G. C.; Coffin, R.; Peet, J.; Bazan, G. C. *J. Am. Chem. Soc.* **2009**, *131*, 10802–+.

(86) Welch, G. C.; Bazan, G. C. *J. Am. Chem. Soc.* **2011**, *133*, 4632–4644.

(87) Zalar, P.; Henson, Z. B.; Welch, G. C.; Bazan, G. C.; Nguyen, T.-Q. *Angew. Chem. Int. Ed.* **2012**, *51*, 7495–7498.

2.0 Experimental Methods

In this chapter, overviews of all experimental techniques and methods relevant to the work in this thesis will be presented. All active materials in this thesis, such as π-conjugated polymers or small molecules were prepared either by industrial sources or by students in the groups of Professor Guillermo C. Bazan (UCSB) and Professor Fred Wudl (UCSB). The synthesis of these materials are described in the corresponding chapters or adequately referenced therein.

2.1 Device and Film Fabrication

As discussed in Chapter 1, the fabrication of different devices; bulk heterojunction solar cells, light-emitting diodes, field-effect transistors, and single-carrier diodes are possible. The specific details for fabrication of devices made in subsequent chapters will be presented in the experimental section of that chapter. Ideally, all these processes should take place in a clean room environment, should conditions allow. The presence of large amount of large particles may affect the quality and yield of the final device.

To start, however, the majority of organic electronic devices use the same basic procedure for fabrication. At the very beginning, one must first clean the desired substrate. For indium-tin-oxide (ITO) or glass/quartz substrates, the standard cleaning procedure is as follows: (1) The substrates are scrubbed with detergent using gloves for at least 2 minutes on each side. (2) The substrates are thoroughly rinsed with deionized water (though demineralized, 18MΩ water is preferable). (3) The substrates are then sonicated for at least 15 minutes in acetone. (4) The substrates are then sonicated for at least 15 minutes in isopropyl alcohol. (5) The substrates are dried over an N_2 stream. (6) The substrates are dried in a 150 ºC oven for 10 minutes. (7) The substrates are treated to at least 20 minutes of UV-O_3. After these steps, the ITO or glass/quartz substrates are ready for the next fabrication step, which could be either deposition of hole-injection layers, the desired organic semiconductor, or thermal deposition of a bottom electrode.

For SiO_2 substrates, specifically those used for field-effect transistors (meaning it has SiO_2 thermally grown atop n^{++} doped Si), the cleaning procedure is modified. For best results, the substrates are sonicated in Piranha solution (3:1 H_2SO_4:H_2O_2) for 15 minutes. This solution will oxidize most organics but will also effectively hydroxylate (add –OH groups) to the SiO_2 surface, making it more hydrophilic. The substrates are subsequently rinsed thoroughly with deionized water and then sonicated in acetone and isprop ropyl alcohol for 15 minutes each. The substrates are then dried over an N_2 stream and used *as is*. This property will increase the quality and coverage of common surface passivation treatments, such as octyltrichlorosilane (OTS) or hexamethyldisilazane (HMDS).[1] The details of treating substrates with these treatments will be discussed in more detail chapters 4 and 5.

Once the substrate has been cleaned, the next step in the fabrication can proceed. To deposit polymer layers the most commonly used technique is spin coating, although a variety of other methods exist such as dip-coating, drop-casting, ink-jet printing, and spray-coating. None of these other methods are used in this thesis. It should be noted that each of these different coating methods may lead to different optical and electrical properties of the deposited material. In spin coating, a small amount of liquid solution (~ 50 µL) containing the organic semiconductor is deposited on the substrate. The solution is thinned and dried by fast rotation of the substrate (500-5000 rpm). This deposition method leads to consistent and high quality thin-films that are suitable for characterization. The spin-speed and solution concentration can be modified to arrive at different film thicknesses.

After deposition the necessary underlying layers, the final step is typically application of the final contact electrode (though this process could also occur *directly* after substrate cleaning). This is done by thermal deposition. In thermal deposition, a source of metal or inorganic salt is heated in vacuum and the vaporized metal travels to the substrate and condenses. Typical metals and salts used in this thesis include the following: Ag, Al, Au, Ba, Ca, Cs_2CO_3, LiF, and MoO_3. Organic materials can also be deposited using this method, as is the case for currently commercialized organic light-emitting diode devices.

2.2 Experimental Methods

In general, for the use and operation of *standard* and *well-established* characterization techniques and equipment such as: UV-visible spectroscopy, photoluminescence spectroscopy, photoluminescence lifetime, photoluminescence quantum yield, atomic force microscopy (AFM), conducting atomic force microscopy (*c*-AFM), x-ray diffraction, ultraviolet/x-ray photoelectron spectroscopy, and impedance spectroscopy; the reader is directed a wealth of literature and internet resources that explain in detail the mechanism and methodology for each technique. In the following sections, a very brief overview of basic electrical characterization performed in this thesis will be discussed, since this topic is more obscure.

A. Diode Current Measurements

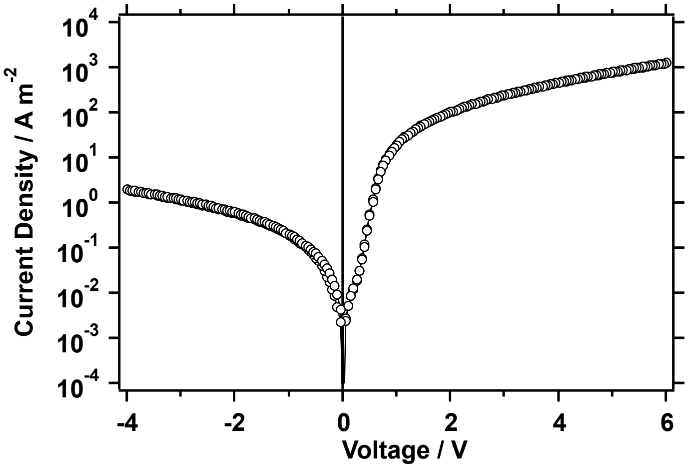

Figure 2.1 Current density-voltage (*J-V*) trace for a typical diode with a π-conjugated polymer or small-molecule as the active layer sandwiched between two electrodes. The built in-voltage appears at roughly 0.35 V.

In this thesis, all diodes were measured in either an inert atmosphere of N_2 or in vacuum at < 1 × 10^{-6} torr. Electrical contact was either made using electrical probes (probe station setup) or sample clip (glove box setup). Current-voltage (*I-V*) measurements were either performed in the dark or under simulated solar illumination using a Keithley 2400 Source Meter Unit or Keithley 4200 Semiconductor Characterization System. For light-emitting diodes, a Si photodiode is placed in front of the devices to measure the light output. Electroluminescence spectra are collected using an Ocean Optics Inc. Spectrophotometer.

Typical current density-voltage (*J*-*V*) characteristics of a single-carrier device, LED, or solar cell dark current is shown in Figure 2.1. In this device, there are three clear distinct regimes: (1) linearly scaling leakage current, symmetric about 0 V, (2) exponential regime until the built-in voltage, and (3) space-charge limited current regime.[2] Deviations from (3) are caused by possible field-dependence in mobilities, recombination in the device, or the series resistance of the contacts.[3,4]

For single-carrier devices, one can use the quadratic voltage behavior to extract the carrier mobility (hole, electron, or effective). Throughout this thesis, regime (3) was fit to the Mott-Gurney Law[5,6]:

$$J = \frac{9}{8}\varepsilon_0 \varepsilon_r \mu \frac{V^2}{L^3}$$

where μ is the zero field mobility, ε_0 is the permittivity of free space, ε_r is the relative dielectric constant of the material, and L is the device thickness. This mobility is more informative than those obtained using transient techniques since it takes into account the thickness scaling in mobility while averaging slow and fast carriers. Transient techniques like time-of-flight tend to give mobilities that heavily depend on device dimensions – giving rise to measurements that are of little information on the material-under-question's true properties. Use of other models, such as field-dependent/Poole-Frenkel/Murgatroyd type equations is incorrect owing to the strong dependence of mobility on carrier density than on field.[4,7] These models have usually been used in the literature to compensate for poor device qualities (high leakage, thin layers, etc.).[8] By further using the temperature dependence of diode characteristics, additional information can be extracted from the system that include the activation energy of hopping.

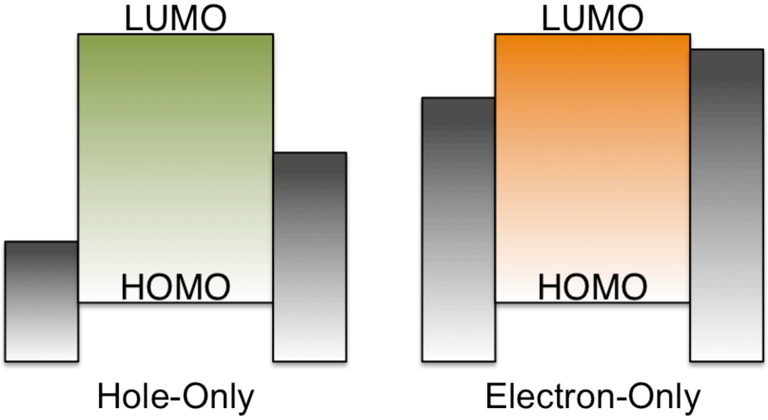

Figure 2.2 Schematic showing the relative energetic levels of electrodes and HOMO/LUMO for hole-only and electron-only devices.

To fabricate a carrier selective device to extract the hole or electron mobility the electrodes need to be carefully selected to either ohmically block or inject electrons or holes. This is schematically shown in Figure 2.2. For these types of devices, one need to be extremely careful about selecting the proper electrodes relative to the HOMO and LUMO levels of the material.

For a hole-only device, the anode *must* make ohmic contact to the HOMO level; this can be achieved using contacts such as PEDOT:PSS or MoO_3.[9,10] At the cathode, a blocking contact is used. For a hole-only device, this could be Au or Ag, depending on the HOMO of the material. For electron-only devices, the anode is usually Al, with Ca forming the necessary ohmic contact to the LUMO at the cathode

B. Field Effect Transistors

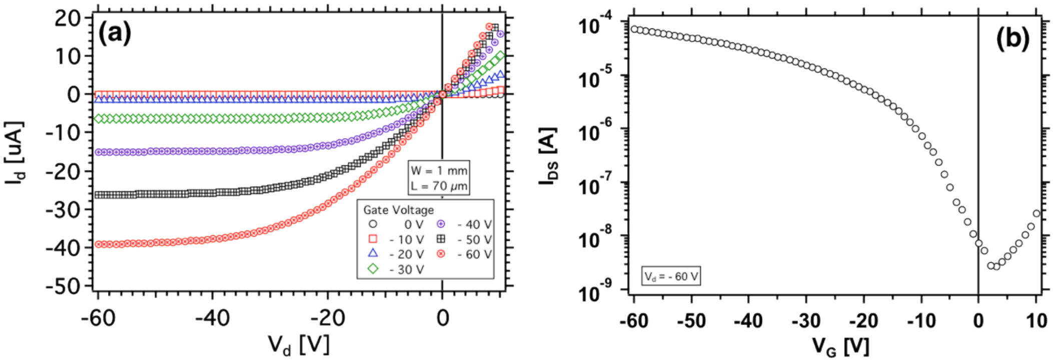

Figure 2.3 Output (a) and (saturation) transfer (b) curves for a typical unipolar (*p*-type) field-effect transistor.

In the same way as the diodes, FETs were measured in a vacuum (1 × 10^{-6} torr) probe station using electrical probes. For these devices, all measurements were performed using a Keithely 4200 Semiconductor Characterization System. As mentioned in the introduction, two different types of measurements can be performed – output (I_d-V_d measurements at fixed V_g) and transfer (I_d-V_g measurements at fixed V_d). In Figure 2.3, typical output (a) and transfer (b) characteristics for a polymer FET are shown.

After verifying the field-effect behavior of the device by sweeping the output curve the transfer characteristics can be used to extract the field-effect mobility. Bear in mind that the field-effect mobility will *always* be greater than the mobility obtained through diode measurements. This is due to the density dependence of mobility – the electric field induced by the gate electrode significantly increases the carrier density in the device.[7] The field-effect mobility can be extracted in one of two regimes: the linear ($V_d \ll V_g - V_t$) or the saturation regime ($V_d \gg V_g - V_t$), where V_t is the threshold voltage. In the saturation regime, the following equation can be used to arrive at the carrier mobility[6,11,12]:

$$\mu_{sat}(V_g) = \frac{2L}{WC_i}\left(\frac{\partial\sqrt{I_d}}{\partial V_g}\right)^2$$

where I_d is the drain-source current in the saturation regime, V_g is the gate voltage, L is the channel length, W is the channel width, and C_i is the capacitance of the dielectric. In the linear regime, this equation is:

$$\mu_{lin}(V_g) = \frac{L}{WC_iV_d}\left(\frac{\partial I_d}{\partial V_g}\right)$$

Using these equations to fit the experimental results, evaluations of carrier mobilities for novel materials designed for high performance transistors or poorly processable materials can be performed. For transistor measurements, the surface energy of the substrate and the concentration of defects will affect the final mobility extracted – marking field-effect mobilities as being "less intrinsic" than those obtained from diode measurements.[1,13]

2.3 References

(1) Don Park, Y.; Lim, J. A.; Lee, H. S.; Cho, K. *Mater. Today* **2007**, *10*, 46–54.

(2) Nicolai, H. T. *Device physics of white polymer light-emitting diodes*; University Library Groningen; Groningen, 2012.

(3) Wetzelaer, G.-J. A. H.; Van der Kaap, N. J.; Koster, L. J. A.; Blom, P. W. M. *Adv. Energy Mater.* **2013**, *3*, 1130–1134.

(4) Blom, P. W. M.; Tanase, C.; Leeuw, D. M. de; Coehoorn, R. *Appl. Phys. Lett.* **2005**, *86*, 092105.

(5) Mott, N. F.; Gurney, R. W. *Electronic processes in ionic crystals*; Dover: New York, NY, 1964.

(6) Sze, S. M. *Physics of semiconductor devices*; 3rd ed.; Wiley-Interscience: Hoboken, N.J, 2007.

(7) Pasveer, W.; Cottaar, J.; Tanase, C.; Coehoorn, R.; Bobbert, P.; Blom, P.; de Leeuw, D.; Michels, M. *Phys. Rev. Lett.* **2005**, *94*, 206601.

(8) Kyaw, A. K. K.; Wang, D. H.; Luo, C.; Cao, Y.; Nguyen, T.-Q.; Bazan, G. C.; Heeger, A. J. *Adv. Energy Mater.* **2014,** *4*, 1301469.

(9) Nicolai, H. T.; Wetzelaer, G. A. H.; Kuik, M.; Kronemeijer, A. J.; de Boer, B.; Blom, P. W. M. *Appl. Phys. Lett.* **2010**, *96*, 172107.

(10) Blom, P. W. M.; de Jong, M. J. M.; Liedenbaum, C. *Polym. Adv. Technol.* **1998**, *9*, 390–401.

(11) Sirringhaus, H. *Adv. Mater.* **2014**, *26*, 1319–1335.

(12) Zaumseil, J.; Sirringhaus, H. *Chem. Rev.* **2007**, *107*, 1296–1323.

(13) Tanase, C.; Meijer, E. J.; Blom, P. W. M.; de Leeuw, D. M. *Phys. Rev. Lett.* **2003**, *91,* 216601.

3.0 Quinacridone Salts as Electron Injection Layers in Polymer Light-Emitting Diodes

In this chapter, a novel water/alcohol soluble quinacridone salt synthesized by Toan Pho (Professor Fred Wudl's group) was utilized as an electron injection layer in a PLED structure utilizing poly[2-methoxy-5-(2'-ethyl-hexyloxy)-1,4-phenylene vinylene] (MEH-PPV) as the emissive layer. By processing a ~20 nm thick layer of quinacridone salt between the MEH-PPV and Al cathode, the luminance efficiency of PLEDs could be increased from 0.85 cd/A to 1.65 cd/A. In addition to devices, the absorption and photoluminescent properties of four different quinacridone salts were characterized. The choice of counterion and alkyl chain has significant effects on the optical and electronic properties of the quinacridone salts.

3.1 Introduction

A Conjugated polyelectrolytes (CPEs) are a unique class of polymer that has found applications in technologies that require solubility in polar media, such as in biosensors[1–5] or chemical sensors.[6] This solubility in polar media is a direct result of the cationic or anionic functional groups that are appended to the repeat units. In organic electronics, this solubility property enables the processing of multilayer structures. This is due to the orthogonal solubility of neutral π-conjugated materials in polar solvents, leading to minimal intermixing of the layers during film deposition.[7,8] In electronic devices, CPEs have been used as the emissive layer in light-emitting electrochemical cells (LECs)[9–13], and as electron-injection (or transport) layers (EILs/ETLs) in PLEDs[8,14–18], organic solar cells[19,20], and for *n*-type FETs.[21] These layers have enabled the use of more stable cathodes like Al to be used, eliminating the need high work function metals, such as Ca or Ba. However, as of late the working mechanism of these materials is under debate.[14,22]

In general, like neutral π-conjugated polymers, CPEs have excellent film forming properties but suffer from classic disadvantages of polymers such as batch-to-batch variations in molecular weight and polydispersity. However, these batch-to-batch variations can be slightly alleviated when synthesis is scaled up. Additionally, the electron mobility and solubility can also be reduced in polymeric materials. Clearly, the use of discrete molecules can overcome these difficulties, thus opening the door to a class of molecules referred to as conjugated oligoelectrolytes.[23] Previous work has shown that these oligoelectrolytes can be used in PLED structures, but their films were non-uniform and extremely rough.[24] Despite this observation, the PLED devices did show enhanced performance.

As an alternative to polyfluorene backbones, we investigate quinacridone-based materials. Quinacridone and its derivatives are a popular pigment in high quality industrial coatings known for their photochemical, chemical, and thermal stability.[25–30] Neutral quinacridones have been used to make self-assembled nanowires and as an electron donor in organic photovoltaics.[31,32]

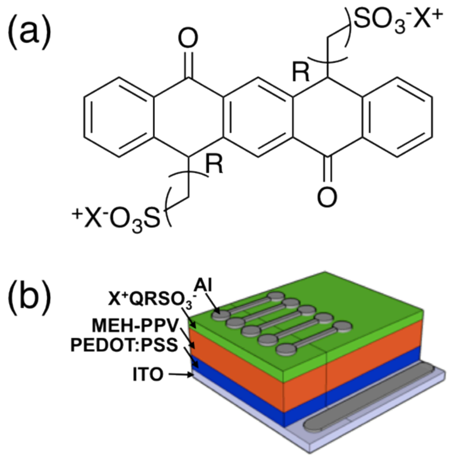

Figure 3.1 Chemical structure of (a) $X^+QRSO_3^-$. R = 3 (P), 6 (H) and X^+ = Na^+, PPh_4^+ and (b) the PLED test structure.

In this chapter, the optical and electronic properties of four quinacridone derivatives is investigated (Figure 3.1): sodium *N,N'*-di(3-sulfonylpropyl)quinacridone ($Na^+QPSO_3^-$), tetraphenylphosphonium *N,N'*-di(3-sulfonylpropyl)quinacridone ($Ph_4P^+QPSO_3^-$), sodium *N,N'*-di(6-sulfonylhexyl)quinacridone ($Na^+QHSO_3^-$), and tetraphenylphosphonium *N,N'*-di(6-sulfonylhexyl)quinacridone ($Ph_4P^+QHSO_3^-$). The synthesis of these materials is reported in reference 33 and is presented herein in the experimental methods. These derivatives can be synthesized on large scales in a single synthetic step from a commercially available precursor. All derivatives were employed as EILs in PLEDs that utilize poly[2-methoxy-5-(2'-ethyl-hexyloxy)-1,4-phenylene vinylene] (MEH-PPV) as the emissive layer.[33] The PLED test structure is shown in Figure 3.1.

3.2 Optical Properties

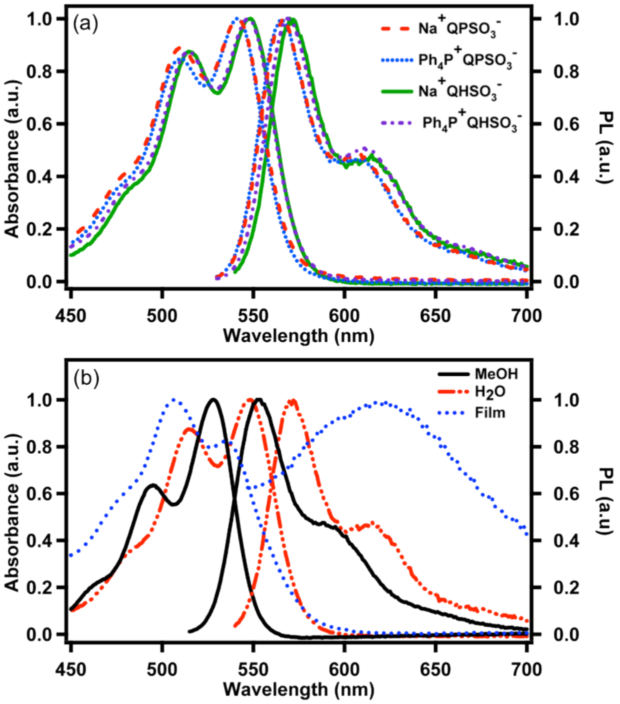

Figure 3.2 (a) The absorption and PL spectra of $X^+QPSO_3^-$ and $X^+QHSO_3^-$ in H_2O. (b) The absorption and PL spectra of $Na^+QHSO_3^-$ in MeOH (black line), water (red dot-dash line), and film (blue dotted line).

In Figure 3.2, the normalized absorption and photoluminescence (PL) spectra of $Na^+QPSO_3^-$, $Na^+QHSO_3^-$, $PPh_4^+QPSO_3^-$, and $PPh_4^+QHSO_3^-$ are shown at concentrations of 1×10^{-3} mg/mL in H_2O. A summary of all observations in this section appears in Table 3.1 at the end of this subsection.

In the absorption spectra of all compounds the 0-0 (~ 545 nm), 0-1 (~ 510 nm), and 0-2 (~ 475 nm) vibronic transitions are clearly resolved. In the PL spectra all compounds have similar maxima and there exists a small shoulder between 600 -

615 nm. Since all derivatives have similar absorption and PL properties in dilute, we find that the choice of counterion has little impact on the intrinsic electronic transitions. This is expected considering that the counterion and alkyl chain *are not* a part of the π- system.

However, differences between different derivatives become obvious when looking at the solution PL quantum yields (Table 3.1.). In general, bulkier counterions seem to give rise to larger quantum yields: 30% versus 21% for the propyl derivatives and 25% versus 18% for the hexyl derivatives. In solution, the bulkier tetraphenyl phosphonium cation may separate the chromophores in solution leading to this observation. This effect has been observed and reported in CPEs.[34]

The absorption spectra of the hexyl derivatives have a ~ 8 nm red-shift relative to the analogous propyl derivative. It is possible that slightly increased aggregation of the hexyl derivatives is the source of this slight red-shift rather than changes in the optical band gap.[34] When comparing the PL quantum yields in H_2O for propyl and hexyl derivatives, there is a general trend that the hexyl derivatives have slightly reduced PL quantum yields (Table 3.1.). In contrast, this observation is reverse when the compounds are dissolved in MeOH.

In Figure 3.2 the absorption and PL spectra for $Na^+QHSO_3^-$ in water, methanol, and in thin-films (processed from 1:1 H_2O:MeOH) is shown. In H_2O, the absorption and PL spectra are red-shifted by 17 nm relative to MeOH – a possible indication of increased aggregation in H_2O. Solution PL quantum yields support this conclusion. By minimizing aggregation, the degree of self-quenching is reduced. This leads to quantum yield reductions from 80% in MeOH to 18% in H_2O. Müllen *et al.* have reported this effect in neutral quinacridones.[35]

The PL spectra of films are broader and red-shifted when compared to the solution spectra. In the film no vibronic structure can be observed, a consequence of chormophoric inhomogeneity. The low PL quantum yield of $Na^+QHSO_3^-$ (1.2%) is a testament to the high degree of self-quenching that takes place in the film. This is the case for all other derivatives studied with quantum yields ranging from 1.6 – 4.1%. As was observed by Yang *et al.*, the counterion did not seem to significantly affect the solid-state quantum yields.[34]

Table 3.1 Summary of optical properties of $X^+QRSO_3^-$ solutions and films. Solutions are all measured at concentrations of 1 × 10^{-3} mg/mL. Films of Na^+ derivatives were deposited from 1:1 H_2O:MeOH mixtures. Films of PPh_4^+ derivatives were deposited from MeOH. See experimental methods for more details.

	H_2O			MeOH			Film		
	λ_{abs} [nm]	λ_{PL} [nm]	ϕ_{PL} [%]	λ_{abs} [nm]	λ_{PL} [nm]	ϕ_{PL} [%]	λ_{abs} [nm]	λ_{PL} [nm]	ϕ_{PL} [%]
$Na^+QPSO_3^-$	541	566	21	528	557	78	535	615	2.7
$PPh_4^+QPSO_3^-$	541	565	30	526	552	74	536	617	1.6
$Na^+QHSO_3^-$	549	570	18	528	554	80	536	617	1.2
$PPh_4^+QHSO_3^-$	547	568	25	527	550	78	534	597	4.1

3.3 Electron Transport

In order to understand, quantify, and evaluate the viability of quinacridone salts as ETLs, electron-only diodes were fabricated in order to determine the electron mobilities, μ_e, of the four quinacridone derivatives. To carry out this measurement, we use a structure of ITO/3-aminopropyltrimethoxysilane (APTMS)/X$^+$QRSO$_3^-$/Ba/Al. In conventional electron-only devices, aluminum forms the bottom anode contact but due to possible problems that may arise from depositing from H_2O:MeOH solution on bare Al, we have used self-assembled-monolayer (SAM) modified ITO. The SAM modified ITO has a work function of 4.3 eV, which is identical to aluminum.[36] Barium forms the ohmic cathode contact to the LUMO of the quinacridone salt.

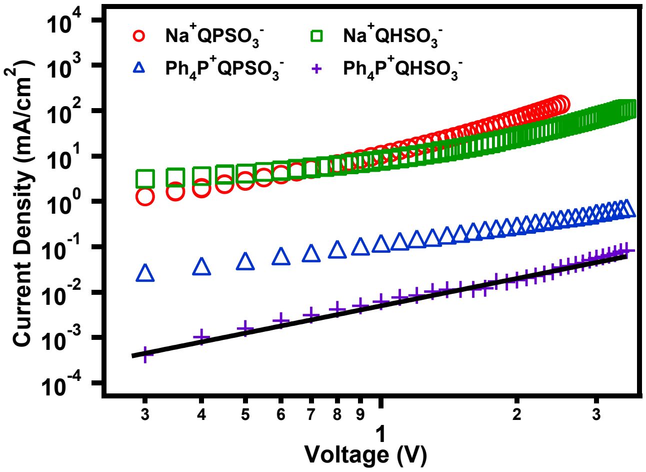

Figure 3.3 ***J-V*** **traces for electron-only devices of ITO/APTMS/X$^+$QRSO$_3^-$/Ba/Al. The solid line is the fit to the Mott-Gurney Law.**

In Figure 3.3, a log-log plot of the forward bias *J-V* characteristics for all quinacridone salts are shown. The solid line represents a fit to the $J \alpha V^2$, the trap-free

Mott-Gurney Law (see Chapter 2).[37–40] In general, the Na^+ derivatives have higher current densities for similar film thicknesses. Using the Mott-Gurney Law, the electron mobilities extracted are 3.9×10^{-5} cm^2/Vs for $Na^+QPSO_3^-$, 3.8×10^{-5} cm^2/Vs for $Na^+QHSO_3^-$, 2.9×10^{-7} cm^2/Vs for $PPh_4^+QPSO_3^-$, and 1.6×10^{-7} cm^2/Vs for $PPh_4^+QHSO_3^-$. These values are summarized in Table 3.2. Modification of the alkyl chain length – propyl versus hexyl, results in essentially no change in electron mobility. However, when going from Na^+ counterions to PPh_4^+ the electron mobility is reduced by two orders of magnitude. While this may be influenced by the counterion, one cannot definitively exclude the effects of processing the films with different solvents. All electron mobilities are within the same range as typical organic semiconductors.

Table 3.2 Electron mobilities, μ_e, obtained from space-charge limited current measurements of electron-only diodes of $X^+QRSO_3^-$.

Material	μ_e [cm^2/Vs]
$Na^+QPSO_3^-$	3.9×10^{-5}
$Na^+QHSO_3^-$	3.8×10^{-5}
$PPh_4^+QPSO_3^-$	2.9×10^{-7}
$PPh_4^+QHSO_3^-$	1.6×10^{-7}

To rationalize the two orders of magnitude difference in electron mobility, we examined the surface topology of $X^+QRSO_3^-$ films. The surface topologies as obtained by atomic force microscopy (AFM) are shown in **Figure 3.4**. Tapping mode images were obtained on the surface between the electrodes of devices used in the electron transport measurements in a dry N_2 glovebox. The surfaces of the Na^+ salts are rough, with root-mean-square (RMS) roughnesses of 7.1 and 21.2 nm for the propyl (Figure 3.4a) and hexyl (Figure 3.4b) compounds respectively. Longer alkyl chains seem to give rise to more 'fiber-like' structures.

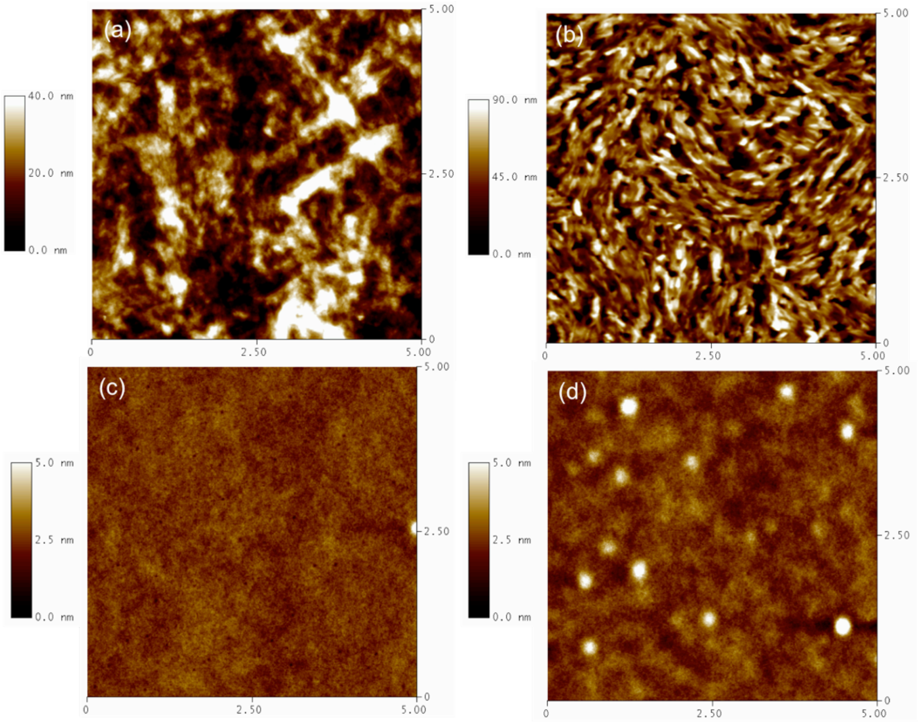

Figure 3.4 Surface topologies of (a) $Na^+QPSO_3^-$, (b) $Na^+QHSO_3^-$, (c) $PPh_4^+QPSO_3^-$, and (d) $PPh_4^+QHSO_3^-$ as measured by AFM in a N_2 glovebox. The image sizes are 5 × 5 µm.

In the PPh_4^+ salts, the film surfaces are *much* smoother, with RMS roughnesses of 0.28 and 0.58 nm for the propyl (Figure 3.4c) and hexyl (Figure 3.4d) derivatives, respectively. The films lack any distinct features, consistent with observations of amorphous π-conjugated materials. This observation may correlate with the electron mobility measurements, in that the bulky nature of the PPh_4^+ counterion may strongly interfere with molecular packing thus significantly impacting the energetic landscape.[41] In the past, large counterions have already been shown to disrupt solid-state organization of π-conjugated materials.[34]

3.4 Polymer Light-Emitting Diodes

Next, with these fundamental properties in hand, the performance of the four quinacridone salts as EILs in PLED test-structures was explored. In Figure 3.5, the *J-V*, luminance-voltage (*L-V*), and luminance efficiency-current density (*LE-J*) curves for ITO/PEDOT:PSS/MEH-PPV/EIL (quinacridone salt)/Al devices and two reference devices for ohmic electron injection (ITO/PEDOT:PSS/MEH-PPV/Ba/Al) and injection limited electron injection (ITO/PEDOT:PSS/MEH-PPV/Al).

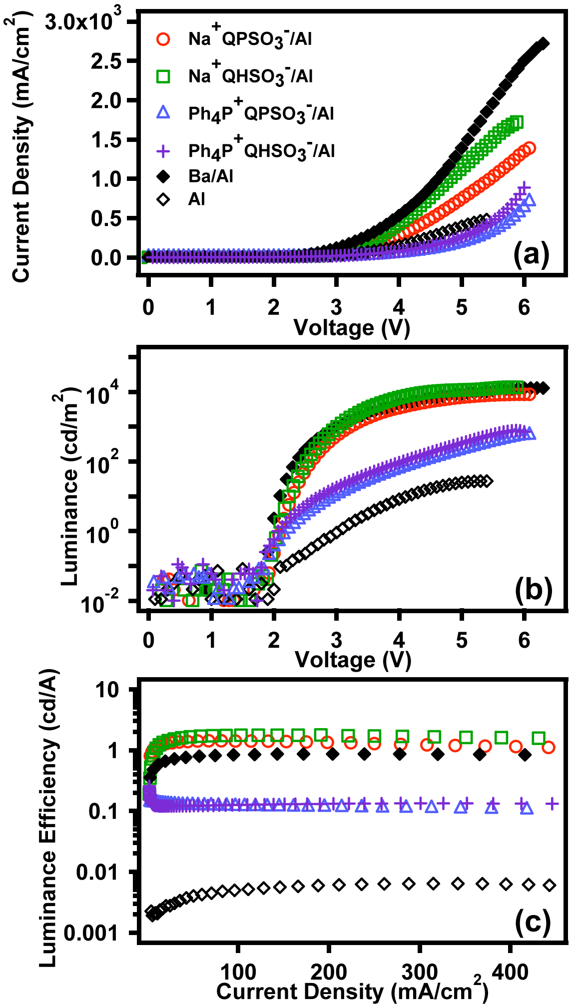

Figure 3.5 (a) Current density-voltage (*J-V*), (b) luminance-voltage (*L-V*), and luminance efficiency-current density (*LE-J*) characteristics of test PLEDs using EILs consisting of: $Na^+QPSO_3^-$ (red circles), $Na^+QHSO_3^-$ (green squares), $PPh_4^+QPSO_3^-$ (blue triangles), and $PPh_4^+QHSO_3^-$ (purple crosses). Reference devices with Ba/Al (filled black diamonds) and Al (open black diamonds) cathodes are also included for comparison.

A summary of all device characteristics appears in Table 3.3. All devices using quinacridone EILs have a turn-on bias for luminance of 1.9 V that is comparable to the Ba device, where electron injection is ohmic. Among all devices using the quinacridone salt, $Na^+QHSO_3^-$ gave the best performance; even out performing the Ba reference device. The Ba device has a maximum luminance of 12800 cd/m^2 but the $Na^+QHSO_3^-$/Al device has a maximum of 13400 cd/m^2 while both turn on at roughly 1.9 V. When going to the Na^+ derivative with a propyl alkyl chain, the turn-on voltage is unchanged but the luminance is reduced by ~ 40% to 8460 cd/m^2. The luminance efficiencies of $Na^+QPSO_3^-$ and $Na^+QHSO_3^-$ were 1.65 and 1.22 cd/A at 300 mA/cm2, much higher than the barium device that was only 0.85 cd/A. The PPh_4^+ derivatives had maximum luminances of only 560 cd/m^2 and efficiencies of 0.11 cd/A, an order of magnitude lower than the Na^+ counterparts.

Table 3.3 Summary of main device parameters extracted for PLED test structures.

Cathode	Turn-On Voltage [V, L = 1 cd/m^2]	Maximum Luminance [cd/m^2]	Luminance Efficiency [cd/A, at 300 mA/cm^2]
Al	3.0	100	6.5×10^{-3}
Ba/Al	1.9	12800	0.85
$Na^+QPSO_3^-$	1.9	8460	1.65
$Na^+QHSO_3^-$	1.9	13400	1.22
$PPh_4^+QPSO_3^-$	1.9	560	0.11
$PPh_4^+QPSO_3^-$	1.9	560	0.11

The difference in performance between the various derivatives seems to correlate well with the trends observed for the electron mobilities.[42–44] As mentioned previously, the Na^+ materials have electron mobilities that are two orders of magnitude larger than the PPh_4^+ materials (10^{-5} v 10^{-7} cm2/Vs). Our observation seems to suggest that electron mobility through the EIL is crucial to obtaining high efficiency multilayer PLEDs. The efficiency of our devices utilizing quinacridone EILs seems to exceed those of CPE based devices. This demonstrates the feasibility of π-conjugated small molecule electrolytes as EILs in multilayer organic electronic devices.

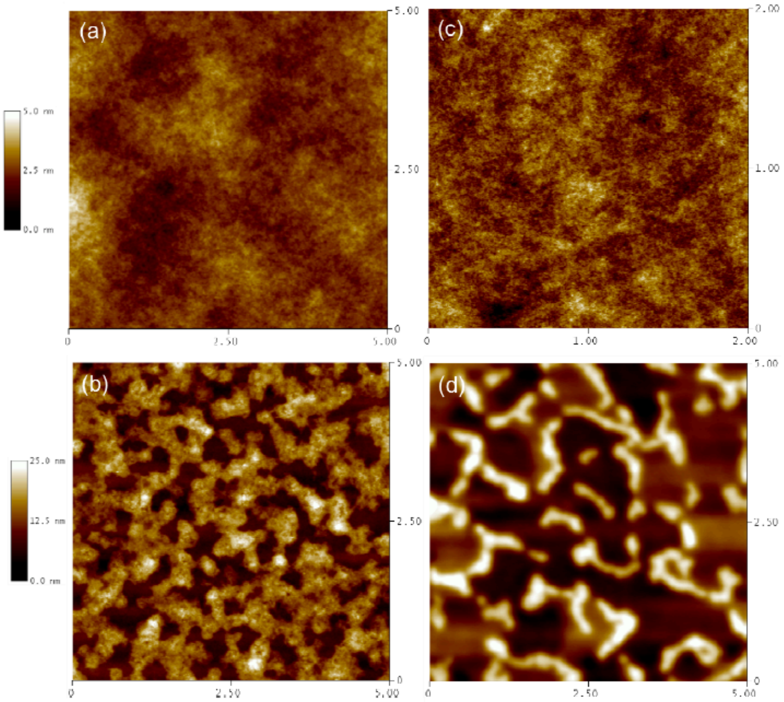

Figure 3.6 The surface topologies of (a) $PPh_4^+QPSO_3^-$, (b) $Na^+QPSO_3^-$, (c) $PPh_4^+QHSO_3^-$, and (d) $Na^+QPSO_3^-$ atop MEH-PPV.

The surface topology of the quinacridone layers atop MEH-PPV was also evaluated. This data is shown in Figure 3.6**.** In general, the PPh_4^+ materials show better film coverage and less structure, just as in the pure films used in the single-carrier diode characterization. Na+ derivatives have more irregular/chaotic surfaces. Nonetheless, as shown in the electron-only diode measurements, it seems that the bulkier PPh_4^+ counterion, while leading to more smooth and amorphous films leads to much poorer intermolecular electronic coupling. Denser and more well packed molecules lead to greater coupling, as has been observed for polymer systems.

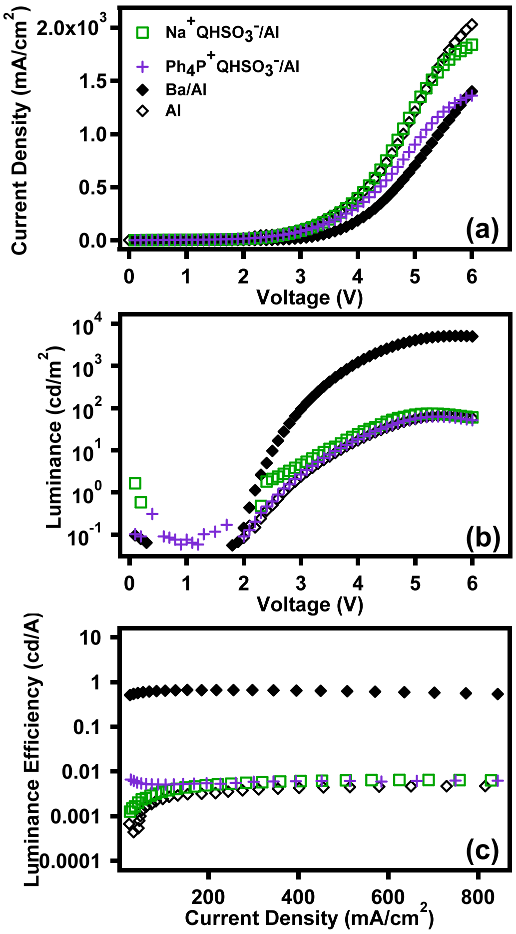

Figure 3.7 (a) *J*-*V*, (b) *L*-*V*, and (c) *LE*-*J* traces utilizing thin EILs processed from Na$^+$QHSO$_3^-$ (green squares) and PPh$_4^+$QHSO$_3^-$ (purple crosses). As before, reference devices with Ba/Al (solid black diamonds) and Al (open black diamonds) cathodes appear for comparison.

It has been demonstrated in the past that devices utilizing thick EILs, i.e. greater than 5 nm, are strongly influenced by the motion of ions through the layer. On the contrary, it has been proposed that devices with thin EILs are influenced more by the presence of an 'interfacial dipole' at the semiconductor-cathode interface.[14] In the case of thin layers, molecular packing and electron transport properties should play in a less significant role when influencing the device performance. Thus, we have processed devices using $Na^+QHSO_3^-$ and $PPh_4^+QHSO_3^-$ as the EIL with thicknesses of ~ 3 nm. The results of this experiment, along with control architectures, are shown in Figure 3.7.

For thin EILs, the turn-on voltage (when L = 1 cd/A) is always 2.7 V. For both materials, the performance is similar to the Al control device, yielding luminance maxima of ~ 60 cd/m^2 at 6.0 V. The luminance efficiency of devices incorporating thin EILs are only marginally higher than the Al reference, with a luminance efficiency of 0.06 cd/A versus 0.04 cd/A. This is surprising since for CPEs, extremely thin layers have been shown to perform *as well* as Ba control devices. This discrepancy is attributed to the lack of continuous film formation. Figure 3.8 shows AFM topology measurements that support this conclusion. It seems that the quinacridone materials dewet atop the hydrophobic MEH-PPV surface.

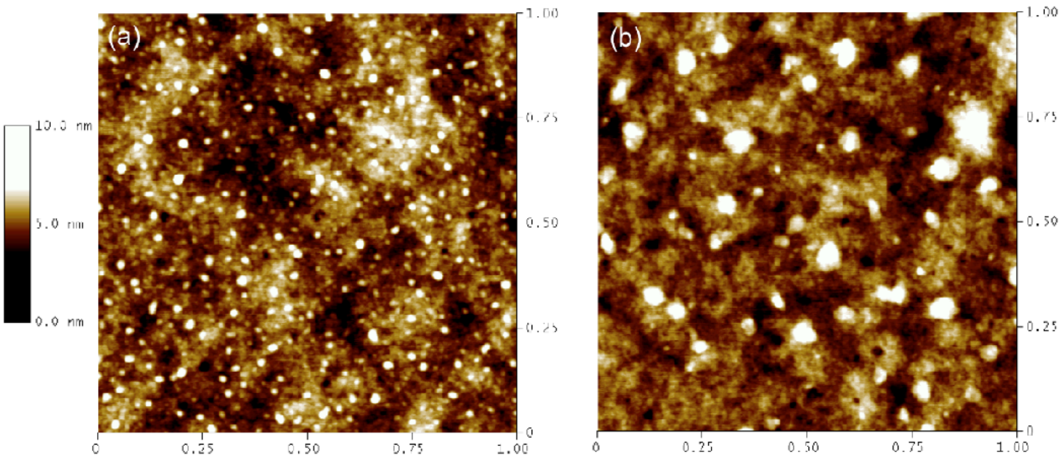

Figure 3.8 Surface topology of thin films of (a) $Na^+QPSO_3^-$ and (b) $PPh_4^+QPSO_3^-$ atop MEH-PPV. Much of the background appears similar to the topology of pristine MEH-PPV layers.

3.5 Conclusions

In summary, the optical and electronic properties of four different quinacridone salts were studied. We found that longer alkyl chains led to more aggregation in solution and greater order in the solid-state. Aggregation behavior in solution strongly correlates with red-shifted absorption spectra and PL quantum yield measurements. In $X^+QRSO_3^-$ molecules, switching solvents from H_2O to MeOH leads to a factor 3 reduction in the quantum yield. In films, this effect is more extreme, with red-shifts being observed of up to 60 nm and a nearly 60-fold reduction in the PL quantum yield.

The bulky nature of the PPh_4^+ counterion interferes with molecular packing, as substantiated by absorption, PL, PL quantum yields, surface morphology, and electron-only diode measurements. The small size of the Na^+ counterion alleviates these problems, enhancing the degree of intermolecular electronic coupling.

All quinacridone derivatives were demonstrated to work as EILs in multilayer PLEDs, displaying turn-on voltages rivaling Ba/Al control devices. Of all the materials, $Na^+QHSO_3^-$ was shown to be the most effective at improving device performance (with luminance efficiencies of 1.65 cd/A), surpassing the performance of the Ba/Al control (luminance efficiency of 0.85 cd/A).

Quinacridone salts are a promising class of small molecule electrolytes that are shown to have utility as EILs. This kind of material should easily find application in device architectures where CPEs have already been so successfully. Their simple and rapid synthesis, along with simple purification makes this an exciting material for future studies – both synthetic and electronic.

3.6 Experimental Methods

General Details: Toluene and anhydrous methanol were purchased from Sigma Aldrich and used as received. All solutions containing water were prepared using 18 MΩ water to ensure that no other ions were present.

Synthesis of Quinacridone Salts: N,*N'*-di(6-bromohexyl)quinacridone was synthesized using a previously reported procedure. A solution of Na_2SO_3 (1.18 g, 9.6 mmol) in H_2O (20 mL) was added to a mixture of *N,N'*-di(6-bromohexyl)quinacridone (1.0 g, 1.6 mmol) in EtOH (20 mL). The mixture was refluxed for two days. Additional Na_2SO_3 (0.59 g, 4.8 mmol) and H_2O (20 mL) were added, and the mixture was refluxed for another two days. Ph_4PCl (2.40 g, 6.4 mmol) and H_2O (50 mL) were added, and the mixture was extracted with DCM (3x). The combined organic extracts were dried over $MgSO_4$ and concentrated in *vacuo*. The residue was recrystallized from hot acetone to give $PPh_4^+QHSO_3^-$ (1.5 g, 1.1 mmol, 73%) as red crystals. ^1H NMR (CD_2Cl_2): δ 8.65 (s, 2H), 8.42 (d, *J* = 7.8 Hz, 2H), 7.89 (t, *J* = 7.4 Hz, 8H), 7.73 (m, 18H), 7.61 (t, *J* = 8.1 Hz, 16H), 7.53 (d, *J* = 8.7 Hz, 2H), 7.19 (t, *J* = 7.4 Hz, 2H), 4.45 (t, *J* = 7.4 Hz, 4H), 2.71 (t, *J* = 7.7 Hz, 4H), 1.96 (br, 4H), 1.81 (p, *J* = 6.7 Hz, 4H), 1.61 (p, *J* = 6.7 Hz, 4H), 1.55 (p, *J* = 6.7 Hz, 4H). ^{13}C NMR (CD_2Cl_2): δ 178.17, 142.86, 136.31, 135.17, 135.03, 131.19, 128.20, 126.84, 121.62, 121.15, 118.48, 117.77, 115.53, 113.82, 52.31, 46.89, 29.35, 27.50, 27.37, 26.07. MS (ESI) *m*/*z*: 319 $(M\text{-}2Ph_4P)^{2-}$, 977 $(M\text{-}Ph_4P)^-$.

A solution of NaI (0.3 g, 2.0 mmol) in acetone (75 mL) was added to a suspension of $Ph_4P^+QHSO_3^-$ (1.05 g, 0.8 mmol) in acetone (300 mL). The mixture was stirred for 45 minutes at room temperature, resulting in a red precipitate that was filtered and washed with acetone. Yield 0.55 g, 99%. ^1H NMR (DMSO-d6): δ 8.65 (s, 2H), 8.38 (d, *J* = 7.8 Hz, 2H), 7.87-7.85 (m, 4H), 7.32 (t, *J* = 7.0 Hz, 2H), 4.54 (t, *J* = 6.8 Hz, 4H), 2.44 (t, *J* = 7.1 Hz, 4H), 1.88 (br, 4H), 1.63 (p, *J* = 7.0 Hz, 4H), 1.56 (p, *J* = 6.2 Hz, 4H), 1.48 (p, *J* = 6.6 Hz, 4H). ^{13}C NMR (DMSO-d6): δ 176.68, 141.95, 135.20, 135.03, 127.04, 125.70, 120.94, 120.32, 115.68, 113.11, 51.43, 45.56, 28.26, 26.56, 26.16, 25.27. MS (ESI) *m*/*z*: 319 $(M\text{-}2Na)^{2-}$, 661 $(M\text{-}Na)^-$.

Optical Characterization: Solid-state absorption, photoluminescence (PL), and quantum yield measurements were performed on quartz substrates that were cleaned by heating in 70:30 (v:v) H_2SO_4:H_2O_2 solution followed by sonication in water twice for 10 min each, in acetone for 30 min, and in isopropanol for an hour. The substrates were dried under nitrogen gas and subsequently in an oven at 120 °C overnight. Substrates were treated in UV/O_3 (UVO Cleaner 42, Jelight Co. Inc.) for an hour prior to film deposition. Films were deposited from 2% w/v solutions of $Na^+QPSO_3^-$ and $Na^+QHSO_3^-$ in 1:1 H_2O:MeOH and 3% w/v solutions of $PPh_4^+QPSO_3^-$ and $PPh_4^+QHSO_3^-$ in methanol. These solutions were stirred overnight at 40 °C. Solutions used for optical studies were serially diluted to 0.001% w/v concentrations for solution-state absorption, photoluminescence, and quantum yield measurements.

All absorption data was obtained using a Shimadzu UV2401-PC spectrophotometer. Fluorescence spectra were measured on a Photon Technology International Quantum Master fluorometer. Solution state quantum yield measurements were performed using the optically dilute method with fluoroscein in water as a reference. Solid state quantum yield measurements were performed using an integrating sphere and a Ti:Al_2O_3 laser (λ_{ex} = 488 nm).

Atomic Force Microscopy: Surface morphology images of EIL films were performed using a MultiMode atomic force microscope (AFM) with Nanoscope Controller IIIa (Veeco Inc.). All AFM measurements were performed in an inert atmosphere of nitrogen to prevent surface alteration by moisture in air. Silicon probes with a spring constant of ~5 N/m and resonant frequencies of 75 kHz (Budget Sensors) were used for tapping mode measurements. Film thicknesses were determined by AFM.

Device Fabrication: Corning 1737 glass substrates patterned with 140 nm of indium-tin-oxide (ITO) were cleaned using the same procedure as for glass substrates discussed above. A 70 nm thick layer of poly(3,4-ethylenedioxythiophene):polystyrene sulfonic acid, PEDOT:PSS, (Baytron P 4083, H.C. Starck Inc.) is then spin coated on top of the ITO/glass substrate in air and annealed at 140 °C for 45 min. For the emissive layer, a 55 nm thick film of MEH-PPV (Canton OLED King Optoelectric Materials Co., Ltd.) was spin coated at 1500 rpm for 60 seconds from a 0.5% w/v solution in toluene atop of the PEDOT:PSS layer in a nitrogen atmosphere and left to dry for 20 min before deposition of the next layer. $X^+QRSO_3^-$ solutions were spin coated atop of the MEH-PPV film at 1500 rpm for 60 sec in a nitrogen atmosphere. $Na^+QPSO_3^-$ and $Na^+QHSO_3^-$ films were spin coated from a 0.05% w/v solution in 50:50 and 30:70 H_2O:MeOH yielding ~20 nm and ~15 nm thick films, respectively. $PPh_4^+QPSO_3^-$ and $PPh_4^+QHSO_3^-$ films were spin coated from a 0.5% w/v solution in 100% methanol giving ~18 nm and ~20 nm thick films, respectively. After leaving the devices to dry in a 10^{-4} torr vacuum overnight, the 100 nm thick aluminum cathode was deposited by thermal evaporation at a base pressure of 10^{-6} torr. Reference devices were made by thermal evaporation of 5 nm of barium capped with 100 nm of aluminum or with 100 nm of aluminum only. All OLED devices were tested in a nitrogen atmosphere using a Keithley 2602 and multimeter coupled with a photodiode.

Electron-only diodes were prepared by using an aminopropyltrimethoxysilane self-assembled monolayer (SAM) modified-ITO surface. SAM-ITO substrates were prepared using a procedure previously reported by Sfez *et al.* This procedure reduces the work function of ITO from 4.7 eV to 4.3 eV. Films were spin coated in a nitrogen atmosphere from 2% w/v 1:1 H_2O:MeOH for $Na^+QPSO_3^-$ and $Na^+QHSO_3^-$ and from 3% w/v in methanol for $PPh_4^+QPSO_3^-$ and $PPh_4^+QHSO_3^-$ giving film thicknesses of ~100 nm, ~85 nm, ~120 nm, and ~100 nm, respectively. The films were dried in a 10^{-4} torr vacuum overnight. Subsequently, a 5 nm layer of barium was thermally evaporated and capped with 100 nm of aluminum. Current density-voltage (*J-V*) curves for electron only devices were obtained in a nitrogen atmosphere using a Keithley 4200 Semiconductor Characterization System.

3.7 References

(1) Chen, L. H.; McBranch, D. W.; Wang, H. L.; Helgeson, R.; Wudl, F.; Whitten, D. G. *Proc. Natl. Acad. Sci. U. S. A.* **1999**, *96*, 12287–12292.

(2) Wang, D. L.; Gong, X.; Heeger, P. S.; Rininsland, F.; Bazan, G. C.; Heeger, A. J. *Proc. Natl. Acad. Sci. U. S. A.* **2002**, *99*, 49–53.

(3) Duan, X.; Liu, L.; Feng, F.; Wang, S. *Acc. Chem. Res.* **2010**, *43*, 260–270.

(4) Jin, Y.; Yang, R.; Suh, H.; Woo, H. Y. *Macromol. Rapid Commun.* **2008**, *29*, 1398–1402.

(5) Liu, B.; Bazan, G. C. *Chem. Mater.* **2004**, *16*, 4467–4476.

(6) Jiang, H.; Taranekar, P.; Reynolds, J. R.; Schanze, K. S. *Angew. Chem.-Int. Ed.* **2009**, *48*, 4300–4316.

(7) Steuerman, D. W.; Garcia, A.; Dante, M.; Yang, R.; Lofvander, J. P.; Nguyen, T.-Q. *Adv. Mater.* **2008**, *20*, 528–+.

(8) Ma, W. L.; Iyer, P. K.; Gong, X.; Liu, B.; Moses, D.; Bazan, G. C.; Heeger, A. J. *Adv. Mater.* **2005**, *17*, 274–277.

(9) Edman, L.; Pauchard, M.; Liu, B.; Bazan, G.; Moses, D.; Heeger, A. J. *Appl. Phys. Lett.* **2003**, *82*, 3961–3963.

(10) Edman, L.; Liu, B.; Vehse, M.; Swensen, J.; Bazan, G. C.; Heeger, A. J. *J. Appl. Phys.* **2005**, *98*, 044502.

(11) Gu, Z.; Shen, Q. D.; Zhang, J.; Yang, C. Z.; Bao, Y. J. *J. Appl. Polym. Sci.* **2006**, *100*, 2930–2936.

(12) Bolink, H. J.; Coronado, E.; Costa, R. D.; Ortí, E.; Sessolo, M.; Graber, S.; Doyle, K.; Neuburger, M.; Housecroft, C. E.; Constable, E. C. *Adv. Mater.* **2008**, *20*, 3910–3913.

(13) Tordera, D.; Meier, S.; Lenes, M.; Costa, R. D.; Ortí, E.; Sarfert, W.; Bolink, H. J. *Adv. Mater.* **2012**, *24*, 897–900.

(14) Hoven, C. V.; Yang, R.; Garcia, A.; Crockett, V.; Heeger, A. J.; Bazan, G. C.; Nguyen, T.-Q. *Proc. Natl. Acad. Sci. U. S. A.* **2008**, *105*, 12730–12735.

(15) Huang, F.; Wu, H. B.; Wang, D.; Yang, W.; Cao, Y. *Chem. Mater.* **2004**, *16*, 708–716.

(16) Hoven, C. V.; Garcia, A.; Bazan, G. C.; Nguyen, T.-Q. *Adv. Mater.* **2008**, *20*, 3793–3810.

(17) Walker, B.; Tamayo, A.; Yang, J.; Brzezinski, J. Z.; Nguyen, T.-Q. *Appl. Phys. Lett.* **2008**, *93*, 063302.

(18) Garcia, A.; Brzezinski, J. Z.; Nguyen, T.-Q. *J. Phys. Chem. C* **2009**, *113*, 2950–2954.

(19) Yang, J.; Garcia, A.; Nguyen, T.-Q. *Appl. Phys. Lett.* **2007**, *90*, 103514.

(20) Mwaura, J. K.; Pinto, M. R.; Witker, D.; Ananthakrishnan, N.; Schanze, K. S.; Reynolds, J. R. *Langmuir* **2005**, *21*, 10119–10126.

(21) Seo, J. H.; Gutacker, A.; Walker, B.; Cho, S.; Garcia, A.; Yang, R.; Nguyen, T.-Q.; Heeger, A. J.; Bazan, G. C. *J. Am. Chem. Soc.* **2009**, *131*, 18220–18221.

(22) Tan, Z.-K.; Vaynzof, Y.; Credgington, D.; Li, C.; Casford, M. T. L.; Sepe, A.; Huettner, S.; Nikolka, M.; Paulus, F.; Yang, L.; Sirringhaus, H.; Greenham, N. C.; Friend, R. H. *Adv. Funct. Mater.* **2014**, *24*, 3051-3058..

(23) Chen, Z.; Dang, X.-D.; Gutacker, A.; Garcia, A.; Li, H.; Xu, Y.; Ying, L.; Nguyen, T.-Q.; Bazan, G. C. *J. Am. Chem. Soc.* **2010**, *132*, 12160–12162.

(24) Liu, G.; Li, A.-Y.; An, D.; Wu, H.-B.; Zhu, X.-H.; Li, Y.; Miao, X.-R.; Deng, W.-L.; Yang, W.; Cao, Y.; Roncali, J. *Macromol. Rapid Commun.* **2009**, *30*, 1484–1491.

(25) Binant, C.; Guineau, B.; Lautie, A. *J. Soc. Dye. Colour.* **1990**, *106*, 187–191.

(26) Suzuki, E. M.; Marshall, W. P. *J. Forensic Sci.* **1998**, *43*, 514–542.

(27) Stachura, S.; Desiderio, V. J.; Allison, J. *J. Forensic Sci.* **2007**, *52*, 595–603.

(28) Paulus, E. F.; Leusen, F. J. J.; Schmidt, M. U. *Crystengcomm* **2007**, *9*, 131–143.

(29) Berg, D.; Nielinger, C.; Mader, W.; Sokolowski, M. *Synth. Met.* **2009**, *159*, 2599–2602.

(30) Jones, F.; Okui, N.; Patterson, D. *J. Soc. Dye. Colour.* **1975**, *91*, 361–365.

(31) Trixler, F.; Market, T.; Lackinger, M.; Jamitzky, F.; Heckl, W. M. *Chem.-Eur. J.* **2007**, *13*, 7785–7790.

(32) Manabe, K.; Kusabayashi, S.; Yokoyama, M. *Chem. Lett.* **1987**, 609–612.

(33) Pho, T. V.; Zalar, P.; Garcia, A.; Nguyen, T.-Q.; Wudl, F. *Chem. Commun.* **2010**, *46*, 8210–8212.

(34) Yang, R.; Garcia, A.; Korystov, D.; Mikhailovsky, A.; Bazan, G. C.; Nguyen, T.-Q. *J. Am. Chem. Soc.* **2006**, *128*, 16532–16539.

(35) De Feyter, S.; Gesquiere, A.; De Schryver, F. C.; Keller, U.; Mullen, K. *Chem. Mater.* **2002**, *14*, 989–997.

(36) Dang, X.-D.; Tamayo, A. B.; Seo, J.; Hoven, C. V.; Walker, B.; Nguyen, T.-Q. *Adv. Funct. Mater.* **2010**, *20*, 3314–3321.

(37) Lampert, M. A. *Phys. Rev.* **1956**, *103*, 1648–1656.

(38) Hwang, W.; Kao, K. C. *Solid-State Electron.* **1976**, *19*, 1045–1047.

(39) Blom, P. W. M.; De Jong, M. J. M.; Vleggaar, J. J. M. *Appl. Phys. Lett.* **1996**, *68*, 3308–3310.

(40) Blom, P. W. M.; De Jong, M. J. M.; Van Munster, M. G. *Phys. Rev. B* **1997**, *55*, R656.

(41) Yang, R.; Xu, Y.; Dang, X.-D.; Nguyen, T.-Q.; Cao, Y.; Bazan, G. C. *J. Am. Chem. Soc.* **2008**, *130*, 3282–+.

(42) Blom, P. W. M.; de Jong, M. J. M.; Liedenbaum, C. *Polym. Adv. Technol.* **1998**, *9*, 390–401.

(43) Malliaras, G. G.; Scott, J. C. *J. Appl. Phys.* **1998**, *83*, 5399–5403.

(44) Blom, P. W. M.; Vissenberg, M.; Huiberts, J. N.; Martens, H. C. F.; Schoo, H. F. M. *Appl. Phys. Lett.* **2000**, *77*, 2057–2059.

4.0 DNA as an Electron Injection Layer in Polymer Light-Emitting Diodes

In this chapter, a DNA interlayer is placed between the emissive layer, poly[2-methoxy-5-(2'-ethyl-hexyloxy)-1,4-phenylene vinylene] (MEH-PPV), and aluminum cathode in a PLED. Introduction of the DNA interlayer reduces turn-on voltages and higher luminance efficiencies that are comparable to the device incorporating a low work function Ba electrode. This DNA interlayer serves a dual purpose of being an electron injection and hole-blocking layer. The time response of the devices suggest that the DNA layer forms an interfacial dipole adjacent to the electrode, thus causing a significant reduction in the electron injection barrier.

4.1 Introduction

The energetics at organic semiconductor-metal interfaces is very sensitive to the local chemical and energetic environment at the contact.[1–4] These interfaces have a profound effect on the performance and operation of organic semiconducting devices. For PLEDs or organic solar cells, such interfacial behavior dictates the energetics of charge injection and charge extraction. Energetic barriers result in unbalanced hole and electron densities, resulting in lower device performance.[5,6] As discussed in Chapter 1, electron injection barriers are the direct result of a mismatch between the energy of the lowest unoccupied molecular orbital (LUMO) and the metal work function. Stable metals such as aluminum, gold, or silver make poor contact with

LUMO levels of typical electroluminescent polymers. For device evaluation, low work function metals such as Ca or Ba can circumvent contact issues for electron injection, but this strategy is not viable for industrial application since the resultant devices are unstable in air.[7,8]

In vacuum processed OLEDs, the use of doped layers already results in lower operation voltages and enhanced device efficiencies without needing to use low work function metals.[9] In PLEDs and other solution processed devices, the availability and ability to processed doped layers and multilayer structures are more limited.[10–16] Thus far, many different strategies have already been employed for reducing barriers at the semiconductor-cathode interface. One approach involves the use of conjugated polyelectrolytes (CPEs)[17–19] or oligoelectrolytes (OEs, Chapter 3)[20–22]. In short, CPEs or OEs have a conventional π-conjugated backbone, but bear ionic functionalities on the solubilizing chains – giving these materials solubility in polar solvents. The two main mechanisms that govern the reduced injection barriers for devices containing CPEs or OEs are hypothesized to be (1) ion migration or (2) interfacial dipole. In ion migration, application of an external bias results in a redistribution of ions that redistributes the electrical field within the device.[11,12,23] This mechanism mainly occurs in devices having thick layers of CPEs or OEs and leads to long response times for maximal current and luminance, much like one would observe in light-emitting electrochemical cells. The interfacial dipole mechanism mainly occurs in devices incorporating thin layers of CPEs or OEs.[3,24–27] The dipole modifies the *effective* work function of the cathode, leading to fast turn-on times. However, these improvements observed may also be due to a solvent effect that is a direct consequence of using methanol.[28]

It was hypothesized that an interfacial dipole at the polymer-metal interface could be obtained by using a thin layer of a standard polyelectrolyte (i.e. one not containing a π-conjugated backbone).[29–31] One abundant and naturally occurring polyelectrolyte is deoxyribonucleic acid (DNA). DNA has already been shown utility in organic electronic devices, primarily as a gate dielectric in field-effect transistors and as a ~20 nm thick hole-transporting/electron-blocking layer in OLEDs.[32–37]

The United States Air Force Research Laboratory at Wright-Patterson Air Force Base provided the DNA sample used in this study.[32] The sample was originally prepared by the Chitose Institute of Science and Technology using the waste products of the Japanese salmon fishing industry using a process described and is commercially available, see reference [38]. The molecular weight of the DNA is typically > 8000 kDa, as determined by gel phase electrophoresis.[32]

In Figure 4.1, the chemical structure of MEH-PPV and the PLED test structure are shown. MEH-PPV was used in these test structures since efficient hole-injection is readily achieved using common hole-injection layers like poly(3,4-ethylenedioxythiophene):poly(styrenesulfonate) (PEDOT:PSS).[12] This allows for the device characteristics to primarily depend on the behavior of the cathode.

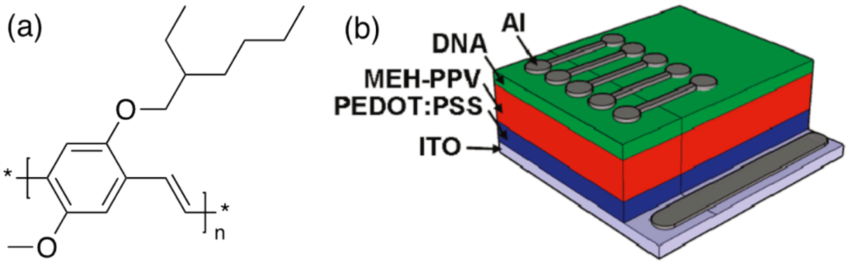

Figure 4.1 (a) The chemical structure of MEH-PPV and (b) the PLED test structure used that incorporates the DNA electron-injection layer.

4.2 Polymer Light-Emitting Diodes

For PLED devices, (Figure 4.1) the DNA interlayer was processed from polar solvents in order to minimize any disturbance of the underlying MEH-PPV layer.[39,40]

Our first attention focused on arriving at optimal processing of the DNA layer. Pure MeOH cannot dissolve the sample so solvent mixtures were used. In order to screen processing conditions for the DNA layer, the DNA was dissolved in 90:10 mixtures of methanol (MeOH):H_2O, acetone $(CH_3)_2CO$:H_2O, acetonitrile (CH_3CN):H_2O, and methyl ethyl ketone (MEK):H_2O at a concentration of 1 mg/mL. The DNA was then processed at 1500 rpm for 60 seconds using a 0.45 μm poly(vinylidene fluoride) (PVDF) filter atop the MEH-PPV layer. Figure 4.2 shows the current density-voltage (*J-V*), luminance-voltage (*L-V*), and luminance efficiency-current density (*LE-J*) characteristics for test PLEDs using DNA interlayers with different solvent mixtures. All these processing conditions give rise to very similar PLED performance, but in general it was found that processing from 90:10 MeOH:H_2O gave the best performance across all current density ranges. The surface topologies of DNA films processed from all these different solvent mixtures vastly different surfaces, which is discussed in the next section.

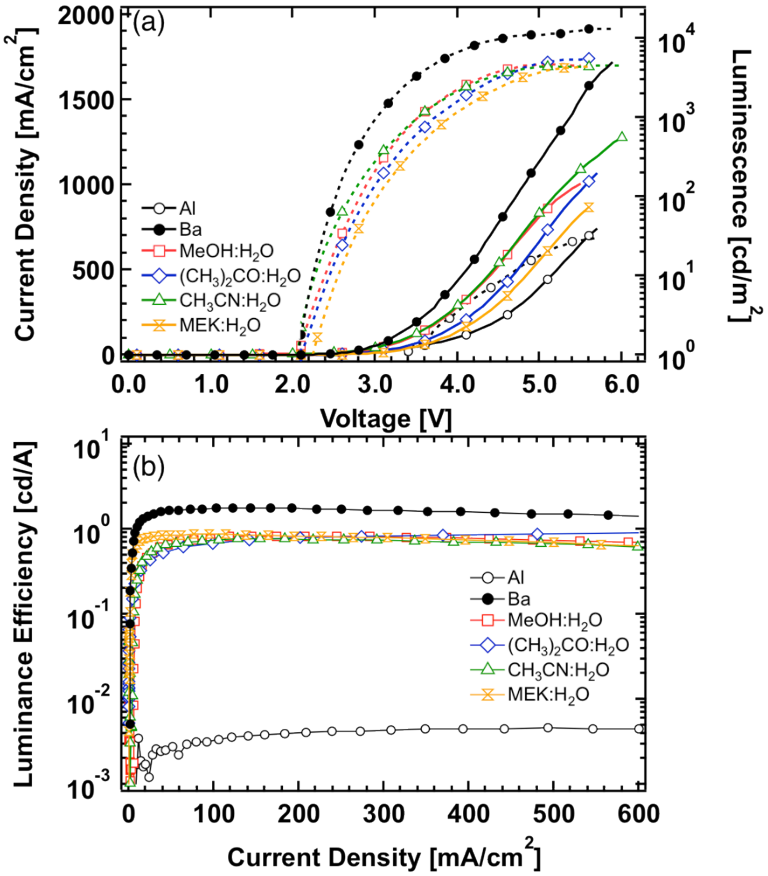

Figure 4.2 (a) *J-V* (solid lines and symbols), *L-V* (dotted lines and symbols) and (b) *LE-J* (solid lines and symbols) characteristics of PLED test structures incorporating DNA processed from different 90:10 mixtures of: MeOH:H_2O (red squares), $(CH_3)_2CO$:H_2O (blue diamonds), CH_3CN:H_2O (green triangles), MEK:H_2O (orange bowties) at a concentration of 0.1% w/v (1 mg/mL). Test structures incorporating Ba (filled black circles) and Al (open black circles) cathodes are included for comparison.

In general, all DNA processing conditions yielded PLEDs that turn on (*L* = 1 cd/m^2) at ~ 2.0 V, except the Al control device that turns on at ~ 3.4 V. The Ba device was the brightest, reaching a maximum luminance of 13400 cd/m^2. All DNA processing conditions had maximum luminance of ~ 4500 cd/m^2. The most evident differences were in the current densities of the devices. The Ba device reaches the highest densities (~ 1700 mA/cm^2), whereas the DNA devices are all somewhat reduced – all in the range of 900 – 1200 mA/cm^2. Of course, these currents are enhanced relative to the Al control, which only reaches a density of ~ 700 mA/cm^2. However, despite these small differences in luminance and current densities, the luminance efficiencies of all the DNA conditions are very similar; all are at about 0.80 cd/A. For comparison, the Ba device has an efficiency of ~ 1.65 cd/A and the Al device is 4 x 10^{-3} cd/A. In subsequent experiments, attention was focused on the MeOH:H_2O mixtures, as they seemed to give the best wetting on MEH-PPV and the most consistent performance.

Using the optimum DNA processing condition (90:10 MeOH:H_2O), further investigation was performed. Figure 4.3 shows the performance of control devices and those incorporating DNA prepared in parallel (i.e. same day, same solutions, etc.). The turn-on voltages for devices with Ba/Al, DNA/Al, and Al cathodes were 1.9 V, 2.3 V, and 3.6 V respectively. The DNA/Al device exhibits *J* and *L* characteristics that are very similar to the Ba device, suggesting a near-ohmic contact for electron injection. For comparison, the *L* at 4.5 V was ~ 8000 cd/m^2 for the Ba device, ~ 5700 cd/m^2 for the DNA/Al device, and ~ 25.5 cd/m^2 for the Al device. Following from the *J* and *L* characteristics, the luminance efficiencies could be readily extracted – yielding efficiencies of 0.80 cd/A for the Ba device, 0.86 cd/A for the DNA/Al device, and 6×10^{-3} cd/A for the Al device. Within the variation in devices, the Ba and DNA/Al device have nearly identical luminance efficiencies (both varying in ± 0.15 cd/A). All these observations conclusively show that the DNA interlayer is effective at improving electron injection in PLED devices, leading to higher efficiencies.[16,41]

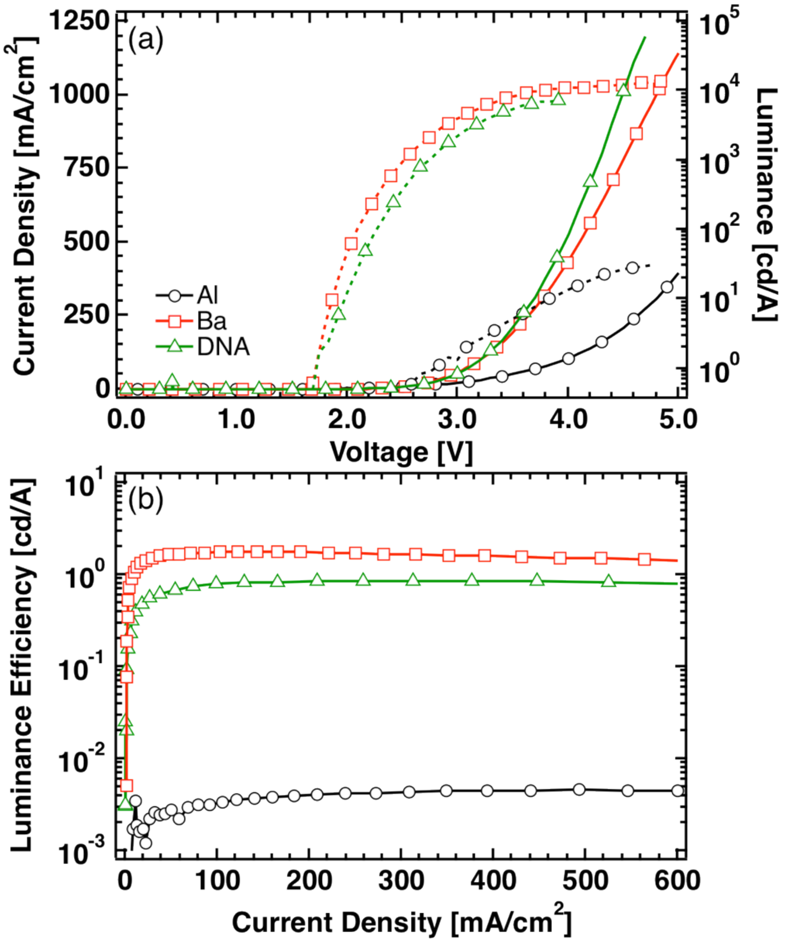

Figure 4.3 (a) *J-V* (closed symbols), *L-V* (open symbols), and (b) luminance efficiency (*LE-J*) characteristics of PLEDs with the structures: ITO/PEDOT:PSS/MEH-PPV/Ba/Al (red squares), ITO/PEDOT:PSS/MEH-PPV/DNA/Al (green triangles), and ITO/PEDOT:PSS/MEH-PPV/Al (black circles).

In order to further understand the mechanism of PLED performance improvement, the time response of DNA/Al and Al devices were examined. This measurement was done by applying a 3.5 V rectangular voltage pulse to the devices and tracking the electroluminescence intensity as a function of time. Details of this experiment appear in the experiment methods as well as previous publications.[20] The result of this measurement appears in Figure 4.4. The time response of MEH-PPV/Al devices, as defined by the time required to read ½ the luminance maximum, was < 1 ms. In contrast, the MEH-PPV/DNA/Al device required 14 ms to achieve the same. It is worth noting that the ratio of luminance in this measurement matches with the luminance ratio obtained by steady-state measurements. These response times suggest that ion motion plays a minor role in enhancing electron injection in these devices.[42] For devices where ion motion was significant, the PLED response time is orders of magnitude higher – taking several seconds.[11] These observations are consistent with the hypothesis that an interfacial dipole between the MEH-PPV and Al contact is responsible for the enhanced charge injection characteristics.

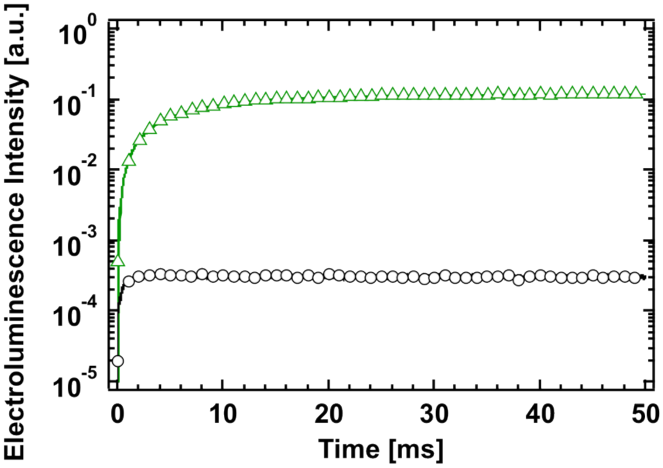

Figure 4.4 The time response of DNA/Al (green triangles) and Al devices (black circles).

To verify that the changes in device performance are not a solvent effect,[28] we analyzed the effect of spin-coating simply the solvent mixture 90:10 MeOH:H_2O atop an MEH-PPV. The *J-V* characteristics are shown in Figure 4.5. Clearly, solvent treatment does not lead to enhanced current densities. This is proof that the DNA layer is what gives rise to enhanced current densities, rather than any effects of the solvent on the emissive layer.

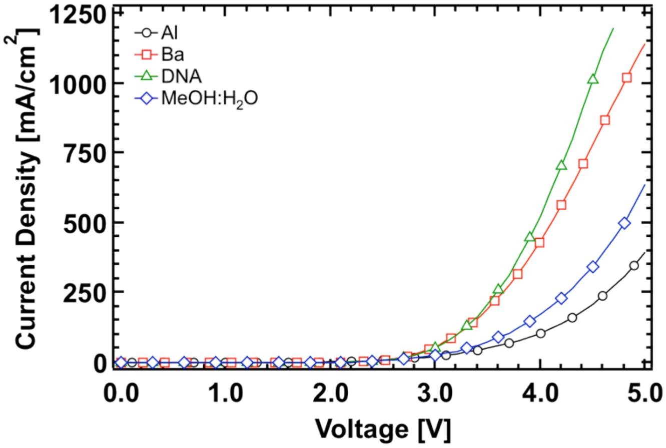

Figure 4.5 The effect of solvent treatment by 90:10 MeOH:H_2O (blue diamonds) on the current density, *J*, of ITO/PEDOT:PSS/MEH-PPV/ devices. Traces for Al (black circles), Ba (red squares), and DNA (green triangles) devices are shown for comparison.

4.3 Thin Film Topologies

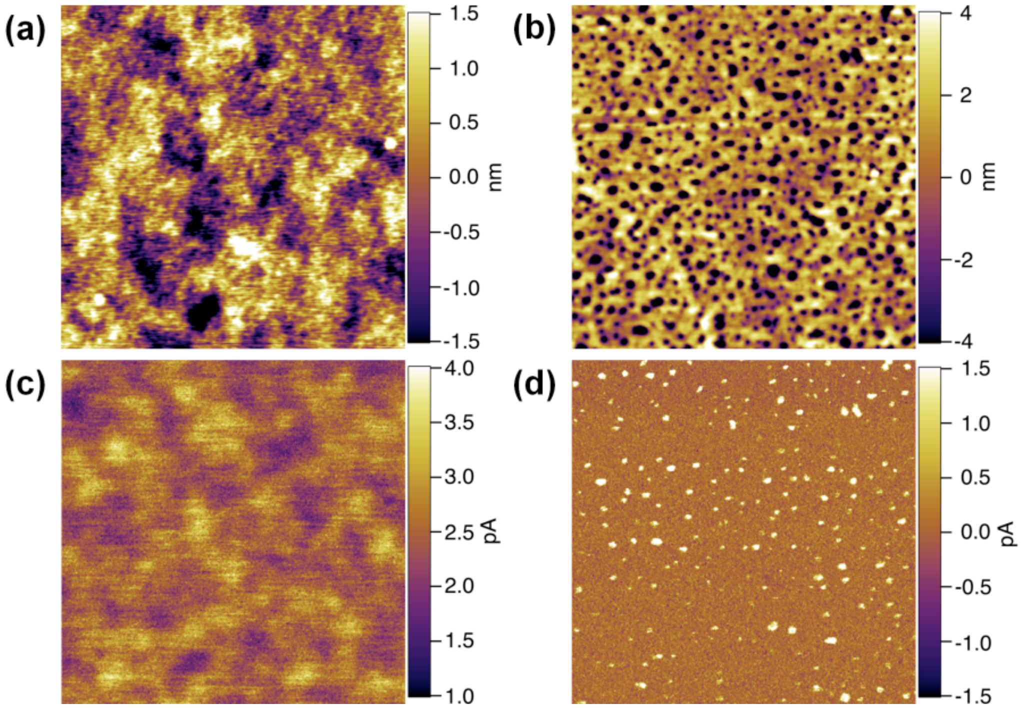

Figure 4.6 The surface topology (a,b) and current measurements of (a,c) MEH-PPV and (b,d) MEH-PPV/DNA surfaces. The voltages used in (c) and (d) were +2 V and +5 V, respectively. The RMS roughness for (a) was 0.8 nm and 2.8 nm for (b).

In order to further understand the effect of the DNA interlayer on the device's function, the surface topology was probed using atomic force microscopy (AFM) and conducting-AFM (c-AFM). Figure 4.6 shows the topology of MEH-PPV/Al and MEH-PPV/DNA/Al devices. The topologies were measured between the Al electrodes. As expected, the MEH-PPV shows a very smooth film with a root-mean-square (RMS) roughness of 0.8 nm. In contrast, the MEH-PPV/DNA films have a web-like topology with pinholes on the order of 12 - 16 nm and an RMS roughness of 2.8 nm. From this measurement, the average DNA thickness is 15 ± 3 nm. The morphology is consistent with poor wetting between the hydrophilic DNA and the hydrophobic MEH-PPV surface. Despite this, the surface morphology does not change even after exposure to moist air for 14 hr (Figure 4.7).[43]

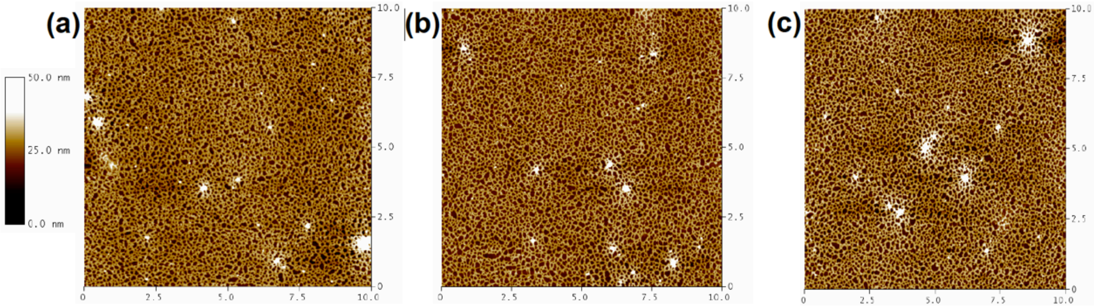

Figure 4.7 Influence of air exposure on the film morphology of 0.1% w/v DNA in 90:10 MeOH:H_2O films on MEH-PPV after (a) 0 hrs (rms: 6.34 nm), (b) 4 hrs (rms: 5.60 nm), and (c) 14 hrs (rms: 6.75 nm) of exposure (10 × 10 µm scans).

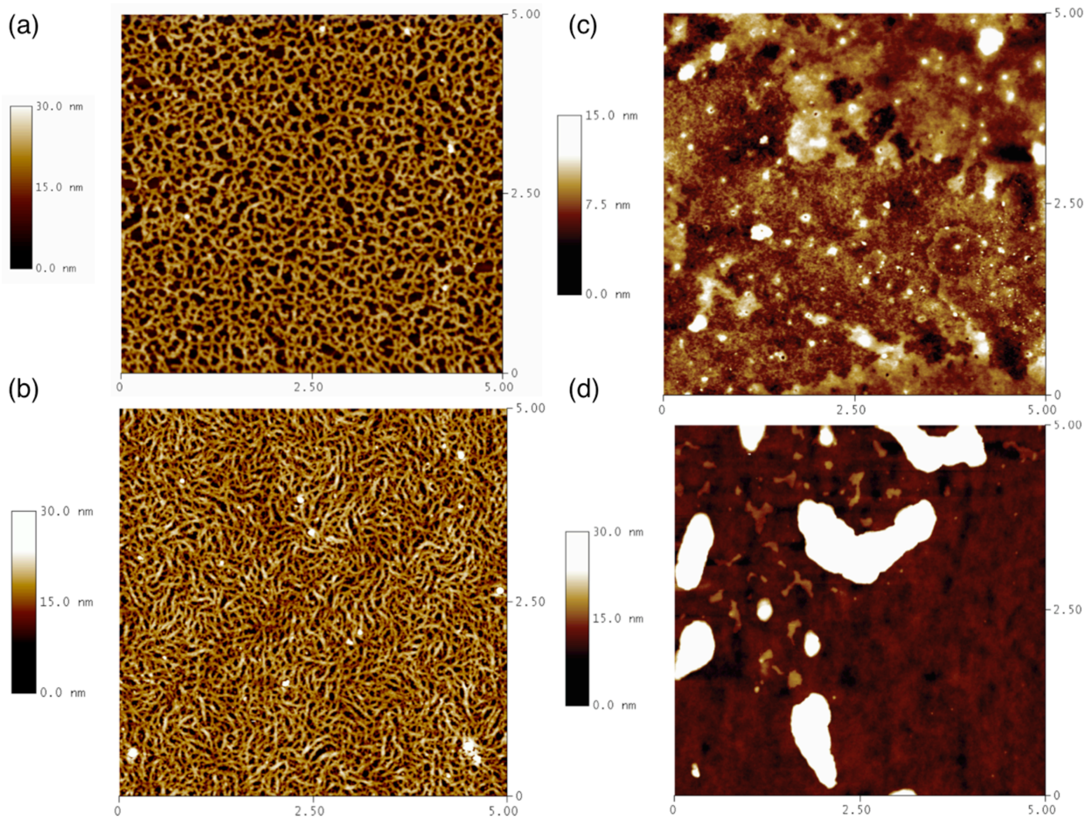

Figure 4.8 Topologies of DNA films atop MEH-PPV processed from 0.1% w/v DNA in 90:10 mixtures of (a) MeOH:H_2O, (b) $(CH_3)_2CO$:H_2O, (c) CH_3CN:H_2O, and (d) MEK:H_2O.

The surface topologies of DNA processed from other conditions are summarized in Figure 4.8. The topologies of all these films, except the $(CH_3)_2CO$:H_2O film are irregular, with many large features strewn across the surface. Nonetheless, as discussed in the previous section, all these topologies led to more or less identical device performances. This is most likely caused by the weak influence of the surface topology on the interfacial dipole effect. The MeOH:H_2O device most likely performed the best due to having the most uniform coverage atop the MEH-PPV surface.

Figure 4.6c and Figure 4.6d shows c-AFM images which were used to gain further insight into the nanoscale conduction characteristics of MEH-PPV and MEH-PPV/DNA films. Using a Au coated AFM tip, one obtains ohmic contact to the highest occupied molecular orbital (HOMO) of MEH-PPV.[44–46] Thus, the c-AFM images illustrate the hole current that travels thorough the MEH-PPV layer. At an applied bias of +2 V, the average current across the MEH-PPV surface of ~2.5 pA is observed. After DNA is spin coated atop the MEH-PPV, almost no current is observed at a bias of +2 V. When the bias is increased to +5 V, the current atop the layer averages at about ~0.1 pA. This current is mainly arising from the pinhole regions shown in Figure 4.5b. These data indicate that DNA covers the majority of the MEH-PPV surface, including a thin-layer within the pinhole regions. The fact that hole current cannot pass through the DNA layer also suggests that the DNA may act as a hole-blocking layer. The device improvement we observe upon processing the DNA layer can be attributed to (a) enhanced electron injection and (b) hole blocking.[47,48] These effects ultimately lead to balanced hole and electron densities and thus enhanced device performance.

4.4 Conclusions

In summary, a naturally occurring and abundant polyelectrolyte, namely, DNA was utilized in order to significantly improve charge injection and device performance in MEH-PPV based PLEDs. Using the DNA interlayer atop the MEH-PPV layer and beneath the Al cathode leads to increases in device efficiencies from 6.5×10^{-3} to 0.80 cd/A.

By comparing the J-V characteristics of Ba and Al controls with DNA/Al devices, there is a clear improvement in the electron injection efficiency. The temporal response of the DNA based devices suggests that ion motion through the DNA layer does little in modifying the electron injection barrier. Rather, it seems that an interfacial dipole layer modifies the effective work function of the Al cathode, leading to superior device performance.

Analysis of the surface topologies of DNA layers shows a web-like morphology rather than amorphous and uniform film. This kind of topology is not unexpected when there is poor wetting that results when depositing a hydrophilic polymer atop a hydrophobic surface. Using c-AFM to map the hole current atop the MEH-PPV layer, it is determined that the DNA layer may also serve as a hole-blocking layer; whereby current was only observed to regions corresponding to pinholes and only at high applied voltage. Since the DNA is anticipated to be insulating towards both electrons and holes, it is reasonable to expect that electrons are injected into MEH-PPV through the *thinnest* parts of the interlayer. This work demonstrates the feasibility of non-conjugated polyelectrolytes for use in organic electronic devices.

4.5 Experimental Methods

General Details: All solvents and metals were obtained from Aldrich and used as received. 18 MΩ water was prepared in the laboratory. DNA was obtained from The Chitose Institute of Science and Technology (CIST) via The Air Force Research Laboratory and stored in a dessicator.

DNA Solution Preparation: DNA solutions were prepared by first dissolving the desired amount of DNA in 18 MΩ water to prevent the introduction of other ions into the solution. The solution is then placed on a vortex mixer at low speed until the solution appears clear. In a glove box, the necessary amount of anhydrous methanol is added. The resulting solution is not heated.

Device Fabrication: Corning 1737 glass substrates patterned with 140 nm of indium-tin-oxide (ITO) was scrubbed thoroughly with detergent and sonicated in water (3x, 10 min), acetone (1x, 30 min), and isopropanol (1x, 30 min). A 60 nm thick layer of poly(3,4-ethylenedioxythiophene):polystyrene sulfonic acid, PEDOT:PSS, (Baytron P 4083, H.C. Starck Inc.) is then spin coated on top of the ITO/glass substrate in air and annealed at 140 °C for 20 min. A ~ 55 nm thick layer of MEH-PPV (Canton OLEDKing Optoelectric Materials Co., Ltd.) was spin coated at 1500 rpm for 60 sec from a 0.5% w/v solution in toluene atop of the PEDOT:PSS layer in nitrogen atmosphere and left to dry for 20 min before deposition of the next layer. DNA solutions were then spin coated using a 0.45 μm polyvinylidene (PVDF) filter atop of the

MEH-PPV layer at 1500 rpm for 60 sec in a nitrogen atmosphere giving an ~ 20 nm thick film with an average thickness of 15 ± 3 nm after accounting for pin-hole depth. After leaving the devices to dry in a 10^{-4} torr vacuum overnight, a 100 nm thick aluminum cathode was deposited by thermal evaporation. Reference devices were made by thermal evaporation of 5 nm of barium capped with 100 nm of aluminum or with 100 nm of aluminum only. OLED devices were tested in nitrogen atmosphere using a Keithley 2602 multimeter coupled with a photodiode. Time response measurements were performed using a Keithley 4200 Semiconductor Characterization System and Si photodiode coupled with a digital oscilloscope (Tektronix).

Atomic Force Microscopy: All atomic force microscopy images were measured under inert atmosphere of nitrogen. Conducting AFM measurements were performed using an Asylum Research MFP-3D. All measurements were done using a nitrogen flow cell. The current was recorded using an internal preamplifier (Asylum Research ORCA head model). Gold-coated silicon probes with a spring constant of 0.2 nNm^{-1} and resonant frequency of 13 kHz (Budget Sensors) was used. Other images were obtained using a MultiMode AFM (Veeco). Silicon probes with a spring constant of ~5 N/m and resonant frequencies of 75 kHz (Budget Sensors) were used for tapping mode measurements.

4.6 References

(1) Ishii, H.; Sugiyama, K.; Ito, E.; Seki, K. *Adv. Mater.* **1999**, *11*, 605–625.

(2) Kahn, A.; Koch, N.; Gao, W. Y. *J. Polym. Sci. Part B-Polym. Phys.* **2003**, *41*, 2529–2548.

(3) Wu, H. B.; Huang, F.; Peng, J. B.; Cao, Y. *Org. Electron.* **2005**, *6*, 118–128.

(4) Shen, Y.; Hosseini, A. R.; Wong, M. H.; Malliaras, G. G. *ChemPhysChem* **2004**, *5*, 16–25.

(5) Malliaras, G. G.; Scott, J. C. *J. Appl. Phys.* **1998**, *83*, 5399–5403.

(6) Friend, R. H.; Gymer, R. W.; Holmes, A. B.; Burroughes, J. H.; Marks, R. N.; Taliani, C.; Bradley, D. D. C.; Dos Santos, D. A.; Bredas, J. L.; Lögdlund, M. *Nature* **1999**, *397*, 121–128.

(7) Broms, P.; Birgerson, J.; Johansson, N.; Logdlund, M.; Salaneck, W. R. *Synth. Met.* **1995**, *74*, 179–181.

(8) Carter, J. C.; Grizzi, I.; Heeks, S. K.; Lacey, D. J.; Latham, S. G.; May, P. G.; delosPanos, O. R.; Pichler, K.; Towns, C. R.; Wittmann, H. F. *Appl. Phys. Lett.* **1997**, *71*, 34–36.

(9) Pfeiffer, M.; Leo, K.; Zhou, X.; Huang, J. .; Hofmann, M.; Werner, A.; Blochwitz-Nimoth, J. *Org. Electron.* **2003**, *4*, 89–103.

(10) Wu, H.; Huang, F.; Mo, Y.; Yang, W.; Wang, D.; Peng, J.; Cao, Y. *Adv. Mater.* **2004**, *16*, 1826–1830.

(11) Hoven, C. V.; Yang, R.; Garcia, A.; Crockett, V.; Heeger, A. J.; Bazan, G. C.; Nguyen, T.-Q. *Proc. Natl. Acad. Sci. U. S. A.* **2008**, *105*, 12730–12735.

(12) Lin, C.-Y.; Garcia, A.; Zalar, P.; Brzezinski, J. Z.; Nguyen, T.-Q. *J. Phys. Chem. C* **2010**, *114*, 15786–15790.

(13) Burgi, L.; Richards, T. J.; Friend, R. H.; Sirringhaus, H. *J. Appl. Phys.* **2003**, *94*, 6129–6137.

(14) Pesavento, P. V.; Puntambekar, K. P.; Frisbie, C. D.; McKeen, J. C.; Ruden, P. P. *J. Appl. Phys.* **2006**, *99*, 094504.

(15) Gong, X.; Wang, S.; Moses, D.; Bazan, G. C.; Heeger, A. J. *Adv. Mater.* **2005**, *17*, 2053–+.

(16) Wetzelaer, G. A. H.; Najafi, A.; Kist, R. J. P.; Kuik, M.; Blom, P. W. M. *Appl. Phys. Lett.* **2013**, *102*, 053301–053301.

(17) Jiang, H.; Taranekar, P.; Reynolds, J. R.; Schanze, K. S. *Angew. Chem.-Int. Ed.* **2009**, *48*, 4300–4316.

(18) Hoven, C. V.; Garcia, A.; Bazan, G. C.; Nguyen, T.-Q. *Adv. Mater.* **2008**, *20*, 3793–3810.

(19) Huang, F.; Wu, H.; Cao, Y. *Chem. Soc. Rev.* **2010**, *39*, 2500–2521.

(20) Yang, R.; Xu, Y.; Dang, X.-D.; Nguyen, T.-Q.; Cao, Y.; Bazan, G. C. *J. Am. Chem. Soc.* **2008**, *130*, 3282–+.

(21) Liu, G.; Li, A.-Y.; An, D.; Wu, H.-B.; Zhu, X.-H.; Li, Y.; Miao, X.-R.; Deng, W.-L.; Yang, W.; Cao, Y.; Roncali, J. *Macromol. Rapid Commun.* **2009**, *30*, 1484–1491.

(22) Pho, T. V.; Zalar, P.; Garcia, A.; Nguyen, T.-Q.; Wudl, F. *Chem. Commun.* **2010**, *46*, 8210–8212.

(23) Hoven, C. V.; Peet, J.; Mikhailovsky, A.; Nguyen, T.-Q. *Appl. Phys. Lett.* **2009**, *94*, 033301.

(24) Ho, P. K. H.; Granstrom, M.; Friend, R. H.; Greenham, N. C. *Adv. Mater.* **1998**, *10*, 769–774.

(25) De Boer, B.; Hadipour, A.; Mandoc, M. M.; van Woudenbergh, T.; Blom, P. W. M. *Adv. Mater.* **2005**, *17*, 621–625.

(26) Winroth, G.; Fenwick, O.; Scott, M. A.; Yip, D.; Howorka, S.; Cacialli, F. *Appl. Phys. Lett.* **2010**, *97*, 043304.

(27) Seo, J. H.; Yang, R.; Brzezinski, J. Z.; Walker, B.; Bazan, G. C.; Nguyen, T.-Q. *Adv. Mater.* **2009**, *21*, 1006–+.

(28) Tan, Z.-K.; Vaynzof, Y.; Credgington, D.; Li, C.; Casford, M. T. L.; Sepe, A.; Huettner, S.; Nikolka, M.; Paulus, F.; Yang, L.; Sirringhaus, H.; Greenham, N. C.; Friend, R. H. *Adv. Funct. Mater.* **2014**, *24*, 3051-3058.

(29) *Physical chemistry of polyelectrolytes*; Radeva, T., Ed.; Surfactant science series; Marcel Dekker: New York, 2001.

(30) Manning, G. S. *Annu. Rev. Phys. Chem.* **1972**, *23*, 117–&.

(31) Dobrynin, A. V.; Rubinstein, M. *Prog. Polym. Sci.* **2005**, *30*, 1049–1118.

(32) Yumusak, C.; Singh, T. B.; Sariciftci, N. S.; Grote, J. G. *Appl. Phys. Lett.* **2009**, *95*, 263304.

(33) Sun, Q.; Chang, D. W.; Dai, L.; Grote, J.; Naik, R. *Appl. Phys. Lett.* **2008**, *92*, 251108.

(34) Hagen, J. A.; Li, W.; Steckl, J.; Grote, J. G. *Appl. Phys. Lett.* **2006**, *88*, 171109.

(35) Kobayashi, N.; Uemura, S.; Kusabuka, K.; Nakahira, T.; Takahashi, H. *J. Mater. Chem.* **2001**, *11*, 1766–1768.

(36) Koyama, T.; Kawabe, Y.; Ogata, N. In *Organic Light-Emitting Materials and Devices V*; Kafafi, Z. H., Ed.; 2002; *4464*, 248–255.

(37) Hirata, K.; Oyamada, T.; Imai, T.; Sasabe, H.; Adachi, C.; Koyama, T. *Appl. Phys. Lett.* **2004**, *85*, 1627–1629.

(38) Singh, T. B.; Sariciftci, N. S.; Grote, J. G. In *Organic Electronics*; Grasser, T.; Meller, G.; Li, L., Eds.; Springer Berlin Heidelberg: Berlin, Heidelberg, 2009; Vol. 223, pp. 73–112.

(39) Steuerman, D. W.; Garcia, A.; Dante, M.; Yang, R.; Lofvander, J. P.; Nguyen, T.-Q. *Adv. Mater.* **2008**, *20*, 528–+.

(40) Wang, C.; Garcia, A.; Yan, H.; Sohn, K. E.; Hexemer, A.; Nguyen, T.-Q.; Bazan, G. C.; Kramer, E. J.; Ade, H. *J. Am. Chem. Soc.* **2009**, *131*, 12538–+.

(41) Blom, P. W. M.; Vissenberg, M. *Mater. Sci. Eng. R-Rep.* **2000**, *27*, 53–94.

(42) Fang, J.; Wallikewitz, B. H.; Gao, F.; Tu, G.; Mueller, C.; Pace, G.; Friend, R. H.; Huck, W. T. S. *J. Am. Chem. Soc.* **2011**, *133*, 683–685.

(43) Chen, Z.; Dang, X.-D.; Gutacker, A.; Garcia, A.; Li, H.; Xu, Y.; Ying, L.; Nguyen, T.-Q.; Bazan, G. C. *J. Am. Chem. Soc.* **2010**, *132*, 12160–12162.

(44) Bozano, L.; Carter, S. A.; Scott, J. C.; Malliaras, G. G.; Brock, P. J. *Appl. Phys. Lett.* **1999**, *74*, 1132–1134.

(45) Lin, H. N.; Lin, H. L.; Wang, S. S.; Yu, L. S.; Perng, G. Y.; Chen, S. A.; Chen, S. H. *Appl. Phys. Lett.* **2002**, *81*, 2572–2574.

(46) Dante, M.; Yang, C.; Walker, B.; Wudl, F.; Nguyen, T.-Q. *Adv. Mater.* **2010**, *22*, 1835–+.

(47) Gruner, J.; Remmers, M.; Neher, D. *Adv. Mater.* **1997**, *9*, 964–+.

(48) Baigent, D. R.; Greenham, N. C.; Gruner, J.; Marks, R. N.; Friend, R. H.; Moratti, S. C.; Holmes, A. B. *Synth. Met.* **1994**, *67*, 3–10.

5.0 Processing Additives for High Performance Organic Field-Effect Transistors

Processing additives have already found extensive use in organic solar cells as a method to increase molecular ordering and achieve higher power conversion efficiencies. In this chapter, this methodology is extended to single-component polymer-based organic field-effect transistors (OFETs). To demonstrate this effect, two different polymers poly(4-(4,4-bis(2-ethylhexyl)-4H-silolo[3,2-b:4,5-b′]dithiophen-2-yl)-[1,2,5]thiadiazolo[3,4-c]pyridine) (**SDT-PT**) and poly(4-(4,4-dihexadecyl-4H-cyclopenta[1,2-b:5,4-b′]dithiophen-2-yl)-[1,2,5]thiadiazolo[3,4-c]pyridine) (**CDT-PT**) are used as the active material in the transistors. The polymers are processed onto the gate dielectric from chlorobenzene (CB) solution in conjunction with several popular processing additives, namely: 1,8-diiodooctane (DIO), 1-chloronapthalene (CN), and 1,8-octanedithiol (ODT). It is shown that the field-effect mobility (μ_h) can be increased while also reducing the threshold voltage (V_t) of the device. These improvements correlate with an increase in the bulk molecular ordering of the polymer, as hypothesized by atomic force microscopy (AFM) images.

5.1 Introduction

Recently, solution processed polymer FETs have been shown to give saturation mobilities in the order of 10^{-1}-10^{1} cm^2/Vs.[1–6] These mobilities make polymer field-effect transistor systems competitive with amorphous silicon and may allow for the fabrication of high speed CMOS circuitry.[7] Processing of organic bulk heterojunction solar cells (BHJ-OSCs) with the addition of a small volume:volume percent of high boiling solvents has become a widespread and standard method for helping to improve the overall performance of devices.[8–12] It has been postulated that addition of these solvent additives helps to improve bulk organization in the BHJ, leading to a significant increase in all device properties such as fill factor, open-circuit voltage, and short-circuit current.[13–15]

So far, this processing methodology has only been applied to donor:acceptor blend systems for BHJ-OSC applications. For single-component systems, i.e. pristine polymer films, most attention has been paid to changing bulk solvents rather than processing from solvent mixtures or using small amounts of solvent additive as in BHJ-OSCs. In OFETs, the active layer-gate dielectric interface plays the biggest role in determining the overall device characteristics since the conduction pathway lays in a zone only several nanometers adjacent to the active layer-dielectric interface.[16] For solution-processed organic FETs, it has been frequently shown that processing conditions significantly influence the organization of individual molecules or polymer chains on the gate dielectric.[17,18] This organization directly affects the bulk electrical properties such as field-effect mobility, on-off ratio, and threshold voltage. Until now, choice of gate dielectric (i.e. polymer dielectric or SiO_2) gate dielectric passivation treatments (i.e. hexamethyldisilazane or octytrichlorosilane treatment), solvent choice, and post-processing thermal annealing are the only approaches that are currently available to help optimize a given material's performance.

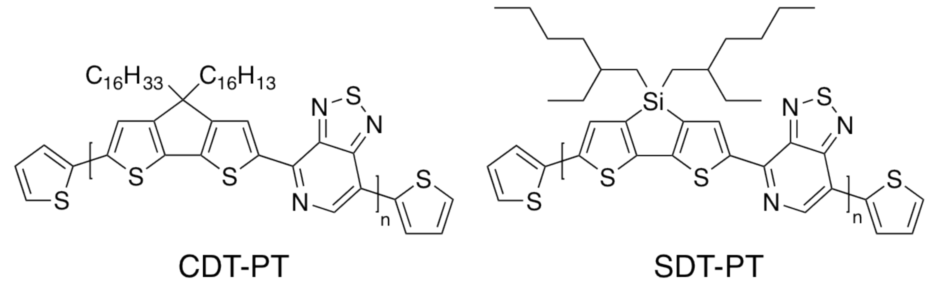

Figure 5.1 The chemical structures of regioregular co-polymers CDT-PT (left) and SDT-PT (right). Both polymers were end-capped with thiophene units.

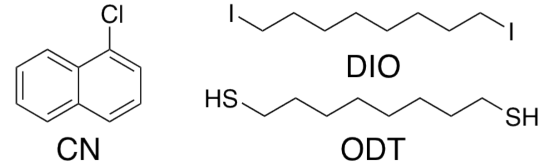

Figure 5.2 The processing additives used in this study: 1-chloronapthalene (CN), 1,8-diiodooctane (DIO), and 1,8-octanedithiol (ODT). All these additives have been commonly used in BHJ-OSC devices.

It is shown that by addition of solvent additives that have seen extensive use in two-component BHJ-OSCs one can also improve the basic performance metrics of single-component polymer FETs. Two different materials were used to verify the effect, namely the regioregular polymers poly(4-(4,4-bis(2-ethylhexyl)-4H-silolo[3,2-b:4,5-b′]dithiophen-2-yl)-[1,2,5]thiadiazolo[3,4-c]pyridine) (**SDT-PT**) and poly(4-(4,4-dihexadecyl-4H-cyclopenta[1,2-b:5,4-b′]dithiophen-2-yl)-[1,2,5]thiadiazolo[3,4-c]pyridine) (**CDT-PT**) (Figure 5.1)[19,20]. The polymers were end-capped, post-synthesis, using thiophene endcaps. The solvent additives of 1-

chloronapthalene (CN), 1,8-diiodooctane (DIO), and 1,8-octanedithiol (ODT) were used to determine the optimal processing additive (Figure 5.2).

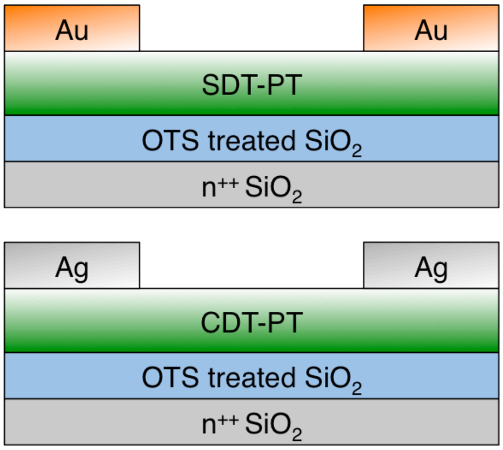

Figure 5.3 The general device structure for bottom gate/top-contact FETs with SDT-PT (top) and CDT-PT (bottom) copolymers as the active layer.

The device structures of the final staggered, bottom-gate/top-contact organic-FETs are shown in Figure 5.3. In general, the device architecture consists of n^{++} Si/SiO_2 (150 nm)/octyltrichlorosilane (OTS)/**SDT-PT** or **CDT-PT**/Au (for **SDT-PT**) or Ag (for **CDT-PT**). The gate electrode is the highly doped n^{++} Si, the gate dielectric is OTS treated thermally grown SiO_2, the active layer is **SDT-PT** or **CDT-PT**, and the source and drain electrodes are defined by the Au (**SDT-PT**) or Ag (**CDT-PT**) contact. For both polymers studied, the output current, saturation mobility (μ_h), threshold voltage (V_t), and I_{on}/I_{off} ratio of the devices can be improved through use of this simple processing technique.

5.2 SDT-PT Devices

First, the influence of different additives on the electrical characteristics of **SDT-PT** based transistors was investigated in bottom-gate, top-contact transistors. The **SDT-PT** layer was processed from 0.25% w/v (2.5 mg/mL) solutions in chlorobenzene (CB) with the necessary volume/volume ratio of additive added. The general device structure is depicted in Figure 5.3. Preliminary studies focused on 1% v/v additions of CN, DIO, and ODT as a way to screen different additives for their effectiveness in enhancing device performance. The *p*-type output characteristics of **SDT-PT** devices processed with and without additives are shown in Figure 5.4. The channel width and length are 1 mm and 70 μm, respectively. The output traces of these devices all show typical behavior, with a linear regime when the drain voltage (V_d) is much less than the gate voltage (V_g) and a saturation regime when V_g is similar to V_d. For clarity, only the curves at V_g = - 60 V are shown.

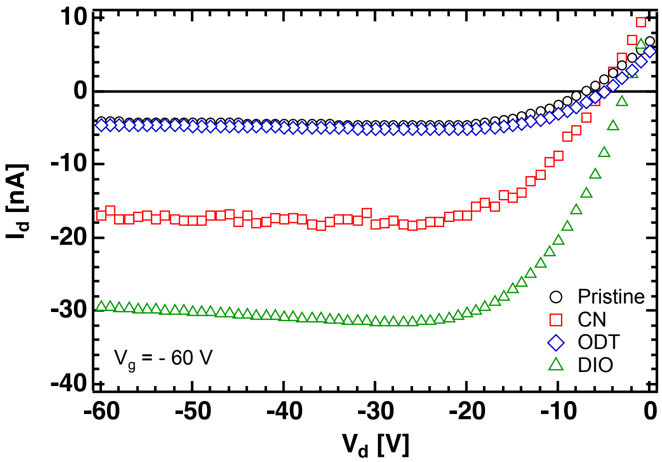

Figure 5.4 The output characteristics of SDT-PT FETs at V_g = -60 V in *p*-mode operation processed in the following conditions: without additive (black circles), with 1% v/v CN (red squares), with 1% v/v ODT (blue diamonds), and with 1% v/v DIO (green diamonds). The channel width and length are 1 mm and 70 µm, respectively.

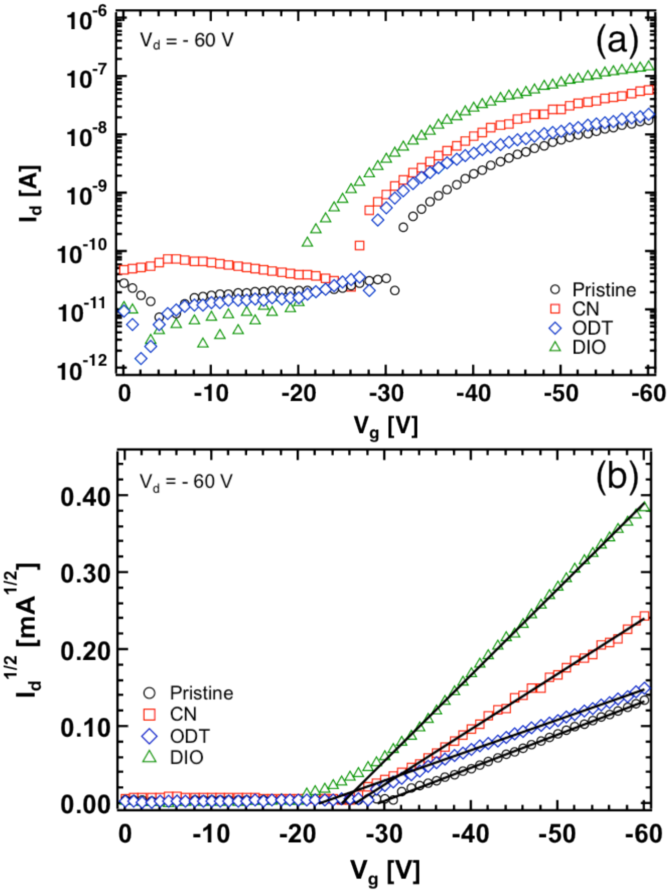

Figure 5.5 The transfer characteristics of SDT-PT transistors processed from pristine solvent (black circles) and with 1% v/v additive additions for CN (red squares), ODT (blue diamonds), and DIO (green triangles). Panel (a) is in log-log to demonstrate changes in the I_{on}/I_{off} ratio. Panel (b) plots $I_d^{1/2}$ and the solid lines are fits to the standard MOS equation (1) to determine μ_h and V_t.

In the output characteristics, processing with additive clearly enhances the observed current in the linear and saturation regimes. For the 1% v/v DIO processed device the drain current (I_d) at V_d = -60 V and V_g = - 60 V is enhanced ~ 7x relative to the control device. For the 1% v/v CN and 1% v/v ODT device, the improvement is ~ 3x and ~ 1x. Naturally, these enhancements in I_d carry over to the transfer characteristics of these devices, which are shown in Figure 5.5.

Using the transfer characteristics in the saturation regime (Figure 5.5) where, $V_d >> V_g - V_t$, one can obtain a more quantitative picture on the effect of additives by virtue of being able to extract figures of merit such as the field-effect mobility (μ_h), V_t and I_{on}/I_{off} ratio. This is achieved through application of the classical metal-oxide-semiconductor equation, Equation (1):[21]

$$\mu_{sat}(V_g) = \frac{2L}{WC_i}\left(\frac{\partial\sqrt{I_d}}{\partial V_g}\right)^2 \tag{1}$$

where I_d is the drain-source current in the saturation regime, V_g is the gate voltage, L is the channel length, W is the channel width, and C_i is the capacitance of the dielectric. The V_t for the devices were extracted from the x-intercept of the fitting line. It is important to note that extraction of mobilities in the saturation or linear regimes do not necessarily reflect an intrinsic property of the semiconductor.

Table 5.1 Parameters extracted from field-effect transistors using SDT-PT as the active layer incorporating different additives. The data was extracted using the transfer characteristics in Figure 5.5.

Condition	μ_h [cm^2/vs]	V_t [V]	I_{on}/I_{off}
Pristine	1.5×10^{-4}	-29	10^3
1% v/v CN	4.2×10^{-4}	-27	10^3
1% v/v ODT	1.3×10^{-4}	-22	10^3
1% v/v DIO	1.0×10^{-3}	-25	10^4

Qualitatively, just as in the output measurements, the I_d measured in the transfer characteristics are enhanced when processing **SDT-PT** with a small amount of additive. A summary of all extracted μ_h, V_t, and I_{on}/I_{off} ratios are shown in Table 5.1. As with the output characteristics, processing with DIO gave the best improvement in all categories relative to the control. The field-effect hole mobility was improved by nearly an order of magnitude, reaching a value of 1.5×10^{-3} cm^2/Vs (DIO) from 1.5×10^{-4} cm^2/Vs (pristine). The threshold voltage of the DIO device was also reduced relative to the pristine solvent device, from -29 V to -25 V. In addition, and mainly a consequence of the increased device current, the I_{on}/I_{off} ratio was also increased by an order of magnitude. The improvement for other additives were less pronounced with CN and ODT giving enhancement factors the hole mobility of ~ 3x and ~ 1x, respectively. These enhancements are identical to those observed in the output I_d.

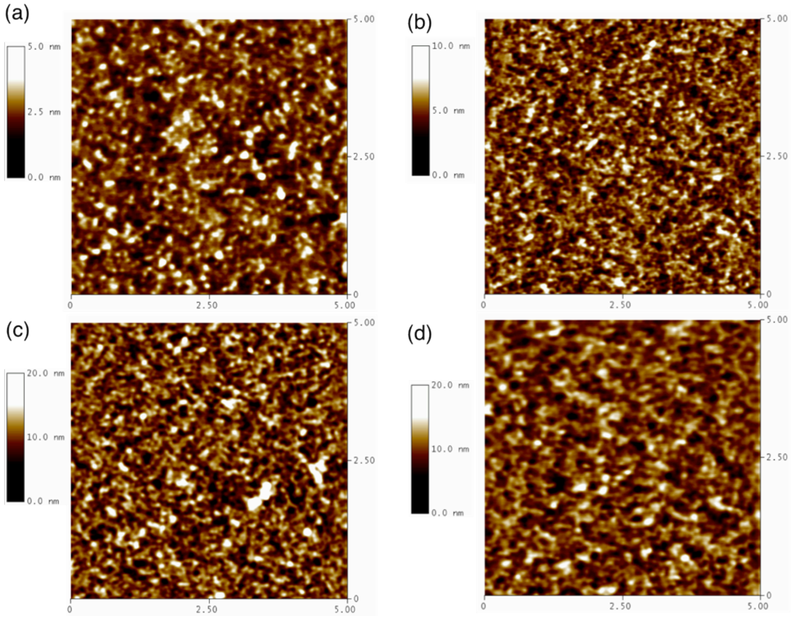

Figure 5.6 The surface topology of SDT-PT devices processed from no additives (a), 1% CN (b), 1% DIO (c), and 1% ODT (d) atop OTS treated SiO_2 substrates. Images were taken in the space between the source and drain electrodes

In order to gain insight into what may be causing the improved device characteristics, atomic force microscopy (AFM) was used to probe the thin-film topologies of **SDT-PT** films processed using the different additives (Figure 5.6). All images were obtained by scanning in between the source and drain electrodes. The surface topologies of each condition may *appear* similar but they all differ in their surface roughness. The film processed from pristine CB has a surface root-mean-square (RMS) roughness of 0.55 nm. The CN film has a surface roughness of 1.0 nm. The ODT film has a surface roughness of 1.1 nm. Surprisingly, the DIO processed film has a surface roughness of 2.2 nm. These observations seem to indicate that the solvent additives have a profound effect on the bulk organization of the polymer during the spin-coating process, ultimately leading to enhanced charge transport behavior in this device geometry.

5.3 CDT-PT Devices

Due to material constraints, attention was turned to the structurally similar **CDT-PT** type regioregular copolymers (Figure 5.1) that have already been shown to achieve very high field-effect mobilities. In this system, the effect of various additives including 3% v/v CN, 1% v/v ODT, and 1% v/vDIO were investigated. Later, attention was focused on the DIO processed system and the behavior was analyzed as a function of v/v ratio of additive. The **CDT-PT** polymer is processed in the same was as the **SDT-PT** polymer, but using Ag as the electrical contact for the source-drain electrodes.

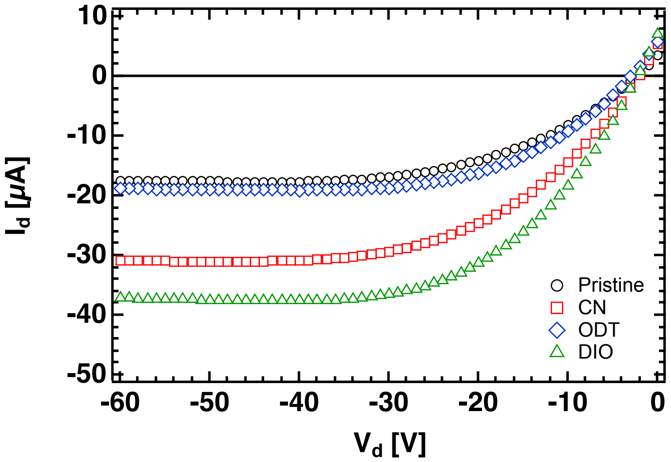

Figure 5.7 The output characteristics of CDT-PT FETs at V_g = -60 V in *p*-mode operation processed in the following conditions: without additive (black circles), with 3% v/v CN (red squares), with 1% v/v ODT (blue diamonds), and with 1% v/v DIO (green diamonds). The channel width and length are 1 mm and 70 µm, respectively.

The *p*-type output characteristics of **CDT-PT** devices processed with and without additives are shown in Figure 5.7. For all devices the channel width and length are 1 mm and 70 µm, respectively. Just as the **SDT-PT** devices, all output traces of these devices all show a linear regime at low V_d followed by a saturation regime at high V_d. For clarity, only the traces for V_g = - 60 V are shown.

As in the **SDT-PT** copolymers, use of additives leaves to enhanced currents in the output characteristics. The DIO processed device has the largest enhancement, with an output current that is ~ 2.0x greater than the control. The enhancement for CN and ODT processed films are minor, with enhancement factors that are only ~1.7x and ~1.1x respectively. The differences for this system are much less pronounced, possibly due to the use of the carbon-bridge rather than the Si-bridge that has been hypothesized to have better potential for higher degrees of molecular order.[22–24]

Again, since the output characteristics gave higher currents, the same improvements are expected in the transfer characteristics (Figure 5.8). Just as in the **SDT-PT** polymer system, a small amount of additive leads to increased μ_h, V_t, and I_{on}/I_{off} ratios. The values extracted for the **CDT-PT** system are summarized in Table 5.2. Just like **SDT-PT**, processing with 1% v/v DIO led to the best overall improvement in device performance but only by a factor of 2x relative to the control (0.44 v. 0.22 cm^2/Vs). The effective threshold voltage of the DIO device was slightly reduced relative to the control, from -9 V to -7 V. For all processing conditions, the I_{on}/I_{off} ratio was very good, at 10^5. The enhancements observed here correlate well with the observed increase in the output I_d.

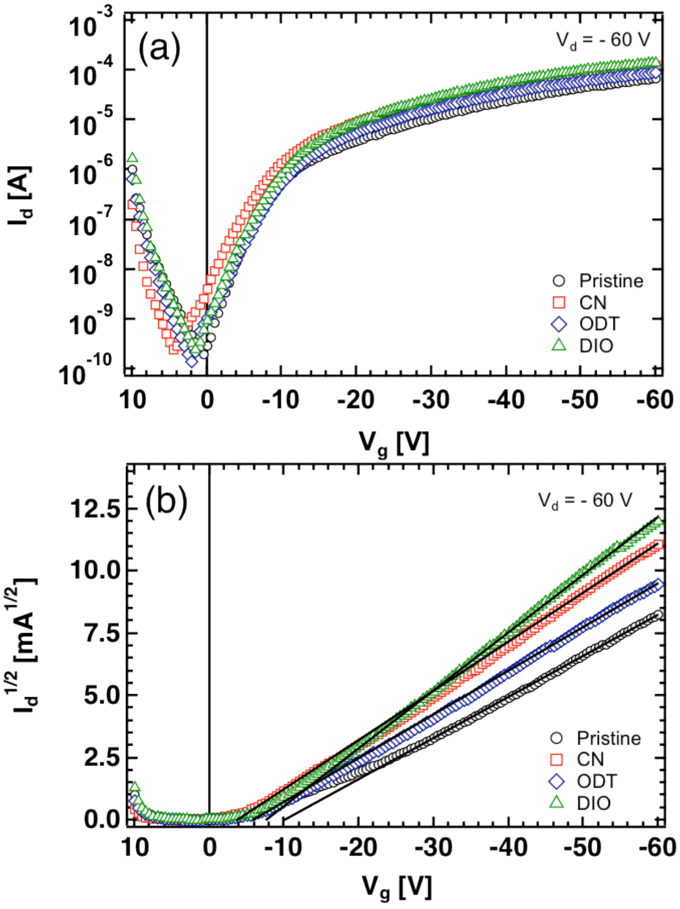

Figure 5.8 The transfer characteristics of CDT-PT transistors processed from pristine solvent (black circles) and with additive additions of 3% v/v CN (red squares), 1% v/v ODT (blue diamonds), and 1% v/v DIO (green triangles). Panel (a) is in log-log to illustrate the I_{on}/I_{off} ratio. Panel (b) plots $I_d^{½}$ and the solid lines are fits to the standard MOS equation (1) used to extract μ_h and V_t.

Table 5.2 Parameters extracted from field-effect transistors using CDT-PT as the active layer incorporating different additives. The data was extracted using the transfer characteristics in Figure 5.8.

Condition	μ_h [cm^2/Vs]	V_t [V]	I_{on}/I_{off}
Pristine	0.22	-9	10^5
3% v/v CN	0.32	-4	10^5
1% v/v ODT	0.25	-6	10^5
1% v/v DIO	0.44	-7	10^5

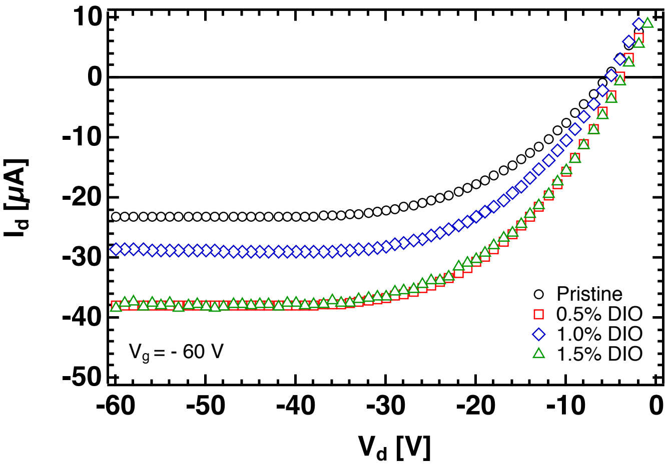

Figure 5.9 The output characteristics of CDT-PT FETs at V_g = -60 V in *p*-mode operation processed in the following conditions: without additive (black circles), with 0.5% (red squares), 1.0% (blue diamonds), and 1.5% v/v DIO (green diamonds). The channel width and length are 1 mm and 70 µm, respectively.

Since processing **CDT-PT** using DIO as an additive gave the best results in the comparative study above, the effect of different v/v ratios of DIO was investigated. For this study, the DIO v/v was varied between pristine solvent, 0.5%, 1.0%, and 1.5% v/v DIO. In this set of parallel experiments, the best improvements in output characteristics (Figure 5.9) were achieved with 0.5% and 1.5% DIO, with an enhancement factor of ~1.7x in the saturation regime I_d. This is close to the result obtained in the previous additive-screening experiment where this improvement is only marginal.

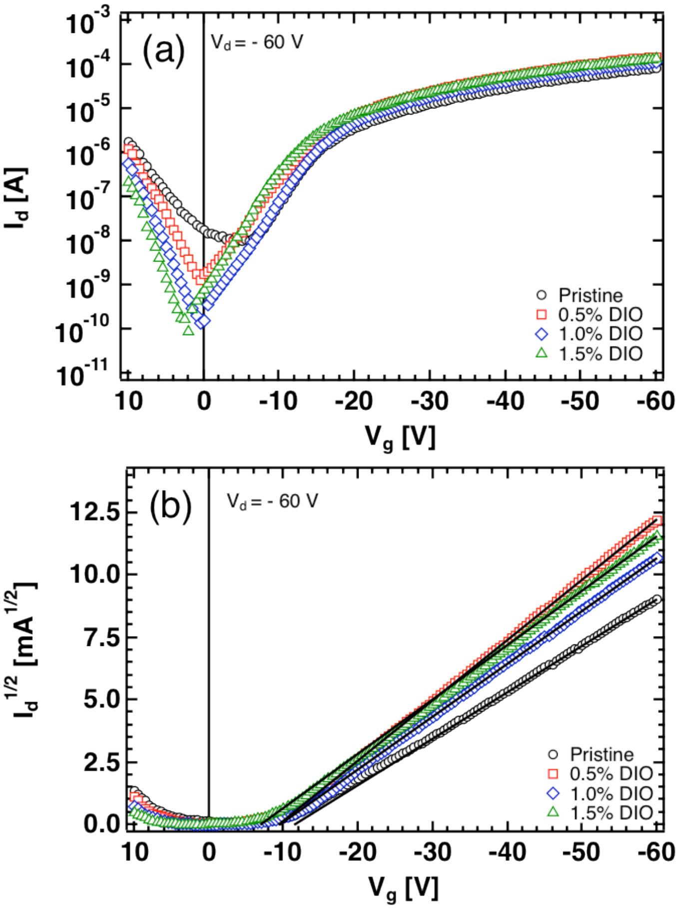

Figure 5.10 The transfer characteristics of CDT-PT transistors processed from pristine solvent (black circles) and without additive (black circles), with 0.5% (red squares), 1.0% (blue diamonds), and 1.5% v/v DIO (green diamonds). The channel width and length are 1 mm and 70 µm, respectively. Panel (a) is in log-log to illustrate the I_{on}/I_{off} ratio. Panel (b) plots $I_d^{1/2}$ and the solid lines are fits to the standard MOS equation (1) used to extract μ_h and V_t.

Table 5.3 Parameters extracted from field-effect transistors using CDT-PT as the active layer incorporating different amounts of DIO additive. The data was extracted using the transfer characteristics in Figure 5.10.

Condition	μ_h [cm^2/Vs]	V_t [V]	I_{on}/I_{off}
Pristine	0.28	-11	10^3
0.5% DIO	0.47	-9	10^4
1.0% DIO	0.36	-9	10^5
1.5% DIO	0.38	-7	10^5

In the transfer characteristics (Figure 5.10), the same analysis was performed as in the previous experiments. Table 5.3 summarizes the parameters obtained for the *best* devices in the DIO v/v study. The μ_h and V_t for the 1% addition was not identical but slight variations in these parameters are expected from experiment to experiment. The field-effect mobility was increased with the same factor as the output current for 0.5% DIO – 1.7x. The same improvement was found for 1.5% additions. The 1.0% addition only gave an improvement of 1.3x. In this group of experiments, treatment with DIO leads to enhancements in the I_{on}/I_{off} ratio, which was not observed in the previous set of experiments. This may be caused by variations in the surface treatment quality. To show that this effect is also statistically significant, the average mobilities ± one standard deviations on the substrate for these conditions are plotted as a function of DIO addition in Figure 5.11.

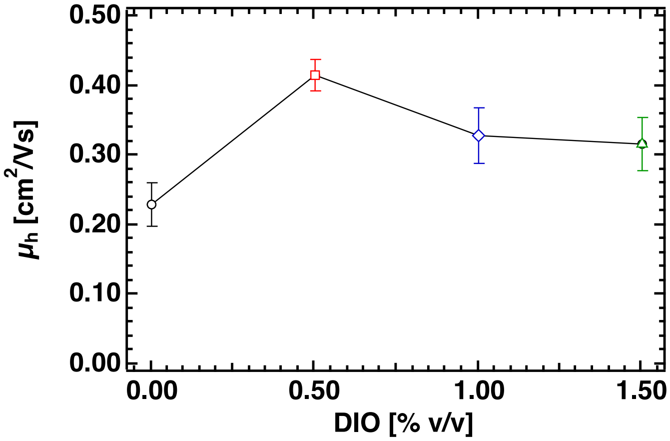

Figure 5.11 Plot of μ_h as a function of % v/v DIO. The error bars represent one standard deviation.

In order to see if addition of DIO led to changes in surface topology the films were probed using AFM. In Figure 5.12, the surface topology of (a) additive-free and (b) 0.5% v/v DIO processed devices. The surfaces of the two films are slightly different, but their differences can be quantified by analyzing the RMS surface roughness. For the device processed with DIO, the RMS roughness is 1.8 nm, while for the additive-free device it is 1.0 nm. This is in agreement with the measurements of the **SDT-PT** system where use of processing additives also resulted in rougher films. In general, this can be correlated with changes in solid-state ordering, which potentially give rise to the enhanced device performance.

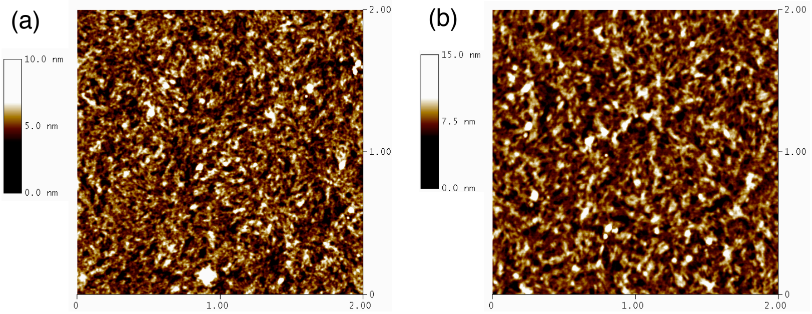

Figure 5.12 The surface topology of CDT-PT devices processed from no additives (a) and from 0.5% DIO (b) atop OTS treated SiO_2 substrates. Images were taken in the space between the source and drain electrodes.

5.4 Conclusions

To conclude, it was shown that addition of a small amount of a high boiling point solvent additive, such as the ones used in organic BHJ solar cells, can lead to significant changes in the operation of the device. Compared to processing from pristine solvents (i.e. 100% chlorobenzene), a small amount of processing additive led to enhancements to many figures of merit for FETs: higher μ_h, lower V_t, and higher I_{on}/I_{off} ratio. This effect was demonstrated using two different polymer systems using a variety of additives that included CN, ODT, and DIO. It was shown that for both systems, addition of the additive led to increased surface roughness that was attributed to changes in the bulk ordering of the polymer.

Future work on this topic should focus on two main aspects. The first would be to do further characterization of the films by x-ray scattering techniques such as grazing incidence wide-angle scattering (GIWAXS). These measurements would shed more light as to the true orientation of the polymer within the bulk of the film and at the dielectric interface. More importantly, this would give researchers a more fundamental handle on understanding the role that additives play in changing molecular ordering and orientation. Most work has so far been done on organic BHJ solar cells that involve two components, complicating the problem. The other aspect would be on optimization of additive choice and additive concentration to arrive at the optimum performance for the given system. This may allow for access of better device performance beyond conventional processing.

5.5 Experimental Methods

General Details: All chemicals and metals were obtained from Acros Organics and used as received. Polymers were obtained from the group of Professor Guillermo C. Bazan (UCSB). Experimental details for the synthesis of **SDT-PT** and **CDT-PT** appear in reference 19 and 20.

Field-Effect Transistor Fabrication and Testing: FETs were made using a bottom-gate, top contact architecture. The gate electrode was n^{++} doped Si with 150 nm thick SiO_2 serving as the gate dielectric (WRS Materials). The SiO_2 dielectric was passivated by treatment with octyltrichlorosilane (OTS). This passivation layer minimizes trapping at the polymer-dielectric interface changes the surface energy, instilling a more hydrophobic character at the polymer-dielectric interface. The OTS treatment procedure appears below in its own subsection. For film processing, 0.25% w/v solutions of **SDT-PT** or **CDT-PT** were prepared in CB solution and the necessary v:v ratio of the desired solvent additive was added. These solutions were kept at 80 °C prior to use. All solutions were spin cast onto the OTS treated SiO_2 substrates at 2000 rpm for 60 seconds. After spin coating, all films were annealed at 80 °C for 10 minutes. 60 nm thick Au (**SDT-PT**) or Ag (**CDT-PT**) source-drain electrodes were subsequently thermally deposited atop the polymer film. The source-drain electrodes were either 1 mm or 2 mm wide and the channel length was 70 μm. The electrical characteristics were measured using a Keithley 4200 Semiconductor Characterization System in a vacuum probe station (Lakeshore Cryotonics).

Octyltrichlorosilane Treatment: All OTS treatment is performed in a glove box atmosphere of N_2. Into a clean and dry bottle, 15 μL of OTS is added to 15 mL of anhydrous hexanes and mixed well. The SiO_2 substrates are placed in a petri dish and immersed in the OTS solution prepared in the bottle for 20 minutes. The substrates are then, one-by-one, rinsed by 3 helpings of 100 μL of hexanes. The substrates are then dried at 80 ºC for 10 minutes to remove residual hexanes from the surface.

Atomic Force Microscopy: All atomic force microscopy images were measured under inert atmosphere of nitrogen. Silicon probes with a spring constant of ~5 N/m and resonant frequencies of 75 kHz (Budget Sensors) were used for tapping mode measurements. Measurements were performed using a MultiMode AFM (Veeco).

5.6 References

(1) Li, J.; Zhao, Y.; Tan, H. S.; Guo, Y.; Di, C.-A.; Yu, G.; Liu, Y.; Lin, M.; Lim, S. H.; Zhou, Y.; Su, H.; Ong, B. S. *Sci. Rep.* **2012**, *2,* 1.

(2) Tseng, H.-R.; Phan, H.; Luo, C.; Wang, M.; Perez, L. A.; Patel, S. N.; Ying, L.; Kramer, E. J.; Nguyen, T.-Q.; Bazan, G. C.; Heeger, A. J. *Adv. Mater.* **2014**, *26*, 2993-2998.

(3) Minemawari, H.; Yamada, T.; Matsui, H.; Tsutsumi, J.; Haas, S.; Chiba, R.; Kumai, R.; Hasegawa, T. *Nature* **2011**, *475*, 364–367.

(4) Diao, Y.; Tee, B. C.-K.; Giri, G.; Xu, J.; Kim, D. H.; Becerril, H. A.; Stoltenberg, R. M.; Lee, T. H.; Xue, G.; Mannsfeld, S. C. B.; Bao, Z. *Nat. Mater.* **2013**, *12*, 665–671.

(5) Li, Y.; Sonar, P.; Murphy, L.; Hong, W. *Energy Environ. Sci.* **2013**, *6*, 1684–1710.

(6) Sun, B.; Hong, W.; Yan, Z.; Aziz, H.; Li, Y. *Adv. Mater.* **2014**, *26*, 2636-2642.

(7) Sirringhaus, H. *Adv. Mater.* **2014**, *26*, 1319–1335.

(8) Peet, J.; Kim, J. Y.; Coates, N. E.; Ma, W. L.; Moses, D.; Heeger, A. J.; Bazan, G. C. *Nat. Mater.* **2007**, *6*, 497–500.

(9) Sun, Y.; Welch, G. C.; Leong, W. L.; Takacs, C. J.; Bazan, G. C.; Heeger, A. J. *Nat. Mater.* **2011**, *11*, 44–48.

(10) Hoven, C. V.; Dang, X.-D.; Coffin, R. C.; Peet, J.; Nguyen, T.-Q.; Bazan, G. C. *Adv. Mater.* **2010**, *22*, E63–E66.

(11) Yiu, A. T.; Beaujuge, P. M.; Lee, O. P.; Woo, C. H.; Toney, M. F.; Fréchet, J. M. J. *J. Am. Chem. Soc.* **2012**, *134*, 2180–2185.

(12) Van der Poll, T. S.; Love, J. A.; Nguyen, T.-Q.; Bazan, G. C. *Adv. Mater.* **2012**, *24*, 3646–3649.

(13) Love, J. A.; Proctor, C. M.; Liu, J.; Takacs, C. J.; Sharenko, A.; van der Poll, T. S.; Heeger, A. J.; Bazan, G. C.; Nguyen, T.-Q. *Adv. Funct. Mater.* **2013**, *23*, 5019–5026.

(14) Perez, L. A.; Chou, K. W.; Love, J. A.; van der Poll, T. S.; Smilgies, D.-M.; Nguyen, T.-Q.; Kramer, E. J.; Amassian, A.; Bazan, G. C. *Adv. Mater.* **2013**, *25*, 6380–6384.

(15) Rogers, J. T.; Schmidt, K.; Toney, M. F.; Kramer, E. J.; Bazan, G. C. *Adv. Mater.* **2011**, *23*, 2284–2288.

(16) Facchetti, A.; Yoon, M.-H.; Marks, T. J. *Adv. Mater.* **2005**, *17*, 1705–1725.

(17) Don Park, Y.; Lim, J. A.; Lee, H. S.; Cho, K. *Mater. Today* **2007**, *10*, 46–54.

(18) Tantiwiwat, M.; Tamayo, A.; Luu, N.; Dang, X.-D.; Nguyen, T.-Q. *J. Phys. Chem. C* **2008**, *112*, 17402–17407.

(19) Ying, L.; Hsu, B. B. Y.; Zhan, H.; Welch, G. C.; Zalar, P.; Perez, L. A.; Kramer, E. J.; Nguyen, T.-Q.; Heeger, A. J.; Wong, W.-Y.; Bazan, G. C. *J. Am. Chem. Soc.* **2011**, *133*, 18538–18541.

(20) Bazan, G. C.; Nguyen, T. Q.; Ying, L.; Zalar, P.; Zhang, Y. Processing additive for single-component solution processed organic field-effect transistors, October 24, 2013.

(21) Sze, S. M. *Physics of semiconductor devices*; 3rd ed.; Wiley-Interscience: Hoboken, N.J, 2007.

(22) Guilbert, A. A. Y.; Frost, J. M.; Agostinelli, T.; Pires, E.; Lilliu, S.; Macdonald, J. E.; Nelson, J. *Chem. Mater.* **2014**, *26*, 1226–1233.

(23) Chen, H.-Y.; Hou, J.; Hayden, A. E.; Yang, H.; Houk, K. N.; Yang, Y. *Adv. Mater.* **2010**, *22*, 371–375.

(24) Morana, M.; Azimi, H.; Dennler, G.; Egelhaaf, H.-J.; Scharber, M.; Forberich, K.; Hauch, J.; Gaudiana, R.; Waller, D.; Zhu, Z.; Hingerl, K.; van Bavel, S. S.; Loos, J.; Brabec, C. J. *Adv. Funct. Mater.* **2010**, *20*, 1180–1188.

6.0 Enantiopure Side Chain Containing Polymers for Field-Effect Transistors

The racemic and enantiopure regioregular polymers, poly(4-(4,4-bis(2-ethylhexyl)-4H-cyclopenta[1,2-b:5,4-b′]dithiophen-2-yl)-[1,2,5]thiadiazolo[3,4-c]pyridine (**P1**) and poly(4-(4,4-bis((S)-2-ethylhexyl)-4H-cyclopenta[1,2-b:5,4-b′]dithiophen-2-yl)-[1,2,5]thiadiazolo[3,4-c]pyridine (**P1S**), were studied in the solution and solid-state to determine differences in the aggregation behavior. UV-Vis spectroscopy and circular dichroism were used to characterize the fraction and chirality aggregates. Atomic force microscopy (AFM) was used to see if these differences were transferred at all to the solid-state. Finally, field-effect transistors (FETs) were fabricated as a means to see if minor differences in aggregation created by the enantiopure side-chains led to differences in electrical performance. It was found that in these devices, regioregular polymers with enantiopure side-chains outperformed the racemic analogues. In this work, the racemic and enantiopure polymers were provided by Dr. Lei Ying from the group of Professor Guillermo C. Bazan at UCSB.

6.1 Introduction

Polymer design for FET applications has often emphasized the importance of regioregular and/or rigid polymer repeat units.[1] These desirable properties can be achieved using ladder-type structures such as the ones proposed by the Swager group at the Massachusetts Institute of Technology.[2] This can also be achieved by careful selection of polymerization catalyst, leading to 100% head-to-tail couplings as has been exploited to realize highly regioregular poly(3-hexylthiophene-2,5-diyl).[3,4] The final structural motif where 'regularity' can be imparted is in the solubilizing chain.

Recently, synthesis of regioregular cyclopentaditophene-pyridylthiadiazole donor-acceptor type conjugated copolymers, with C12-alkyl side chains showed high hole mobilities of ~ 0.1 cm^2/Vs.[5] It was reported that increasing the molecular weight of these types of polymers may lead to higher field-effect mobilities, but solubility became more limited, necessitating a longer C16-alykl side-chain. Using this polymer structure, hole mobilities could range between 0.7 and 1.9 cm^2/Vs simply by increasing the molecular weight from 30 kDa to 300 kDa.[6]

To further increase the solubility of the polymers, a well-known method is to use 2-ethylhexyl side chains. The bulky nature and more rotational degrees of freedom given by this side chain reduces interchain interactions.[7] The shorter length of these alkyl chains versus the C12 or C16 chains should also lead to reduced π-π stacking distances. Of course, substitution of an ethyl group at the 2 position of the hexyl chain creates a chiral center on the compound. Most reports on conjugated polymers bearing a 2-ethylhexyl side chain do not focus on the chirality of this side-chain, presumably due to the commercial availability of the racemic precursor.

Chirality in conjugated polymers has been taken advantage of, notably for the polyfluorene family of polymers, to arrive at new morphologies and polarized absorption and photoluminescence properties for applications in organic solar cells and polymer light-emitting diodes.[8–12] However, no work has sought to take advantage of these different isomers for their electrical properties.

In this work, the racemic and enantiopure regioregular polymers, poly(4-(4,4-bis(2-ethylhexyl)-4H-cyclopenta[1,2-b:5,4-b′]dithiophen-2-yl)-[1,2,5]thiadiazolo[3,4-c]pyridine (**P1**) and poly(4-(4,4-bis((S)-2-ethylhexyl)-4H-cyclopenta[1,2-b:5,4-b′]dithiophen-2-yl)-[1,2,5]thiadiazolo[3,4-c]pyridine (**P1S**), endcapped with thiophene were studied. Their chemical structures are shown in **Figure 6.1**. The synthesis of these polymers was carried out by Dr. Lei Ying in the group of Professor Guillermo C. Bazan (UCSB) and is described both in reference 13. It should be specifically noted that the samples studied herein have nearly identical molecular weights/polydispersity indices of 37 kDa/1.9 for **P1** and 35 kDa/1.9 for **P1S**.

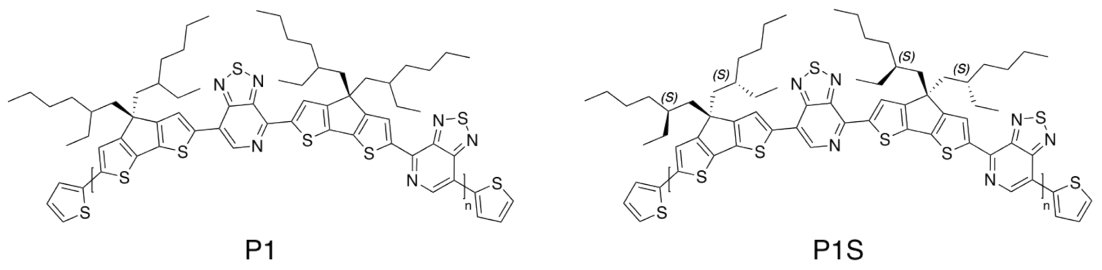

Figure 6.1 Chemical structures of regioregular polymers: racemic P1 (left) and enantiopure P1S (right).

6.2 Optical Properties

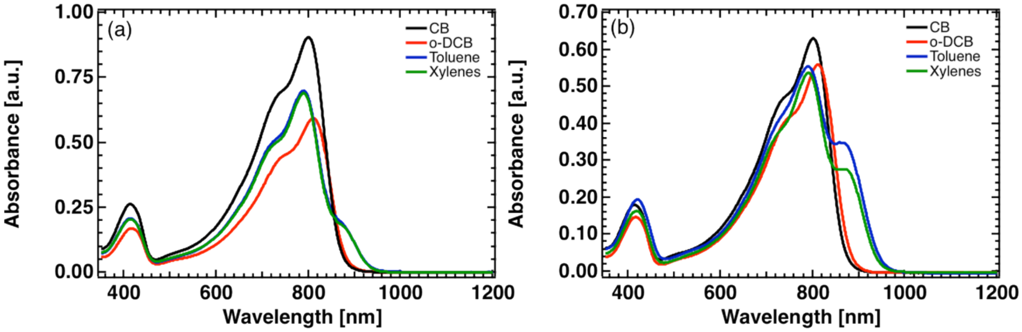

Figure 6.2 The UV-visible spectra of 6.7 × 10^{-3} mg/mL P1 (a) or P1S (b) at room temperature in CB (black line), o-DCB (red line), toluene (blue line), and xylenes (green line).

In Figure 6.2, the UV-visible spectra of **P1** and **P1S** at a concentration of 6.7 × 10^{-3} mg/mL are shown in solvents of chlorobenzene (CB), o-dichlorobenzene (o-DCB), toluene, and xylenes. In CB and o-DCB, the polymers are well dissolved and, as expected, **P1** and **P1S** exhibit very similar absorption profiles with absorbance maxima (λ_{max}) at ~ 800 nm and absorption onsets (λ_{onset}) of ~ 900 nm. However, after dissolving the polymers in poorer solvents such as toluene or xylenes, aggregation signals emerge, corresponding to the emergence of a shoulder with λ_{max} of ~ 865 nm and an extension λ_{onset} of both polymers to about 960 nm. The λ_{max} in toluene and xylene are both ~ 790 nm. When comparing the aggregation behavior of **P1** and **P1S** in toluene and xylenes, **P1S** has comparatively stronger aggregation behavior. This suggests that the 2-(S)-ethylhexyl side chains in **P1S** facilitate formation of ordered secondary structures in solution.[14]

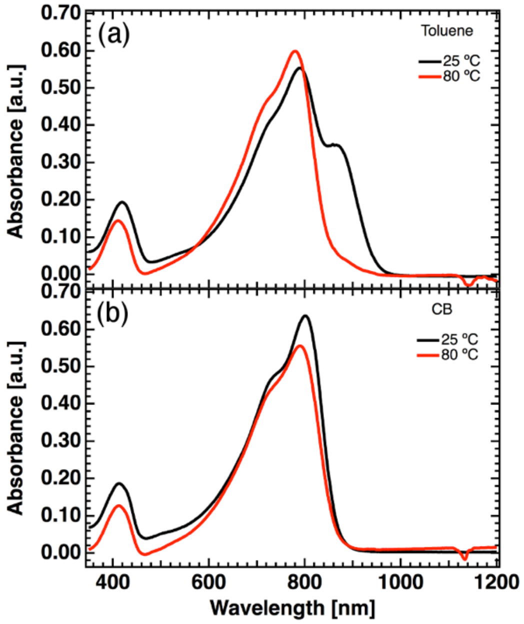

Figure 6.3 Effect of temperature on the UV-vis spectra of P1S in toluene (a) and CB (b) at a concentration of 6.7 × 10^{-3} mg/mL. The negative dip in the 80 ºC spectra at 1130 nm is an artifact of the instrument.

To verify that the shoulder that emerges at ~ 865 nm is caused by aggregation behavior, the temperature dependent absorption spectra were analyzed (Figure 6.3). **P1S** in CB at 25 ºC and 80 ºC have nearly identical absorption profiles, a testament to the fact that CB is a 'good solvent' for P1S and that the molecular chains are extended even at room temperature. In toluene, the behavior is much different. By heating the solution to 80 ºC, the aggregation shoulder present in the 25 ºC spectrum at ~ 865 nm is almost completely removed. This is caused by dissociation of aggregates by increased molecular vibrations.[14]

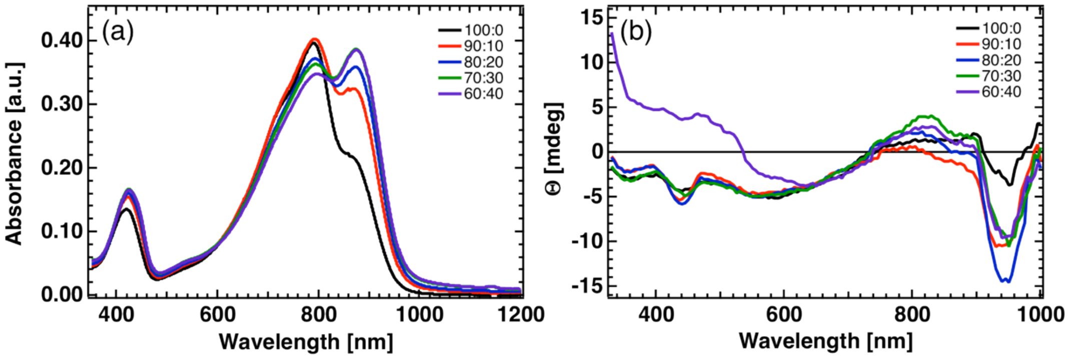

Figure 6.4 The UV-visible spectra (a) and CD spectra (b) of P1S in toluene:MeOH mixtures of 100:0 (black line), 90:10 (red line), 80:20 (blue line), 70:30 (green line), and 60:40 (purple line) at a concentration of 6.7 × 10^{-3} mg/mL.

In order to further aggregate **P1S** in solution, toluene (poor solvent) and methanol (non-solvent, MeOH) were mixed together in 100:0, 90:10, 80:20, 70:30, and 60:40 toluene:MeOH ratios.[15] Addition of 50:50 MeOH causes the polymer is crash out of solution, which is why further additions were not explored. The UV-visible spectra of these mixtures are shown in Figure 6.4a. With increasing MeOH content the peak at ~ 790 nm is slightly reduced while the aggregate peak centered at ~ 875 nm is increased. This is direct indication that addition of MeOH solvent potentially results in a higher population of ordered secondary structures. To further verify this, circular dichroism (CD) was used to probe the chirality of any aggregates that exist in solution (Figure 6.4b).[16] The CD signals are weak, but still show bands that correlate well to UV-visible spectra. As the MeOH is increased, the negative CD peak at 940 nm is increased. A negative cotton effect is also observed at ~ 440 nm, corresponding to the high-energy band in absorption. The slightly positive signal observed for the 60:40 trace suggests that the aggregates are (S), as expected from the chirality of the side chain.

6.3 Surface Topology

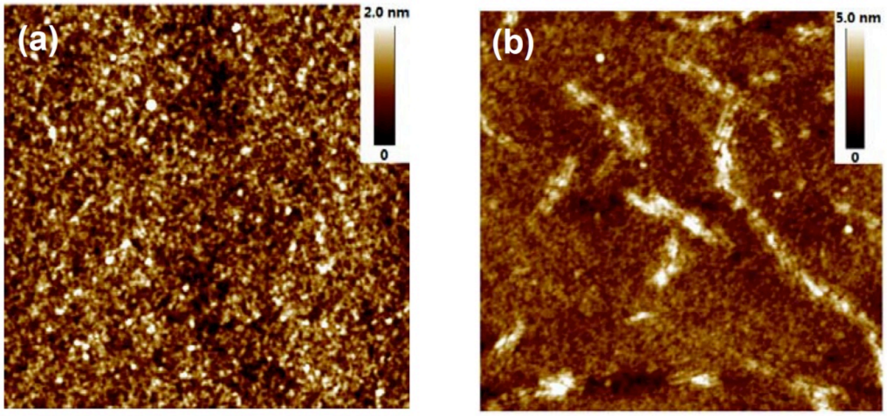

Figure 6.5 Tapping mode AFM images of P1 (a) and P1S (b) films cast from CB on SiO_2/OTS substrates. The scan size is 1 × 1 µm.

In order to see if chiral aggregates could be transferred into a solid-state film, atomic force microscopy (AFM) was used to probe the surface topology of **P1** and **P1S** films.[9] Due to poor solubility of **P1** and **P1S** in toluene, toluene:MeOH, and xylenes at concentrations more typical of device fabrication (2-5 mg/mL), films were processed from room temperature solutions of **P1** and **P1S** at 0.25% w/v (2.5 mg/mL) in CB. The solutions were deposited on octyltrichlorosilane (OTS) treated SiO_2; a traditional surface for field-effect transistor applications. Though the absorption spectra of **P1** and **P1S** are similar in solution (Figure 6.1), the surface topology can be drastically changed (Figure 6.5).

The surface topologies of **P1S** films show a high concentration of fiber-like structures strewn all across the surface.[17] The root-mean-square (RMS) roughness of the films, taking into account the regions between the fibers, is 0.69 nm. The fibers themselves are approximately 85 nm wide, on average. In contrast, the films of **P1** appear featureless and amorphous with a RMS roughness of only 0.39 nm. One would expect that these surface properties should correspond to changes in electrical properties; [18,19] this is the focus in the next subsection.

6.4 Field-Effect Transistors

Due to the limited solubility of the polymers, it is not possible to fabricate single-carrier diodes, thus, field-effect transistors (FETs) were used to determine if the presence of chiral aggregates in the film positively influenced the electrical characteristics of the polymer relative to the racemic polymer.[20] This is due to the fact that the active layer can be just a few nanometers thick. To this end, bottom-gate, top-contact field effect transistors were fabricated. Devices were made using a structure of n++ Si/SiO_2 (150 nm)/OTS/**P1** or **P1S**/Au (60 nm). The n^{++} Si is the gate electrode, SiO_2 is the gate dielectric, OTS is the passivation layer, and the Au metal forms the source-drain electrodes. The channel width was 2 mm and the channel length was 70 μm. As in the AFM experiments, films of **P1** or **P1S** were processed from 0.25% w/v solutions in CB. The films were annealed at 80 ºC for 10 minutes prior to source-drain electrode deposition.

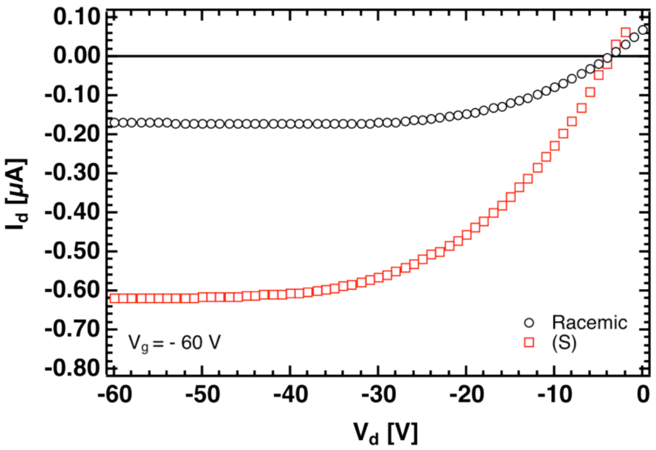

Figure 6.6 The output characteristics of P1 (black circles) and P1S (red squares) FETs at V_g = - 60 V in *p*-mode operation. The channel width and length are 2 mm and 70 µm, respectively.

Figure 6.6 shows the *p*-type output traces for **P1** and **P1S** devices. For clarity, only the characteristics at a gate voltage, V_g, equal to - 60 V are shown; in general all devices showed typical output behavior for FETs. The output current in the saturation regime, at a drain voltage, V_d, equal to - 60 V, is 3.7x larger for **P1S** compared to **P1**. However, in order to more quantitate the differences between **P1** and **P1S**, the transfer characteristics of the FET were compared.

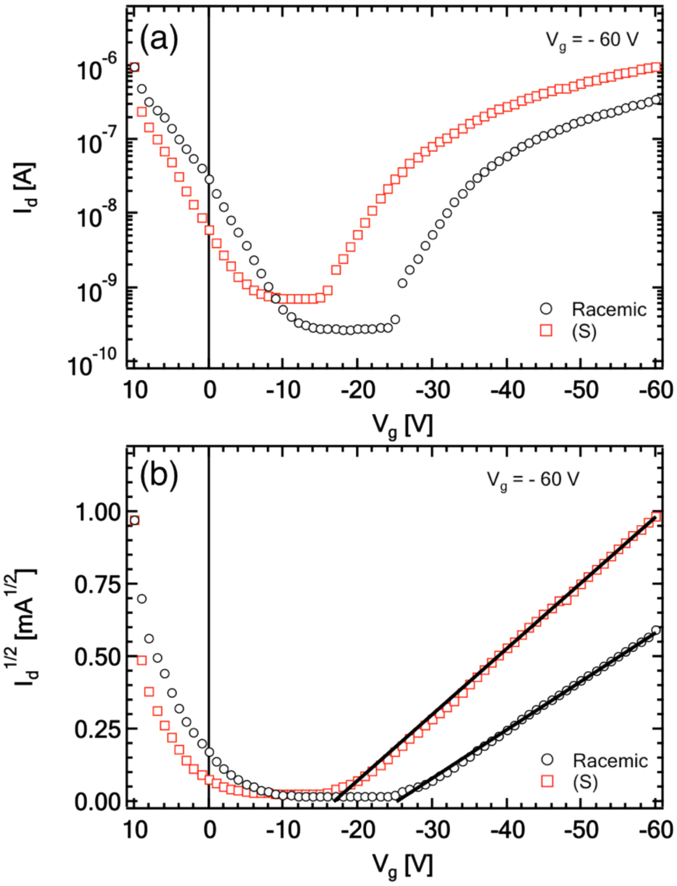

Figure 6.7 The transfer characteristics of P1 (black circles) and P1S (red squares) devices. Panel (a) is shown to demonstrate differences in I_{on}/I_{off} ratio. Panel (b) plots $I_d^{½}$ and the solid lines are fits to Equation (1) to determine μ_h and V_t. The channel width and length are 2 mm and 70 µm, respectively.

Using the transfer characteristics in the saturation regime (Figure 6.7) the field-effect mobility (μ_h), threshold voltage (V_t) and I_{on}/I_{off} ratio is extracted. This is achieved using Equation (1):[21]

$$\mu_{sat}(V_g) = \frac{2L}{WC_i}\left(\frac{\partial\sqrt{I_d}}{\partial V_g}\right)^2 \tag{1}$$

where I_d is the drain-source current in the saturation regime, V_g is the gate voltage, L is the channel length, W is the channel width, and C_i is the capacitance of the dielectric. The V_t for the devices were extracted from the x-intercept of the fitting line.

The parameters extracted from the transfer curves appear in Table 6.1. In the saturation regime, **P1S** has a μ_h of 2.1 × 10^{-3} cm^2/Vs whereas the μ_h of **P1** is 1.1 × 10^{-3} cm^2/Vs. To compare with the C16 or C12 straight chain analogues, the field effect mobility is 1-2 orders of magnitude lower. In addition, the V_t of **P1** is -25 V, compared to the reduced V_t for **P1S** of -17 V. The I_{on}/I_{off} ratio for both systems are more or less the same, at 10^3. The differences between **P1** and **P1S** are minor, however, these observations in the bulk electrical properties seem to correlate with the significant changes in the solid-state surface topologies shown in the previous section.

Table 6.1 Parameters extracted from field-effect transistors using P1 and P1S as the active layer. The data was extracted using the transfer characteristics in Figure 6.7.

Polymer	μ_h [cm^2/vs]	V_t [V]	I_{on}/I_{off}
P1	1.1 × 10^{-3}	-25	10^3
P1S	2.1 × 10^{-3}	-17	10^3

6.5 Conclusions

In conclusion, incorporation of a chiral side chain in an otherwise racemic material led to enhancements in the observed field-effect mobility when processing the racemic and enantiopure in parallel methods. The solution-state absorption properties of **P1** and **P1S** are significantly different, with **P1S** showing stronger aggregation behavior in poor or non-solvent solutions. These differences were transferred to the solid-state where fiber-like structures were observed on the film surface for **P1S**, whereas the **P1** film showed no signs of molecular ordering. Later, field-effect transistor devices showed a marginal difference of about a factor 2 in the measured μh from saturation regime transfer characteristics. This discovery gives researchers an additional handle, if needed, on further increasing the regularity in their molecular design. Unfortunately, the observed μ_h of **P1** and **P1S** are lower than the C16 or C12 straight-chain analogues. However, the 2-ethylhexyl side-chains afford better processability in the high molecular weight regime, where further control of regularity down to the chemical structure may be more useful.

Future work on this topic may draw attention to other solubilizing chains bearing chiral centers, such as (S)-3,7-dimethyloctyl. These chains are already commercially available from alcohol precursors, making structures more accessible. The longer chiral and branched alkyl chain may afford transistor performances more similar to the C12 or C16 straight-chain copolymers previously reported. Enantiopure structures may also be useful for visible-gap materials, where preferential absorption or photoluminescence of polarized light may be useful. Examples would be polymer light-emitting diodes or photodetectors.

6.6 Experimental Methods

General Details: All chemicals and metals were obtained from Acros Organics and used as received. Polymers were obtained from the group of Professor Guillermo C. Bazan (UCSB). Experimental details for the synthesis of **P1** and **P1S** appear in reference 13.

Optical Characterization: The absorption spectra were measured using a Perkin-Elmer Lambda 750 UV-vis spectrophotometer. Circular dichroism spectra were obtained using an AVIV model 202 CD-spectrometer (AVIV, Inc., Professor Kevin Plaxco group, UCSB). All optical characterization was performed using quartz cuvettes.

Atomic Force Microscopy: All atomic force microscopy images were measured under inert atmosphere of nitrogen. Images were obtained using a MultiMode AFM (Veeco). Silicon probes with a spring constant of ~5 N/m and resonant frequencies of 75 kHz (Budget Sensors) were used for tapping mode measurements.

Field-Effect Transistor Fabrication and Testing: FETs were made using a bottom-gate, top contact architecture. The gate electrode was n^{++} doped Si with 150 nm thick

SiO_2 serving as the gate dielectric (WRS Materials). The SiO_2 dielectric was passivated by treatment with octyltrichlorosilane (OTS). This passivation layer minimizes trapping at the polymer-dielectric interface changes the surface energy, instilling a more hydrophobic character at the polymer-dielectric interface. The OTS treatment procedure appears below in its own subsection. For film processing, 0.25% w/v solutions of **P1** or **P1S** were prepared in chlorobenzene (CB) solution and the necessary v:v ratio of the desired solvent additive was added. These solutions were kept at 80 °C prior to use. All solutions were spin cast onto the OTS treated SiO_2 substrates at 2000 rpm for 60 seconds. After spin coating, all films were annealed at 80 °C for 10 minutes. 60 nm thick Au source-drain electrodes were subsequently thermally deposited atop the polymer films. The source-drain electrodes were either 1 mm or 2 mm wide and the channel length was 70 μm. The electrical characteristics were measured using a Keithley 4200 Semiconductor Characterization System in a vacuum probe station (Lakeshore Cryotonics).

6.7 References

(1) Nam, S.; Lee, S.; Lee, I.; Shin, M.; Kim, H.; Kim, Y. *Nanoscale* **2011**, *3*, 4261.

(2) Yamaguchi, S.; Swager, T. M. *J. Am. Chem. Soc.* **2001**, *123*, 12087–12088.

(3) McCullough, R. D.; Lowe, R. D. *J. Chem. Soc. Chem. Commun.* **1992**, 70.

(4) Chen, T. A.; O'Brien, R. A.; Rieke, R. D. *Macromolecules* **1993**, *26*, 3462–3463.

(5) Ying, L.; Hsu, B. B. Y.; Zhan, H.; Welch, G. C.; Zalar, P.; Perez, L. A.; Kramer, E. J.; Nguyen, T.-Q.; Heeger, A. J.; Wong, W.-Y.; Bazan, G. C. *J. Am. Chem. Soc.* **2011**, *133*, 18538–18541.

(6) Tseng, H.-R.; Phan, H.; Luo, C.; Wang, M.; Perez, L. A.; Patel, S. N.; Ying, L.; Kramer, E. J.; Nguyen, T.-Q.; Bazan, G. C.; Heeger, A. J. *Adv. Mater.* **2014**, *26*, 2993-2998.

(7) Grimsdale, A. C.; Chan, K. L.; Martin, R. E.; Jokisz, P. G.; Holmes, A. B. *Chem. Rev.* **2009**, *109*, 897–1091.

(8) Abbel, R.; Schenning, A. P. H. J.; Meijer, E. W. *J. Polym. Sci. Part Polym. Chem.* **2009**, *47*, 4215–4233.

(9) Geng, Y.; Trajkovska, A.; Katsis, D.; Ou, J. J.; Culligan, S. W.; Chen, S. H. *J. Am. Chem. Soc.* **2002**, *124*, 8337–8347.

(10) Gilot, J.; Abbel, R.; Lakhwani, G.; Meijer, E. W.; Schenning, A. P. H. J.; Meskers, S. C. J. *Adv. Mater.* **2010**, *22*, E131–E134.

(11) Oda, M.; Nothofer, H.-G.; Scherf, U.; Šunjić, V.; Richter, D.; Regenstein, W.; Neher, D. *Macromolecules* **2002**, *35*, 6792–6798.

(12) Peeters, E.; Christiaans, M. P. T.; Janssen, R. A. J.; Schoo, H. F. M.; Dekkers, H. P. J. M.; Meijer, E. W. *J. Am. Chem. Soc.* **1997**, *119*, 9909–9910.

(13) Bazan, G. C.; Ying, L.; Zalar, P.; Nguyen, T. Q. Conjugated copolymers chiral side chain for organic thin film transistors, **2013**.

(14) Langeveld-Voss, B. M. W.; Janssen, R. A. J.; Meijer, E. W. *J. Mol. Struct.* **2000**, *521*, 285–301.

(15) Halkyard, C. E.; Rampey, M. E.; Kloppenburg, L.; Studer-Martinez, S. L.; Bunz, U. H. F. *Macromolecules* **1998**, *31*, 8655–8659.

(16) Tomović, Ž.; van Dongen, J.; George, S. J.; Xu, H.; Pisula, W.; Leclère, P.; Smulders, M. M. J.; De Feyter, S.; Meijer, E. W.; Schenning, A. P. H. J. *J. Am. Chem. Soc.* **2007**, *129*, 16190–16196.

(17) Schenning, A. P. H. J.; Kilbinger, A. F. M.; Biscarini, F.; Cavallini, M.; Cooper, H. J.; Derrick, P. J.; Feast, W. J.; Lazzaroni, R.; Leclère, P.; McDonell, L. A.; Meijer, E. W.; Meskers, S. C. J. *J. Am. Chem. Soc.* **2002**, *124*, 1269–1275.

(18) Jimison, L. H.; Toney, M. F.; McCulloch, I.; Heeney, M.; Salleo, A. *Adv. Mater.* **2009**, *21*, 1568–1572.

(19) Schoonbeek, F. S.; van Esch, J. H.; Wegewijs, B.; Rep, D. B. A.; de Haas, M. P.; Klapwijk, T. M.; Kellogg, R. M.; Feringa, B. L. *Angew. Chem. Int. Ed.* **1999**, *38*, 1393–1397.

(20) Dimitrakopoulos, C. D.; Malenfant, P. R. L. *Adv. Mater.* **2002**, *14*, 99–117.

(21) Sze, S. M. *Physics of semiconductor devices*; 3rd ed.; Wiley-Interscience: Hoboken, N.J, 2007.

7.0 Using Lewis Acids to Modulate The Absorption, Photoluminescence, and Electroluminescence of Lewis Basic Polymers

In chapter 7, Lewis acid-base interactions are exploited to tune the absorption, photoluminescence, and electroluminescence of a π-conjugated copolymer. The π-conjugated polymer, poly[(9,9-dioctylfluorene-2,7-diyl)-*alt*-(pyridine-2,6-diyl)] (**F8Py**), was synthesized to provide a Lewis basic site for binding of Lewis acids. In this work, attention was paid on adducts between **F8Py** and tris(pentafluorophenyl)boron (**BCF**). It is shown that the absorption of **F8Py** can be red shifted up to 30 nm. Interestingly, formation of the **F8Py-BCF** adduct does not result in quenching of photoluminescence, but an overall red shift and increase in quantum yield. These changes in optical properties extend to the electrical behavior, where films containing various amounts of **F8Py-BCF** adduct results in red shifted electroluminescence. This project demonstrates the utility and viability of Lewis acid-base chemistry for *functional* devices utilizing such π-conjugated systems.

7.1 Introduction

In chapter 1, it was shown that various synthetic strategies could be used in order to fine-tune the energetic positions of the highest occupied and lowest unoccupied molecular orbitals (HOMO and LUMO).[1–4] These structural modifications at the molecular level tailors a given π-conjugated system for a given application –

wider (visible) gaps for polymer light-emitting diodes (PLEDs)[5–7], narrow gaps for photovoltaics and photodetectors[8–10], and either wide or narrow gaps for unipolar or ambipolar conduction in field-effect transistors.[11]

Several band-gap engineering strategies already exist for tuning the optoelectronic properties of π-conjugated polymers. These include: (1) choice of repeat unit, (2) stabilizing quinoidal resonance structures, (3) planarization or kinking of repeat units, (4) incorporation of main group elements, (5) cross-conjugation, (6) donor-acceptor repeat units, or (7) statistical copolymers.[5,12–14] The properties of a bulk film can also be tuned by utilizing polymer:polymer, polymer:molecule, or polymer:phosphor blends.[15–18]

Previously, it was shown that addition of protic acids to π-conjugated molecules containing basic functionalities could also be used to achieve band-gap modulation in solution and in the bulk. Protonation of heteroatoms along a conjugated backbone resulted in redistribution of electron densities and thus changes in the effective band-gap.[19–22] More recently, it was shown that Lewis acids could be used to influence the degree of charge transfer character and therefore the absorption properties of narrow band gap polymers and oligomers.[23–25] This strategy is attractive because it allows for careful control of optical properties through modulation of Lewis acid strength. For example, trimethylaluminum would give a smaller red-shift when compared to boron trifluoride would give a larger red shift. In addition, since the resultant Lewis acid-base adducts are formally zwitterionic, one avoids the presence of free mobile ions in the polymer matrix as would be generated during a protonation reaction.[26,27] Mobile ions could have detrimental or unpredictable influences on the electrical properties of such films.

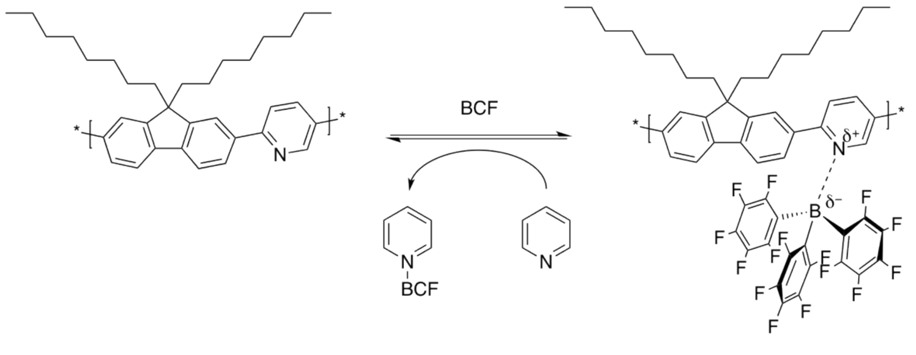

Figure 7.1 Reversible adduct formation between F8Py and BCF in solution. The parent polymer can be recovered by treatment with pyridine.

In the following, it is shown that use of Lewis acid-base interactions is a facile method to tune the absorption, photoluminescence, and electroluminescence properties of poly[(9,9-dioctylfluorene-2,7-diyl)-*alt*-(pyridine-2,6-diyl)] (**F8Py**). This polymer was selected for this study since fluorene-type polymers typically exhibit relatively high photoluminescence (PL) quantum yields in the visible spectrum and have been widely used in PLED research. The octyl side chains were chosen to improve solubility of the polymer. The pyridine co-monomer unit provides a lone pair of electrons that can readily bind to Lewis acids. Trivalent group 13 compounds work well in this respect due to their vacant p_z orbital that can readily accept a pair of electrons, as would be the case for the classical reaction of a boron trihalide with ammonia. In this work, we focus on trispentafluorophenyl borane (**BCF**) due to its strong Lewis acidity, resistance to air and moisture, and stability towards B-C cleavage.[28,29]

A general scheme for reactions between **F8Py** and **BCF** is shown in Figure 7.1 below.

As will be shown below, the **F8Py-BCF** adducts leads to lower energy absorption and emission transitions, extended PL lifetimes, and increased solid-state quantum yields. These favorable properties allowed this strategy to be successfully demonstrated in PLED devices to modify the electroluminescence (EL) characteristics while maintaining the luminance efficiency of the parent polymer.

7.2 Optical Properties

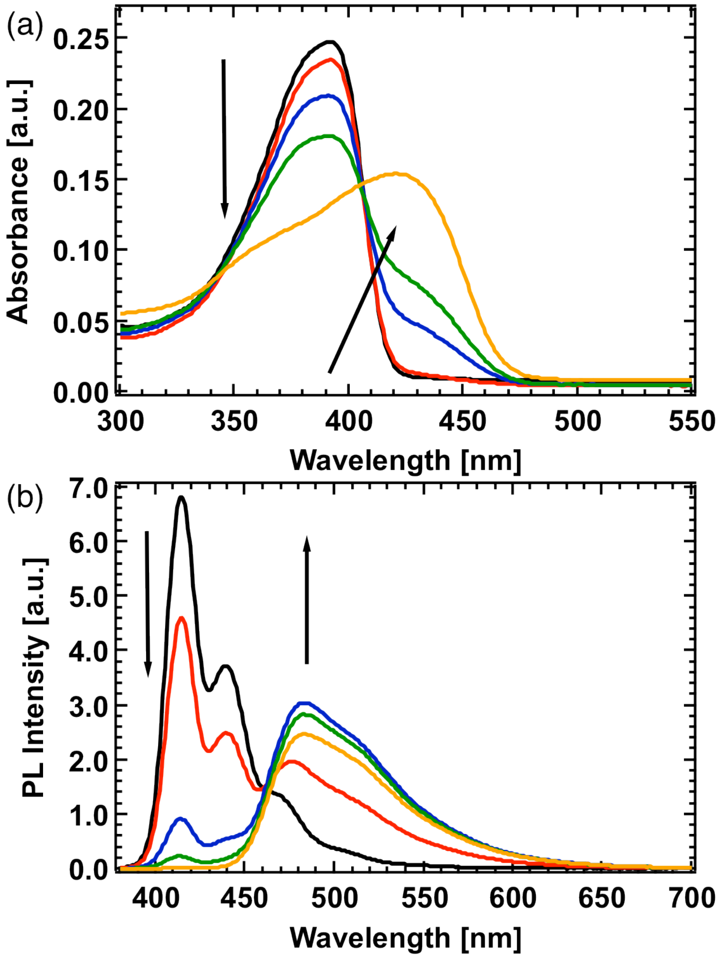

Figure 7.2 UV-Vis absorption (a) and PL (b) spectra of F8Py in toluene after addition of 0.0 (black line), 0.1 (red line), 0.3 (blue line), 0.7 (green line), and 1.3 (orange line) mol. equivalents of BCF. The arrows serve as a guide of the overall trend. See Figure 7.12 in the appendix of this chapter for a complete set of spectra.

The absorption and photoluminescence (PL) properties of various molar ratios of **F8Py** and **BCF** were used to examine **F8Py**-**BCF** adduct formation. The UV-vis and PL spectra in dilute toluene solution at where **F8Py** is dissolved at a concentration of 5 × 10^{-6} M (in terms of repeat unit mass, 2 × 10^{-3} mg/mL) are shown in Figure 7.2. Pristine **F8Py** has a broad absorption spectrum, with an absorption maximum (λ_{max}) of 392 nm and an absorption onset (λ_{onset}) of 417 nm, which is in close agreement with previous reports on structurally related polymers.[30,31] Incremental additions of 0.1 equivalents of **BCF** gives rise to a reduction of the peak at 391 nm and the growth of a new, broad peak with a $\lambda_{max\ of}$ 421 nm and λ_{onset} of 471 nm (Figure 7.1a). For clarity, only 0.0, 0.3, 0.7, and 1.3 equivalents additions of **BCF** are shown in Figure 7.1. The complete spectra for incremental additions of 0.1 up to 1.4 equivalents **BCF** is shown in Figure 7.12, in the appendix. The newly red-shifted λ_{onset} can be thought in terms of an effectively reduced optical band-gap. The change in spectral properties is attributed to adduct formation between the N-atom in **F8Py** and **BCF**, as was shown in Figure 7.1.

Just as was reported previously, **BCF** effectively withdraws electron density from the pyridine moiety in the copolymer leading to a lower energy charge-transfer band. Addition of pyridine regenerates the spectra of pristine **F8Py** due to the formation of the pyridine-**BCF** adduct and liberation of the parent polymer (**F8Py**), demonstrating that the binding is reversible, in agreement with previous publications.[23,24,32] The apparent isosbestic point at ~ 406 nm suggests that *only* two separate species exist in solution, corresponding to **BCF** bound and unbound **F8Py** monomer units.

Figure 7.2b shows the PL spectra in toluene solution after addition of **BCF** to **F8Py**, measured using the solutions that appear in Figure 7.2a. Again, for clarity only 0.0, 0.3, 0.7, and 1.3 equivalents additions of **BCF** are shown in Figure 7.2b. The complete spectra for incremental additions of 0.1 up to 1.4 equivalents **BCF** is shown in Figure 7.12, in the appendix. All PL measurements were measured using a fluorometer with an excitation wavelength of 390 nm. The PL spectrum of pristine **F8Py** contains vibronic fine structure, possessing three distinct peaks at 414 nm, 439 nm, and 469 nm – a common feature of polyfluorene type polymers.[33–35] Stepwise addition of **BCF** leads to a red shift in emission and reduction of vibronic fine structure, resulting in a very broad emission band spanning from 450 to 600 nm with λ_{max} = 484 nm. Similar broadening and loss of vibronic features was also reported upon protonation of similar polymer structures. The quantum yields of these solutions were measured using the relative method, with quinine sulphate as the standard (0.5 M H_2SO_4, quantum yield = 0.546). The quantum yields in solution are quite stable across all additions of **BCF** and were between 0.69 – 0.71.

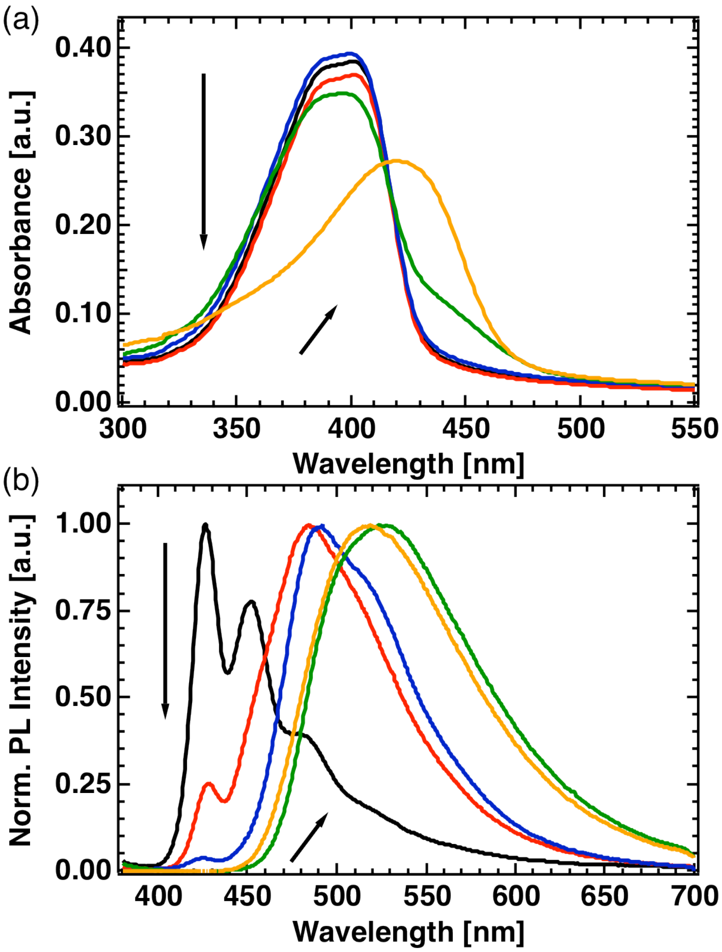

Figure 7.3 UV-Vis absorption (a) and PL (b) spectra of of F8Py and BCF adduct films containing 0.00 (black line), 0.001 (red line), 0.01 (blue line), 0.10 (green line), and 0.70 (orange line) mol. equivalents BCF. The films were spin cast from toluene solutions and the thicknesses are all ≈ 90 nm.

The absorption and PL spectra for thin-films of **F8Py-BCF** films are shown in Figure 7.3. All films were cast from toluene solution to give ≈ 90 nm thick films. The absorption of the native **F8Py** polymer is red shifted by 14 nm relative to in solution, giving a λ_{max} of 395 nm (Figure 7.3a). Successive additions of **BCF** leads to a red-shift of λ_{max} from 395 nm to a peak centered at roughly 422 nm. When compared to the spectra in solution, one observes that significant shifts are observed at lower **BCF** concentrations in the film than in the solution. These differences are attributed to a shift in the equilibrium towards adduct formation upon transitioning to the solid state.

The solid state PL spectrum of native **F8Py** contains vibronic fine structure with three distinct peaks at 424 nm, 450 nm and 477 nm (Figure 7.3b). This feature characteristic of polyfluorene type polymers and was also observed in the solution spectra.[13,33–37] Formation of **F8Py-BCF** adducts induces a shift in the PL peak from 424 nm to 532 nm resulting in a broad band spanning from 450 to 700 nm. In contrast to the solution measurements, the film PL ceases to significantly evolve beyond the addition of 0.1 mol. equivalents of **BCF**. These observations are consistent with interchain Förster resonance energy transfer (FRET) from free **F8Py** segments to **F8Py-BCF** adduct sites present in the film.

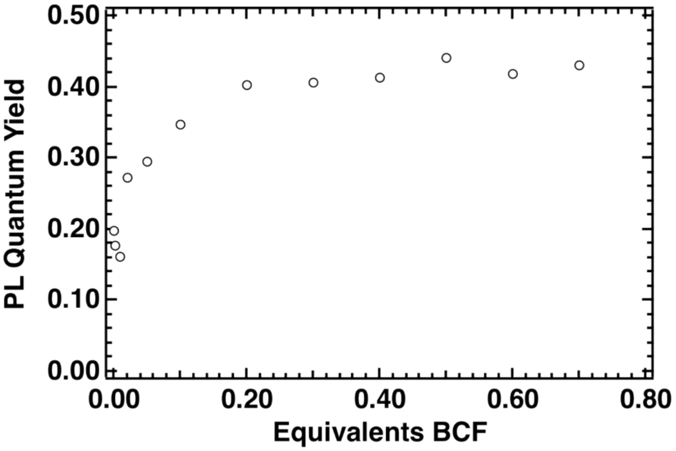

Figure 7.4 The PL quantum yield of F8Py films as a function of the number of mol. equivalents of BCF added.

The quantum yields of **F8Py-BCF** films were also analyzed in an integrating sphere using the method described in reference 38. Figure 7.4 shows the evolution of the PL quantum yield for various additions of **BCF** in the film. The PL quantum yields of adduct films increases from 0.20 for the parent polymer to 0.44 with 0.5 mol. equivalents **BCF**. Further additions do not seem to change the quantum yield further. This increase is most likely due to less effective self-quenching due a combination of deplanarization of the polymer chain upon binding of **BCF** and the greater separation between choromophores as a result of the additional steric bulk in the backbone induced by the formation of the adduct (Figure 7.1).

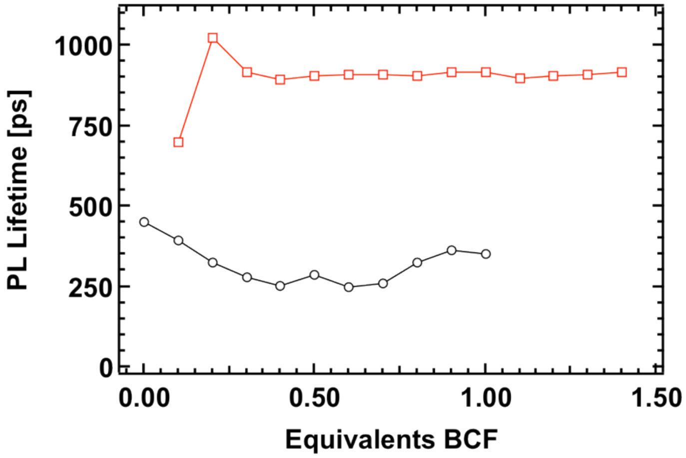

Figure 7.5 The PL lifetimes in solution as a function of mol. equivalents BCF. The black curves and circles correspond to the emission at 440 nm and the red curves and squares correspond to the emission at 480 nm. The excitation wavelength in both cases is 390 nm.

The PL lifetimes of **F8Py** and **F8Py-BCF** adducts were investigated using time correlated single-photon counting techniques to probe how adduct formation changes the excited state dynamics of the conjugated polymer. Typical decay traces in solution and fitting parameters for all measured decays in solutions appears in the appendix, Figure 7.14 and Table 7.3. In the pristine **F8Py** solution, the emission at 440 nm is well described by a monoexponential decay with a lifetime of 444 ps. Upon addition of **BCF**, the lifetime of the emission at 440 nm decays biexponentially with time constants of ~ 450 ps and ~ 50-70 ps, with the fast component contributing to up to 50% of the decay as more **BCF** is added to the solution. The 50-70 ps component matches the width of our instrument response function, so the actual lifetimes may be shorter than the measured value. The emission at 480 nm, however, has a longer-lived monoexponential decay with a time constant of ~ 1.10 ns across all **BCF** additions. A summary of the solution decays as a function of **BCF** additions shown in Figure 7.5.

A similar trend is observed in thin films, where the lifetime at 440 nm for pristine **F8Py** is short lived, at approximately 70 ps, while the PL decay of adduct films have multiexponential decays dominated by a time constant of ~ 2.1 ns. See the appendix, Figure 7.15 and Table 7.4 for representative PL decays and fitting parameters for all equivalents studied. The longer lifetime of the **F8Py-BCF** adducts can be explained by considering the formation of a new emissive state that is associated with the withdrawal of electron density from the polymer by **BCF** that has a lower oscillator strength.[39–41] A longer lifetime and higher PL quantum yield should bode well in PLEDs where these properties are crucial determinates of efficiency.

7.3 Surface Topology

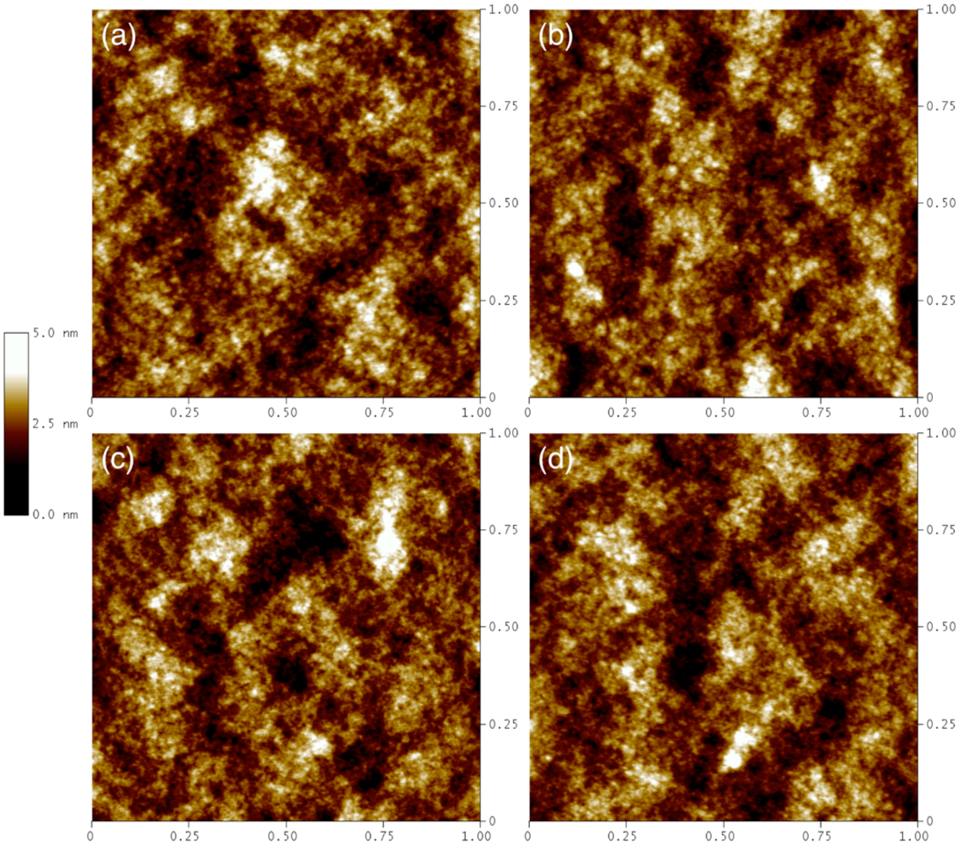

Figure 7.6 Surface Topology of films of pristine F8Py (a) and (b) 0.1, (c) 0.2, and (d) 0.3 mol. equivalents BCF. The scan size is 1 × 1 μm. Addition of BCF does not cause major changes in the surface topologies for this class of polymer.

The surface topology of **F8Py** and a films cast from solutions of **F8Py** containing 0.1, 0.2, and 0.3 mol. equivalents **BCF** were examined by using tapping-mode atomic force microscopy (AFM, Figure 7.6) All films are smooth and lack any evidence of local order. This is a common feature of polyfluorenes that usually exhibit smooth and amorphous films. The root mean square (RMS) surface roughness values are nearly identical at 0.56 nm for pristine **F8Py** and 0.54, 0.55, and 0.55 for the films containing 0.1, 0.2, and 0.3 equivalents **BCF**, respectively

7.4 Ultraviolet Photoelectron Spectroscopy

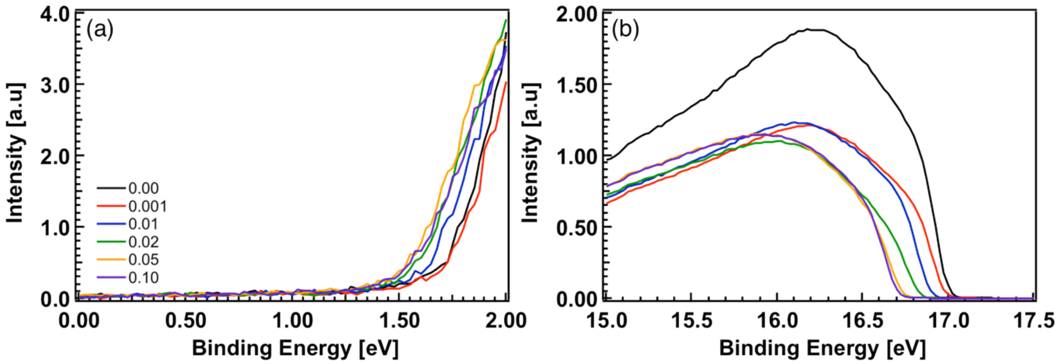

Figure 7.7 UPS spectra showing the low-energy cut-off region (a) and high-energy cut-off region (b) for F8Py-BCF films. The black curve corresponds to pristine F8Py. The red, blue, green, orange, and purple curves correspond to 0.001, 0.01, 0.02, 0.05, and 0.10 equivalents of BCF, respectively. The extracted values for the HOMO level of the polymer with different additions of BCF are shown in Table 7.1.

Ultraviolet photoelectron spectroscopy (UPS) was used to determine the highest occupied molecular orbital (HOMO) energy levels of the **F8Py** and **F8Py-BCF** adduct films.[42] These results are summarized in Table 7.1, with corresponding UPS spectra appearing in Figure 7.7. The LUMO was estimated from the optical band gap

(E_g). The E_g was estimated from the lowest energy peak in the fluorescence spectrum. The HOMO energies were determined by subtracting the difference between the high-energy cut-off and the low-energy cut-off regions (HOMO) in the spectra from the incident photon energy of 21.2 eV. Upon addition of **BCF**, the HOMO level is stabilized.[23–25] However, the lowest unoccupied molecular orbital (LUMO) level is reduced to a greater extent, resulting in the decreased E_g.

Table 7.1 The energy levels of F8Py and F8Py-BCF films. The HOMO level was determined by UPS, the Eg was estimated from fluorescence spectra, and the LUMO was calculated by the difference between the HOMO and optical gap.

mol. equiv. **BCF**	HOMO [eV]	E_g [eV]	LUMO [eV]
0.0	-5.74	2.91	-2.83
0.001	-5.80	2.56	-3.24
0.01	-5.86	2.52	-3.34
0.02	-5.92	2.51	-3.41
0.05	-5.96	2.46	-3.50
0.10	-5.98	2.36	-3.62

7.5 Polymer Light-Emitting Diodes

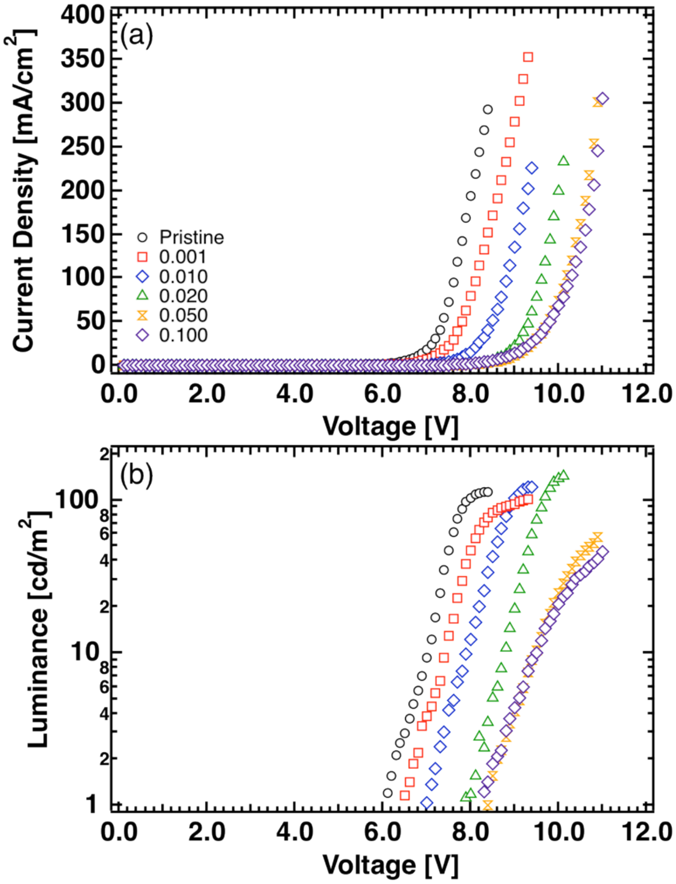

Figure 7.8 (a) Current density-voltage (*J-V*) and (b) luminance-voltage (*L-V*) characteristics for devices containing 0.0 (black circles), 0.001 (red squares), 0.010 (blue diamonds), 0.020 (green triangles), 0.050 (orange hourglasses) and 0.100 (purple diamonds) mol. equivalents BCF.

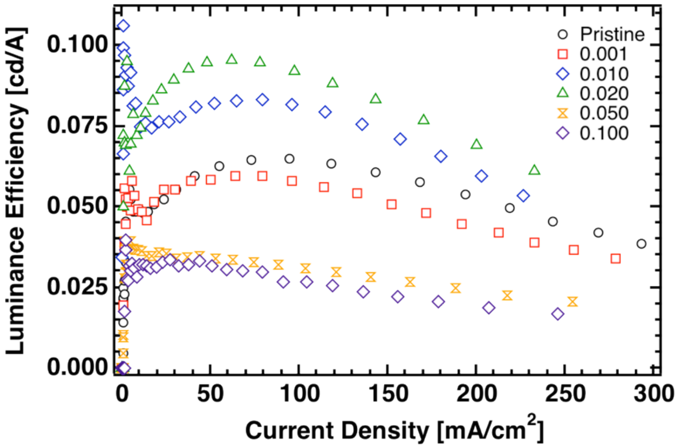

Figure 7.9 Luminance efficiency-current density (*LE-J*) characteristics for devices containing 0.0 (black circles), 0.001 (red squares), 0.010 (blue diamonds), 0.020 (green triangles), 0.050 (orange hourglasses) and 0.100 (purple diamonds) mol. equivalents BCF.

With these favorable optical and film forming properties, it seemed appropriate that **F8Py-BCF** adducts could function as the emissive layer in functional PLED devices. Test PLED structures consisted of indium-tin-oxide (ITO)/poly(3,4-ethylenedioxythiophene):poly(styrenesulfonate) (PEDOT:PSS)/poly(9-vinylcarbazole) (PVK)/**F8Py** + X mol. equivalents **BCF**/Ba/Al. The PVK layer was included as a hole injecting/electron blocking layer. Barium is a cathode whose work function (-2.5 eV) matches well with the LUMO of **F8Py** and **F8Py-BCF** adducts. Devices were fabricated in which 0.00, 0.01, 0.02, 0.05, and 0.10 mol. equivalents **BCF** were added. The resulting current density-voltage (*J-V*) and luminance-voltage (*L-V*) data are shown in Figure 7.8. The luminance efficiency-current density (*LE-J*) characteristics are shown in Figure 7.9.

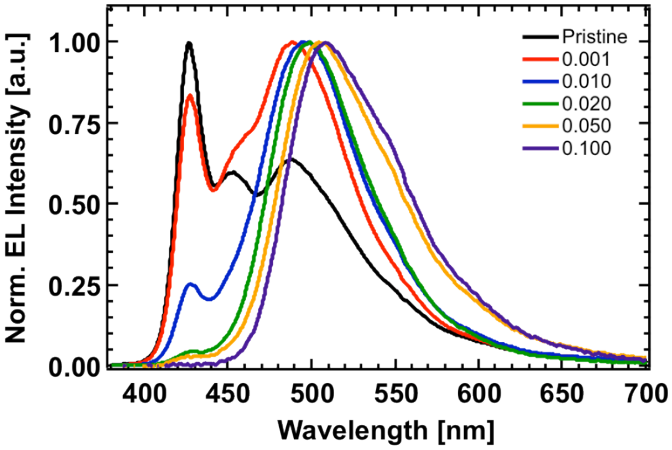

Figure 7.10 Electroluminescence spectra after addition of increasing equivalents of BCF: 0.0 (black line), 0.001 (red line), 0.010 (blue line), 0.020 (green line), 0.050 (orange line), and 0.100 (purple line). All spectra were measured at a constant current density of 111 mA/cm^2.

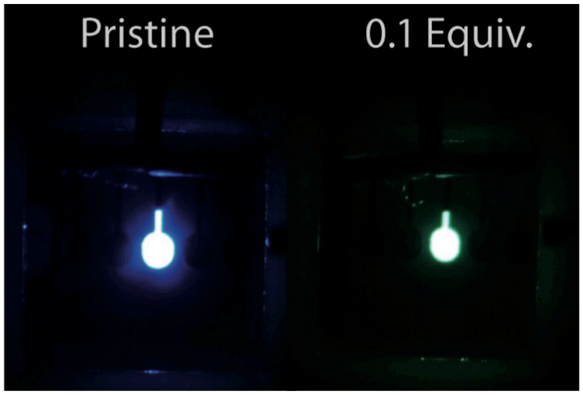

Figure 7.11 Photograph of pristine F8Py (left) and 0.10 equivalents BCF devices driven at a current density of 111 mA/cm^2.

The electroluminescence (EL) spectra (obtained at a current density of 111 mA/cm^2) of the devices are shown in Figure 7.10. A photograph is shown in Figure 7.11, demonstrating the change in color. A summary of all parameters extracted from the plots below appears at the end of this section; see Table 7.2.

As larger fractions of **BCF** are added, the *J-V* and *L-V* characteristics shift to higher biases, resulting in larger turn-on voltage (V_{on}) relative to the pristine **F8Py** device (Figure 7.8). The shift of the *J-V* and *L-V* characteristics towards higher biases could be due to a modification of injection barriers in the PLED devices – for example, as a result of the decreasing effective HOMO level (Table 7.1).[43,44] The sequential vacuum level shift observed in the UPS spectra is in agreement with the trends observed for V_{on} in the *J-V* and *L-V* plots. Since the HOMO of PVK is ~ - 5.4 eV[45] and assuming no interfacial effects, the hole-injection barrier in PLEDs fabricated can be increased from ~ 0.3 eV to ~ 0.6 eV.[46] Considering that the HOMO and LUMO energy levels are lowered in energy for the **F8Py**-**BCF** adducts, the barrier for hole-injection is increased while the electron-injection barrier (if using a low work function cathode, such as Ba) remains unchanged.

The *LE-J* characteristics of each device are similar, with all luminance efficiencies staying within same order of magnitude (Figure 7.9). Despite the increase in operating voltage, the external quantum efficiency (η_{ext}) remains constant at about 0.07% until the addition of more than 0.02 mol. equivalents **BCF** where a reduction in η_{ext} is observed. The η_{ext} were all compared at a current density of 11 mA/cm^2. More importantly, adduct formation at the concentrations studied does not adversely affect the luminance efficiency or quantum efficiency, while at the same time delivering modifications of the luminescent properties.

In the same manner as the PL spectra, increasing amounts of **BCF** gradually red shift the EL spectra (Figure 7.10). With increasing mol. equivalents of **BCF** gradual 'quenching' of the main **F8Py** emission takes place as the growth of the **F8Py-BCF** adduct peak proceeds. At 0.02 equivalents **BCF** the EL from the **F8Py** is weak, contributing less than 7% to the total EL. Since the M_n of the polymer sample is 25 kDa, this would correspond to approximately 1 **BCF** molecule per polymer chain. Additions of **BCF** beyond 0.02 mol. equivalents lead to slightly more red-shifted EL, up to a λ_{max} of 535 nm (Table 7.2). The Commission Internationale de L'éclairage 1931 (CIE 1931) color space coordinates were calculated from the EL spectra shown in Figure 7.10 and appear in Table 3.1. Photographs of actual pristine and 0.10 mol. equivalents devices are shown in Figure 7.11.

Table 7.2 Basic parameters of F8Py PLEDs containing various amounts of BCF.

mol. equiv. **BCF**	EL λ_{max} [nm]	CIE 1931 (x,y)	V_{on} [V]	LE [cd/A]	η_{ext} [%]
0.000	426	(0.19,0.19)	6.1	0.046	0.070
0.001	481	(0.18,0.22)	6.5	0.052	0.071
0.010	485	(0.20,0.34)	7.0	0.071	0.072
0.020	493	(0.20,0.43)	7.9	0.089	0.076
0.050	505	(0.27,0.49)	8.3	0.088	0.023
0.100	509	(0.29,0.54)	8.4	0.026	0.018

7.6 Conclusions

To conclude, simple mixing of a Lewis basic polymer with a Lewis acid allows the absorption and PL properties of the parent polymer to be modified in a single step. Upon adduct formation, the absorption and photoluminescence of **F8Py** could be red-shifted significantly. Interestingly, solutions and films containing **F8Py-BCF** adducts exhibit significantly longer excited state lifetimes and larger (or equal) quantum yields than the native **F8Py** polymer.

With these desirable optical properties, PLEDs were fabricated using **F8Py** and **F8Py-BCF** adducts as the emissive layer. Just like the PL spectra, the EL spectra are red-shifted as the fraction of polymer bound to **BCF** is increased. When 0.10 mol. equivalents of **BCF** is added, the emission of the pristine **F8Py** polymer at 426 nm is completely suppressed, resulting in an EL with a $\lambda_{\max}$ of 509 nm. The *LE-J* characteristics of devices were not significantly influenced by the formation of **F8Py-BCF** adducts, however, *J-V* and *L-V* characteristics were shifted to higher voltages. These shifts can be readily rationalized when considering a gradual increase in hole injection barriers as the effective HOMO level of the **F8Py** film is more and more decreased with the increasing presence of **F8Py-BCF** adducts. The use of alternative hole injection layers or inverted device structures may be able to circumvent this feature.

Lewis acid-base interactions provide a straightforward way to modulate optoelectronic properties in PLEDs without influence on device performance. Lewis acid-base interactions may also be useful in electrochemical sensors to detect Lewis acids or Lewis bases in an environment, such as ammonia. In addition, this strategy could be very important to other organic electronic applications where fine-tuning of energy levels and emissive gaps are crucial for device operation, such as in tandem photovoltaics or photodetectors and field-effect transistors. In the next chapter (Chapter 8), the influence of π-conjugated polymer-**BCF** adducts on the hole transport properties of a model system in order to gain further insight into the process that takes place in devices

7.7 Experimental Methods

Polymer Synthesis and BCF Preparation: **F8Py** was synthesized according to the previously reported procedure.[30,31] GPC analysis was performed in 1,3,5-trichlorobenzene at 150 °C to give M_n of 25800 and PDI of 2.9. **BCF** was purified by sublimation before use.

Optical Measurements: The absorption spectra were measured using a Perkin-Elmer Lambda 750 UV-Vis spectrophotometer. Solutions were prepared in nitrogen atmosphere and measured in capped 1 cm quartz cuvettes using anhydrous toluene (Acros Organics) as the solvent. Films were prepared by spin coating **F8Py** from toluene with the appropriate monomer mol. equivalents **BCF** onto clean quartz substrates. Steady-state PL spectra were obtained using a Horiba Fluorolog spectrofluorometer.

Fluorescence lifetime measurements were performed using the time-correlated single photon counting (TCSPC) technique. Approximately 200 femtosecond (fs) excitation pulses with a wavelength of 390 nm were generated by doubling the fundamental frequency of a fs Ti:Sapphire laser (Coherent Mira-900) pulses by optical harmonics generator (Inrad). The laser repetition rate was reduced to 2 MHz by a homemade acousto-optical pulse picker in order to avoid saturation of the chromophore. The TCSPC system was equipped with an ultrafast micro channel plate photomultiplier tube detector (Hamamatsu R3809U-51) and electronics board (Becker & Hickl SPC-630) and has instrument response time about 60-75 picoseconds. The triggering signal for the TCSPC board was generated by sending a small fraction of the laser beam onto a fast (400 MHz bandwidth) Si photodiode (Thorlabs Inc.). The fluorescence signal was dispersed in Acton Research SPC-500 monochromator after passing through a pump blocking, long wavelength-pass, autofluorescence-free, interference filter (Omega Filters, ALP series). The monochromator is equipped with a CCD camera (Roper Scientific PIXIS-400) allowing for monitoring of the time-averaged fluorescence spectrum.

Photoluminescence quantum yield (PLQY) measurements of polymer films were performed in spectralon-coated integrating sphere (Labsphere) using a modification of the technique reported in reference [38]. The optical layout of the setup is identical to the one used in reference [38]. A calibrated photodiode (Newport Corporation 818UV) was used as a detector. Band-pass (UG11 Schott glass) and long-pass interference filters (Omega Filters, Thorlabs) were used to detect laser and photoluminescence (PL) intensities, respectively. The cut-off wavelength of the long-pass filter was selected to be as close to the laser wavelength as possible but still allow for efficient blocking of the laser light. The excitation light with wavelength 364 nm was generated by Spectraphysics Beamlok 2060 lasers. The laser light intensity was attenuated to the level of <5 mW at the sample's position by neutral density filters. The laser beam was modulated by an optical chopper (SRS SR540) which also provided a clock signal for a lock-in amplifier (SRS SR830) which detected the photocurrent from the photodiode. The samples were deposited on fused silica substrates in inert atmosphere and the sphere was purged with dry nitrogen during the measurements to reduce the sample's photodegradation.

Atomic Force Microscopy: The AFM surface topology data was obtained in nitrogen atmosphere using a MultiMode AFM (Veeco) in tapping mode. Silicon probes (Budget Sensors) with a spring constant of ~ 5 N/m and resonant frequencies of 75 kHz were used.

Polymer Light-Emitting Diode Fabrication: PLEDs were fabricated on corning 1737 glass substrates patterned with 140 nm of ITO. The substrates were scrubbed thoroughly with detergent and sonicated in water (3x, 10 min), acetone (1x, 30 min), isopropanol (1x, 30 min), and treated with UV-ozone. A 50 nm thick layer of PEDOT:PSS (Baytron P 4083, H. C. Starck Inc.) is then deposited and baked at 140 °C. PVK (Sigma-Aldrich) was then spin coated from chlorobenzene atop the PEDOT:PSS to yield 20 nm thick films. The **F8Py** and **F8Py-BCF** were spun coat from toluene solutions giving ca. 90 nm thick films. The cathode consisted of Ba (5 nm) and an Al capping layer (100 nm) deposited by thermal evaporation (chamber pressure ca. 10^{-7} torr). PLEDs were tested in a nitrogen atmosphere using a Keithley 2602 sourcemeter coupled with a calibrated Si-photodiode. Electroluminescence spectra were obtained using an Ocean Optics USB2000 spectrophotometer in nitrogen atmosphere.

Ultraviolet Photoelectron Spectroscopy: For UPS measurements, 60 nm of Au was deposited atop precleaned Si/SiO_2 substrates. **F8Py** and **F8Py-BCF** solutions (0.2% w/v, toluene) were then deposited at 3000 rpm atop the Au film in nitrogen atmosphere. In order to minimize air-exposure, samples were then transferred to the analysis chamber using an air-free sample holder. The UPS analysis chamber is equipped with a hemispherical electron-energy analyzer (Kratos Ultra Spectrometer) and kept at a pressure of 1×10^{-9} torr.

7.8 Appendix

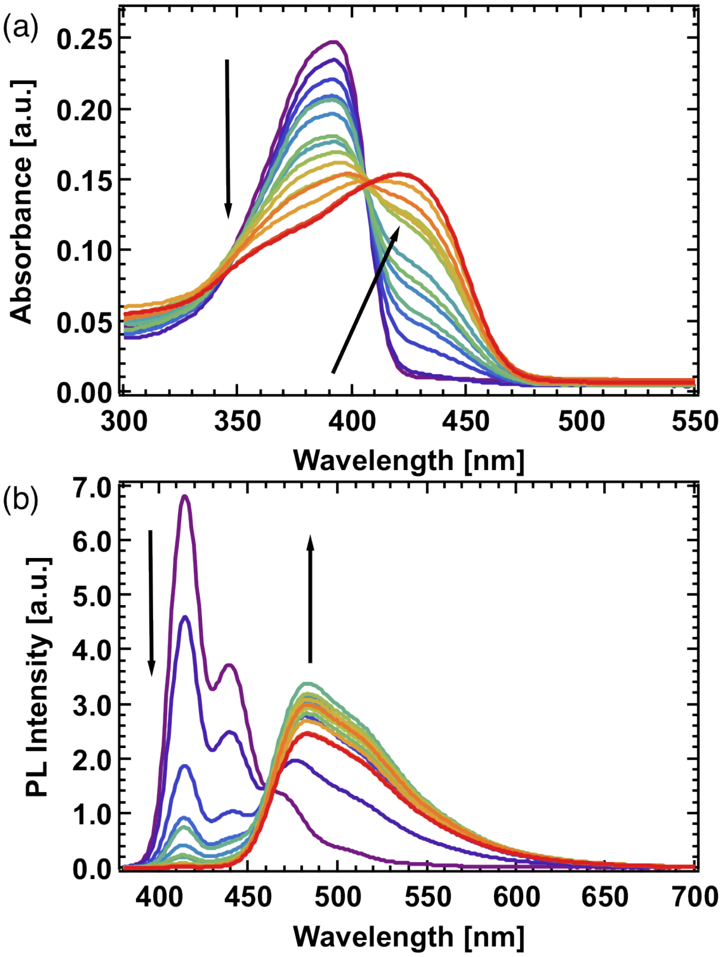

Figure 7.12 UV-Vis absorption (a) and photoluminescence (b) spectra of F8Py and BCF adducts in toluene. Each successive curve corresponds to a step of 0.1 additional mol. equivalents of BCF.

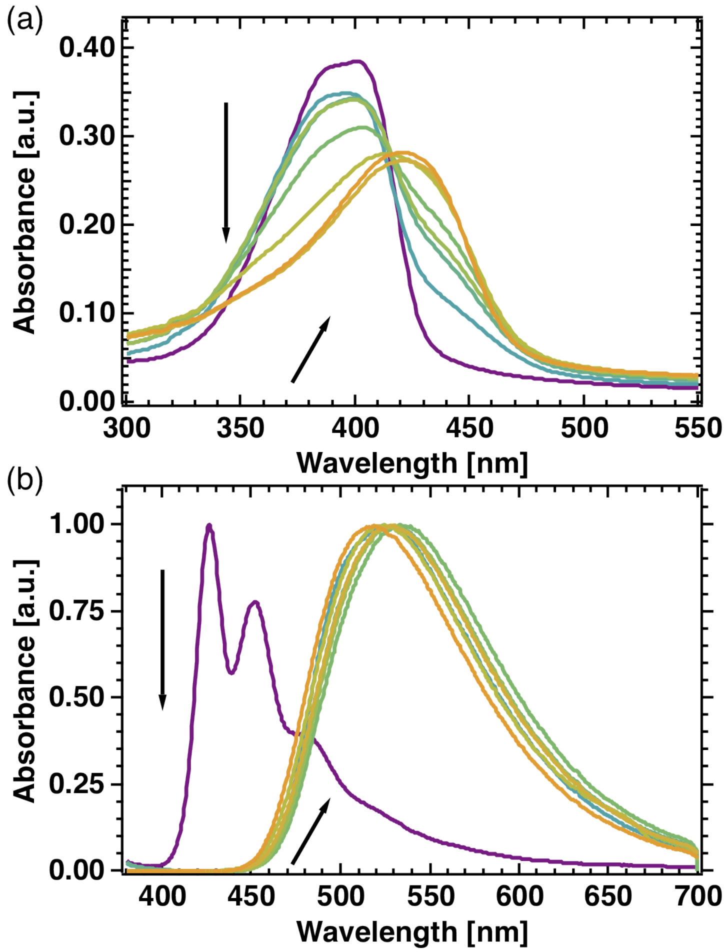

Figure 7.13 UV-Vis absorption (a) and photoluminescence (b) spectra of F8Py and BCF adducts in toluene. Each successive curve corresponds to a step of 0.1 additional mol. equivalents of BCF.

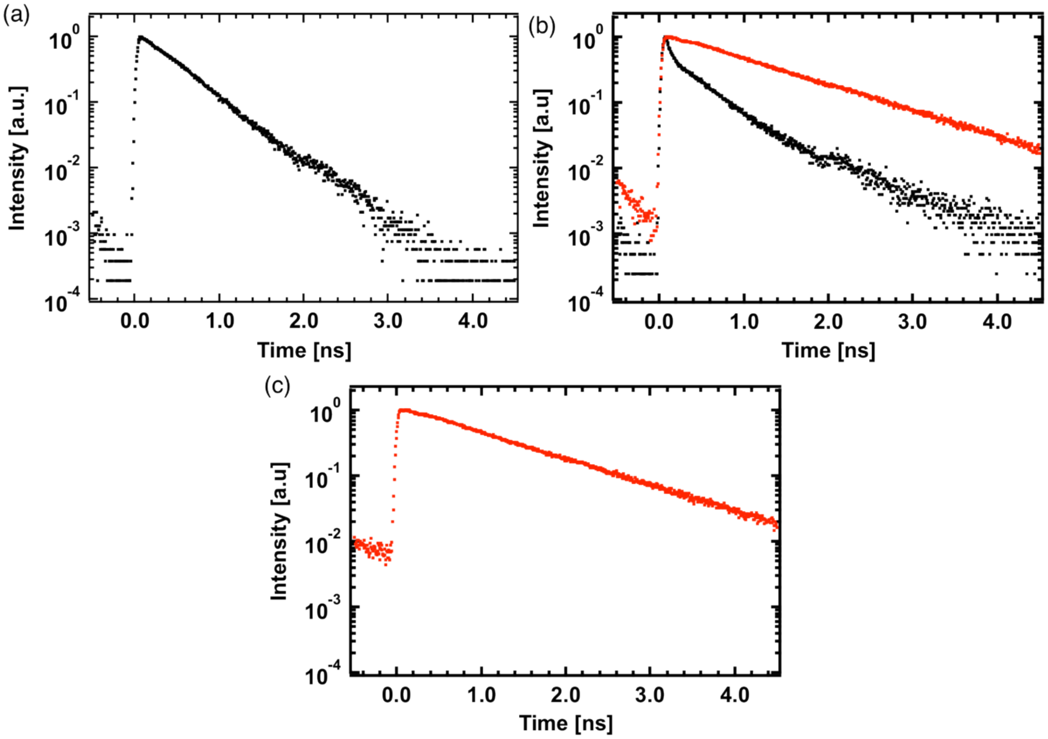

Figure 7.14 Normalized representative photoluminescence transients of F8Py solutions containing (a) 0.0, (b) 0.4, and (c) 1.0 mol. equivalents BCF. The black dots correspond to emission at 440 nm and the red dots correspond to emission at 480 nm. The excitation wavelength in all cases was 390 nm.

Table 7.3 Photoluminescence decay fitting parameters for solutions containing F8Py and BCF. Parameters A1 and A2 are weighing parameters and T1 and T2 are the complementary time constants for biexponential decay fittings.

mol. equiv. **BCF**	Emission at 440 nm				Emission at 480 nm			
	A1	T1 [ps]	A2	T2 [ps]	A1	T1 [ps]	A2	T2 [ps]
0.0	1.0	444	N/A	N/A	N/A	N/A	N/A	N/A
0.1	0.92	407	0.08	69	0.32	1036	0.69	562
0.2	0.69	403	0.34	73	1.0	1031	N/A	N/A
0.3	0.55	419	0.45	56	1.0	1088	N/A	N/A
0.4	0.50	461	0.50	52	1.0	1116	N/A	N/A
0.5	0.49	500	0.35	40	1.0	1092	N/A	N/A
0.6	0.54	428	0.51	51	1.0	1096	N/A	N/A
0.7	N/A	N/A	N/A	N/A	1.0	1096	N/A	N/A
0.8	N/A	N/A	N/A	N/A	1.0	1103	N/A	N/A
0.9	N/A	N/A	N/A	N/A	1.0	1088	N/A	N/A
1.0	N/A	N/A	N/A	N/A	1.0	1087	N/A	N/A
1.1	N/A	N/A	N/A	N/A	1.0	1110	N/A	N/A
1.2	N/A	N/A	N/A	N/A	1.0	1011	N/A	N/A
1.3	N/A	N/A	N/A	N/A	1.0	1097	N/A	N/A
1.4	N/A	N/A	N/A	N/A	1.0	1072	N/A	N/A

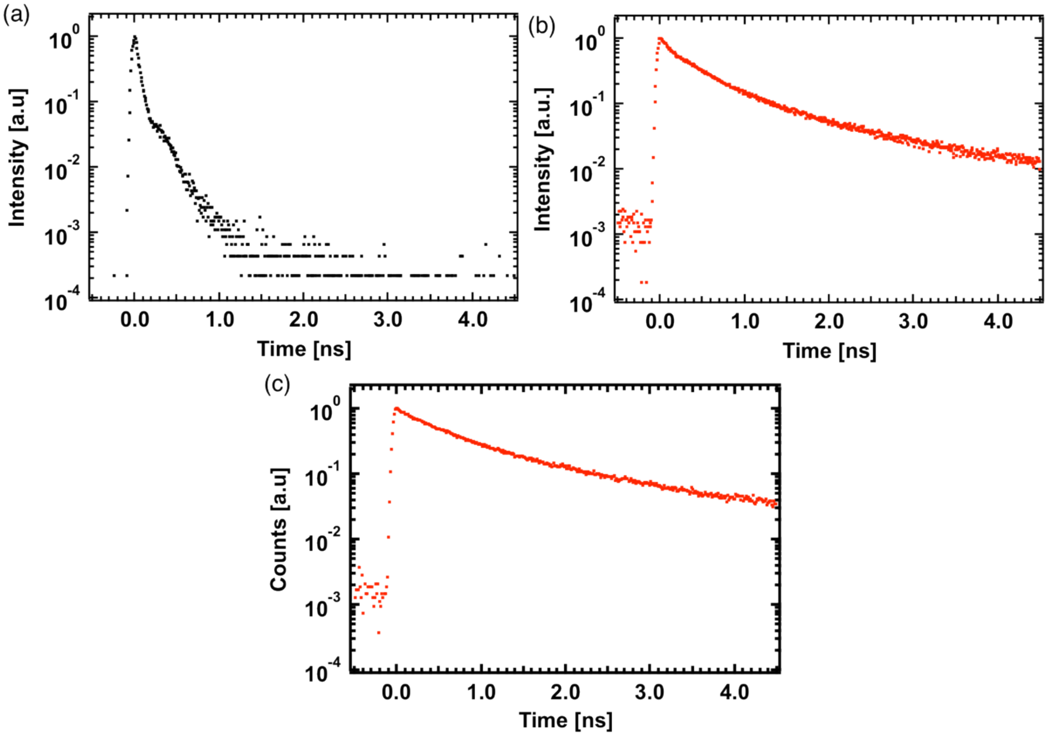

Figure 7.15 Normalized representative photoluminescence transients of F8Py films containing (a) 0.0, (b) 0.1, and (c) 0.6 mol. equivalents BCF. The black dots correspond to emission at 440 nm and the red dots correspond to emission at 510 nm. The excitation wavelength in all cases was 390 nm. Note that the emission of the pristine polymer at 440 nm (a) decays with a time constant that is shorter than the instrument response function width. The transient is a replica of the instrument response function.

Table 7.4 Photoluminescence decay fitting parameters for films containing F8Py and BCF. Parameters A1, A2, A3, are weighing parameters and T1, T2, T3 are the complementary time constants of triexponential decay fittings.

mol. equiv.	Emission at 440 nm				Emission at 510 nm					
BCF	A1	T1 [ps]	A2	T2 [ps]	A1	T1 [ps]	A2	T2 [ps]	A3	T3 [ps]
0.0	N/A	< 50	N/A	N/A	N/A	N/A	N/A	N/A	N/A	N/A
0.1	N/A	N/A	N/A	N/A	0.15	73	0.69	500	0.15	1817
0.2	N/A	N/A	N/A	N/A	0.32	73	0.64	452	0.14	1636
0.3	N/A	N/A	N/A	N/A	0.22	72	0.64	422	0.20	1479
0.4	N/A	N/A	N/A	N/A	0.04	29	0.76	662	0.22	2027
0.5	N/A	N/A	N/A	N/A	0.18	40	0.66	658	0.17	2245
0.6	N/A	N/A	N/A	N/A	0.07	72	0.71	591	0.23	2407

7.9 References

(1) Forrest, S. R.; Thompson, M. E. *Chem. Rev.* **2007**, *107*, 923–925.

(2) Klauk, H. *Organic electronics: materials, manufacturing and applications*; Wiley-VCH: Weinheim, 2006.

(3) Hadziioannou, G.; Malliaras, G. G. *Semiconducting polymers. Volume 1 Volume 1*; Wiley-VCH-Verlag: Weinheim, 2007.

(4) *Organic electronics: materials, processing, devices and applications*; So, F., Ed.; CRC Press: Boca Raton, FL, 2010.

(5) Grimsdale, A. C.; Chan, K. L.; Martin, R. E.; Jokisz, P. G.; Holmes, A. B. *Chem. Rev.* **2009**, *109*, 897–1091.

(6) Beaujuge, P. M.; Amb, C. M.; Reynolds, J. R. *Acc. Chem. Res.* **2010**, *43*, 1396–1407.

(7) Amb, C. M.; Dyer, A. L.; Reynolds, J. R. *Chem. Mater.* **2011**, *23*, 397–415.

(8) Boudreault, P.-L. T.; Najari, A.; Leclerc, M. *Chem. Mater.* **2011**, *23*, 456–469.

(9) Cheng, Y.-J.; Yang, S.-H.; Hsu, C.-S. *Chem. Rev.* **2009**, *109*, 5868–5923.

(10) Chen, J.; Cao, Y. *Acc. Chem. Res.* **2009**, *42*, 1709–1718.

(11) Murphy, A. R.; Frechet, J. M. J. *Chem. Rev.* **2007**, *107*, 1066–1096.

(12) Roncali, J. *Chem. Rev.* **1997**, *97*, 173–205.

(13) Scherf, U.; List, E. J. W. *Adv. Mater.* **2002**, *14*, 477–+.

(14) Kraft, A.; Grimsdale, A. C.; Holmes, A. B. *Angew. Chem.-Int. Ed.* **1998**, *37*, 402–428.

(15) Berggren, M.; Inganäs, O.; Gustafsson, G.; Rasmusson, J.; Andersson, M. R.; Hjertberg, T.; Wennerström, O. *Nature* **1994**, *372*, 444–446.

(16) Kawamura, Y.; Yanagida, S.; Forrest, S. R. *J. Appl. Phys.* **2002**, *92*, 87–93.

(17) Gong, X.; Robinson, M. R.; Ostrowski, J. C.; Moses, D.; Bazan, G. C.; Heeger, A. J. *Adv. Mater.* **2002**, *14*, 581–585.

(18) Granström, M.; Inganäs, O. *Appl. Phys. Lett.* **1996**, *68*, 147.

(19) Kappaun, S.; Horner, S.; Kelterer, A.-M.; Waich, K.; Grasse, F.; Graf, M.; Romaner, L.; Niedermair, F.; Muellen, K.; Grimsdale, A. C.; Saf, R.; List, E. J. W.; Zojer, E.; Slugovc, C. *Macromol. Chem. Phys.* **2008**, *209*, 2122–2134.

(20) Monkman, A. P.; Palsson, L. O.; Higgins, R. W. T.; Wang, C. S.; Bryce, M. R.; Batsanov, A. S.; Howard, J. A. K. *J. Am. Chem. Soc.* **2002**, *124*, 6049–6055.

(21) Hancock, J. M.; Jenekhe, S. A. *Macromolecules* **2008**, *41*, 6864–6867.

(22) Monkman, A. P.; Halim, M.; Samuel, I. D. W.; Horsburgh, L. E. *J. Chem. Phys.* **1998**, *109*, 10372–10378.

(23) Welch, G. C.; Coffin, R.; Peet, J.; Bazan, G. C. *J. Am. Chem. Soc.* **2009**, *131*, 10802–+.

(24) Welch, G. C.; Bazan, G. C. *J. Am. Chem. Soc.* **2011**, *133*, 4632–4644.

(25) Hayashi, S.; Asano, A.; Koizumi, T. *Polym. Chem.* **2011**, *2*, 2764–2766.

(26) Rep, D. B. A.; Morpurgo, A. F.; Sloof, W. G.; Klapwijk, T. M. *J. Appl. Phys.* **2003**, *93*, 2082–2090.

(27) De Mello, J. C.; Tessler, N.; Graham, S. C.; Friend, R. H. *Phys. Rev. B* **1998**, *57*, 12951–12963.

(28) Piers, W. E. In *Advances in Organometallic Chemistry, Vol 52*; West, R.; Hill, A. F., Eds.; 2005; Vol. 52, pp. 1–76.

(29) Piers, W. E.; Chivers, T. *Chem. Soc. Rev.* **1997**, *26*, 345–354.

(30) Liu, B.; Yu, W. L.; Lai, Y. H.; Huang, W. *Chem. Mater.* **2001**, *13*, 1984–1991.

(31) Liu, S. P.; Ng, S. C.; Chan, H. S. O. *Synth. Met.* **2005**, *149*, 1–11.

(32) Massey, A.; Park, A. *J. Organomet. Chem.* **1966**, *5*, 218–+.

(33) Rothe, C.; Galbrecht, F.; Scherf, U.; Monkman, A. *Adv. Mater.* **2006**, *18*, 2137–+.

(34) Winokur, M. J.; Slinker, J.; Huber, D. L. *Phys. Rev. B* **2003**, *67*, 184106.

(35) Cadby, A. J.; Lane, P. A.; Mellor, H.; Martin, S. J.; Grell, M.; Giebeler, C.; Bradley, D. D. C.; Wohlgenannt, M.; An, C.; Vardeny, Z. V. *Phys. Rev. B* **2000**, *62*, 15604–15609.

(36) Pei, Q. B.; Yang, Y. *J. Am. Chem. Soc.* **1996**, *118*, 7416–7417.

(37) Leclerc, M. *J. Polym. Sci. Part -Polym. Chem.* **2001**, *39*, 2867–2873.

(38) Greenham, N. C.; Samuel, I. D. W.; Hayes, G. R.; Phillips, R. T.; Kessener, Y. A. R. R.; Moratti, S. C.; Holmes, A. B.; Friend, R. H. *Chem. Phys. Lett.* **1995**, *241*, 89–96.

(39) Dehu, C.; Meyers, F.; Bredas, J. L. *J. Am. Chem. Soc.* **1993**, *115*, 6198–6206.

(40) Cornil, J.; Dos Santos, D. A.; Beljonne, D.; Bredas, J. L. *J. Phys. Chem.* **1995**, *99*, 5604–5611.

(41) Henderson, B.; Imbusch, G. F. *Optical spectroscopy of inorganic solids*; Clarendon Press ; Oxford University Press: Oxford [Oxfordshire]; New York, 1989.

(42) Ishii, H.; Sugiyama, K.; Ito, E.; Seki, K. *Adv. Mater.* **1999**, *11*, 605–+.

(43) Parker, I. D. *J. Appl. Phys.* **1994**, *75*, 1656–1666.

(44) De Boer, B.; Hadipour, A.; Mandoc, M. M.; van Woudenbergh, T.; Blom, P. W. M. *Adv. Mater.* **2005**, *17*, 621–625.

(45) Gong, X.; Ostrowski, J. C.; Moses, D.; Bazan, G. C.; Heeger, A. J. *Adv. Funct. Mater.* **2003**, *13*, 439–444.

(46) *Organic electroluminescent materials and devices*; Miyata, S.; Nalwa, H. S., Eds.; Gordon and Breach Publishers: Amsterdam, 1997.

8.0 Lewis Acids as *p*-Type Dopants for Lewis Basic Polymers

The work in Chapter 7 provides a basis for Chapter 8, in that it demonstrated that Lewis acid-base adducts between the Lewis acid tris(pentafluorophenyl) borane (**BCF**) and a Lewis basic π-conjugated polymer could be used in functional solution processed light-emitting devices. However, many basic questions went unanswered. Perhaps the most important question one can ask is: what happens to the charge transport properties of the polymer after adduct formation? In this chapter, the hole transport properties of a model system comprising the Lewis basic poly[(4,4-diethylhexyldithieno[3,2-b:2′,3′-d]silole)-2,6-diyl-alt-(1,4-pyridyl)-4,7-diyl] (**DTS-Py**) and **BCF** adducts is explored as a function of Lewis acid concentration. Just as in previous reports, the absorption spectra of **DTS-Py** could be red-shifted after addition of **BCF**.

Remarkably, in the electrical transport measurements, it is observed that adduct formation results in a *p*-doped system, whereby the hole mobility could be increased a whole two orders of magnitude relative to the pristine polymer. This was determined using hole-only diodes and analysis of current density-voltage and impedance traces. The hole mobility increase follows because the background carrier density within the film can be increased after adduct formation. Addition of high equivalents of **BCF** results in loss of molecular ordering and a collapse in the hole mobility, despite the large background densities. These observations potentially open the door to a future where *p*-doping of solution processed π-conjugated polymer layers can be realized without the loss of processability that typical charge transfer dopants cause

8.1 Introduction

In inorganic semiconductors, the transition from *intrinsic* to *extrinsic* semiconductor is achieved through doping; i.e. the introduction of impurity states. This ability to controllably dope semiconductors has led to the creation and specific modulation of *p-n* junctions, an essential building block of semiconductor devices found in nearly all digital electronics.[1]

For inorganic semiconductors, the methodology of doping is well established, being first conceptualized in the 1940's. However, for organic semiconductors (OSCs) (and particularly solution-processed OSCs) the availability of dopants and the underlying methodology of molecular doping is still poorly understood.[2,3] Despite this, modern OLED devices benefit heavily from the use of doped transport layers; lowering operation voltages and significantly increasing device efficiencies.[4]

In 1977, it was shown that the conductivity of polyacetylene could be controlled over 11 orders of magnitude by oxidative doping with a variety of halogens.[5] Molecular doping of OSCs was first demonstrated by cosublimation of tetrafluoro-tetracyano-quinodimethane (F_4TCNQ) with phtalocyanine derivatives, achieving *p*-type doping.[6] Ten years later, F_4TCNQ was successfully used to *p*-type dope solution-processed devices.[7,8] Unfortunately, due to differential solubility of F_4TCNQ (dimethylformamide, acetonitrile), the organic semiconductor (common non-polar organic solvents such as toluene, chlorobenzene, etc.), and the F_4TCNQ-OSC charge-transfer complex, achieving high doping concentrations and dense polymer layers necessary for functional devices is extremely challenging.[9] Additionally, because of the energy of F_4TCNQ's lowest unoccupied molecular orbital (LUMO), at -5.2 eV, *p*-doping a wider variety of OSCs is limited (for example those possessing deeper highest occupied molecular orbitals (HOMOs)), requiring the design of a molecule with an *even greater* electron accepting ability. Recent reports suggest that this might not necessarily be the case, but is a good reference point.[10]

In 2009, Welch *et al.* showed that it was possible to modulate the absorption properties of p-conjugated systems bearing an available lone pair (such as nitrogen heteroatoms) by formation of an adduct with a Lewis acid.[11,12] Larger red-shifts in absorption were achieved using stronger Lewis acids (red-shift: $AlMe_3 < B(C_6F_5)_3 < BBr_3$). With this method, a wide variety of optical properties were accessed without the need of extensive molecular design and synthetic effort. This method works by withdrawing electron density from the p-system, narrowing the optical band-gap of the compound. We have recently demonstrated that this method can be extended to functional devices; where we could simultaneously tune the absorption, photoluminescence, and electroluminescence in a model conjugated polymer system.[13] Hitherto, the effect that Lewis acid adduct formation has on the charge-transport properties of the polymer is unknown.

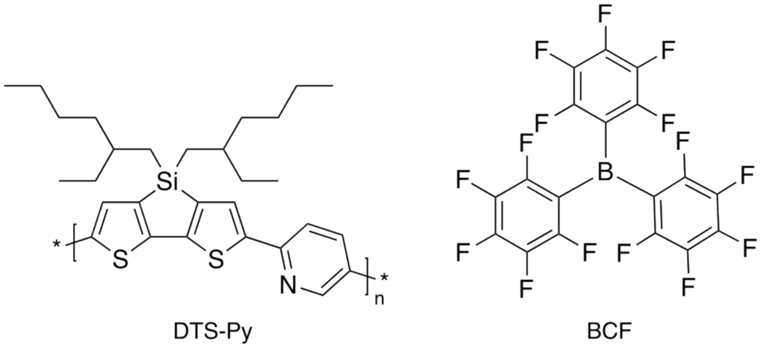

Figure 8.1 Chemical structures of DTS-Py (left) and BCF (right).

We have used a model system comprising the poly[(4,4-diethylhexyldithieno[3,2-b:2′,3′-d]silole)-2,6-diyl-alt-(1,4-pyridyl)-4,7-diyl] (**DTS-Py**) copolymer and tris(pentafluorophenyl)borane (**BCF**) to investigate what effect Lewis acid addition has on the optical and hole-transport properties. The chemical structures of this model system are shown in Figure 8.1. The HOMO and LUMO of **DTS-Py** is -5.00 and -3.45 eV, as determined using cyclic voltammetry (see Figure 8.12 in the appendix).

8.2 Optical Properties

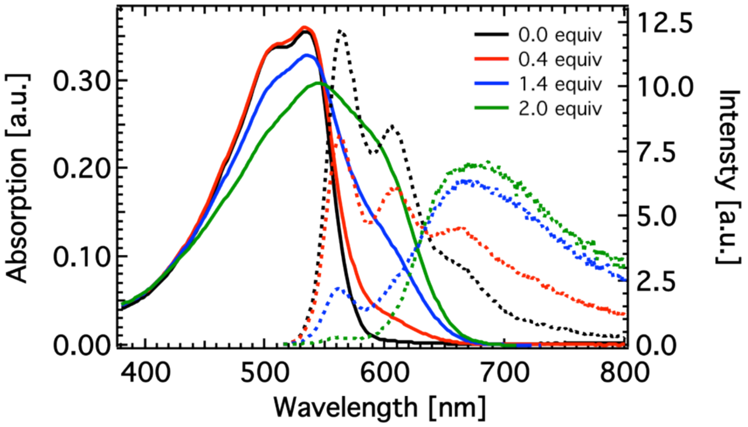

Figure 8.2 Solution absorption (solid lines) and photoluminescence (dashed lines) of DTS-Py and varying amounts of BCF: 0.0 equiv (black line), 0.4 equiv (red line), 1.4 equiv (blue line), and 2.0 equiv (green line). The photoluminescence spectra were all normalized by area to have an area of unity.

First, the solution-state absorption and photoluminescence (area normalized to unity) properties of **DTS-Py** with varying amount of **BCF** were probed (Figure 8.2). The concentration of **DTS-Py** was kept constant at 5.5×10^{-3} mg/mL (1.1×10^{-5} M). The molar extinction coefficient (ε) at the peak absorption of the pristine polymer was found to be 3.1×10^{4} $M^{-1}cm^{-1}$. Upon addition of more and more **BCF**, the absorption spectra red shifts and a new peak grows that is centered at roughly 586 nm. There is an isosbestic point at 548 nm. In the photoluminescence spectra, the addition of more **BCF** results in red-shifted photoluminescence spectra with the pristine photoluminescence peak at 563 nm and the adduct peak emerging at 675 nm. The photoluminescence spectra also seem to show an isosbestic point at ~ 632 nm.

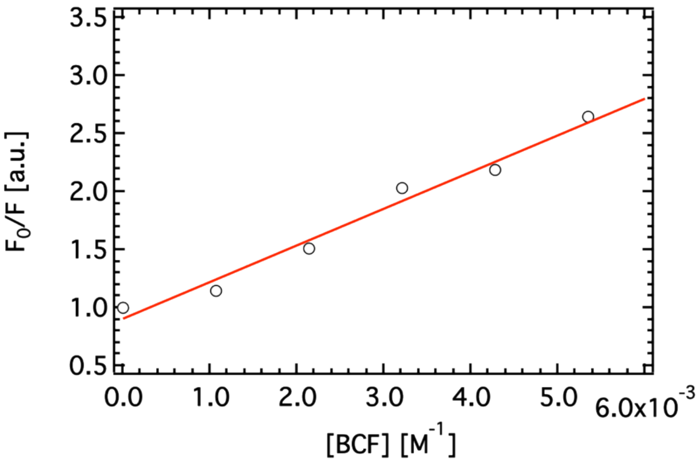

Figure 8.3 Stern-Volmer plot showing the concentration of BCF against the ratio of fluorescence loss in the un-normalized photoluminescence spectra. The red-line is a fit to the data using the Stern-Volmer equation.

By modeling the loss in fluorescence (of the un-normalized data) with increasing **BCF** using the Stern-Volmer relationship, the association constant between **DTS-Py** and **BCF** can be estimated.[14] The data and fit are shown in Figure 8.3. From this data, an association constant of **DTS-Py** and **BCF** of ~ 3 × 10^2 M^{-1} is found, which is in good agreement with nuclear magnetic resonance studies on related polymers and Lewis acids.[12]

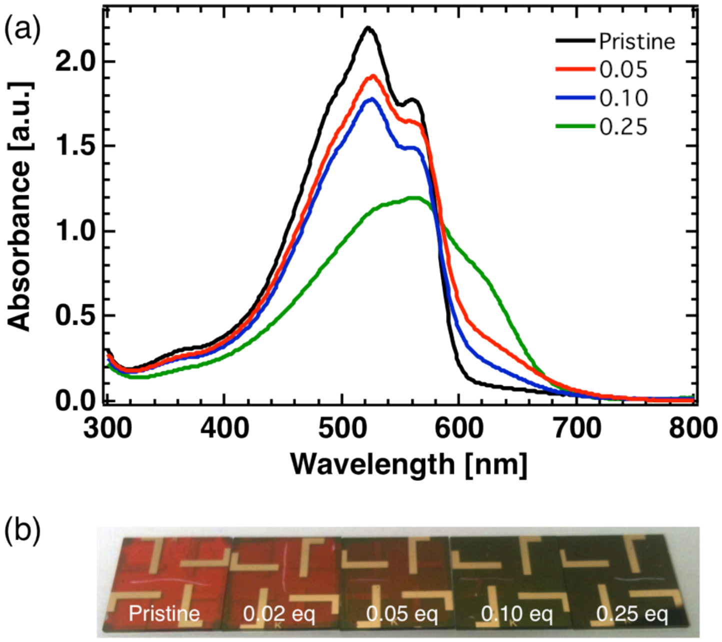

Figure 8.4 (a) Optical absorption of DTS-Py with the following molar equivalent (with respect to repeat unit) additions of BCF: 0.00 (black line), 0.05 (red line), 0.10 (blue line), and 0.25 (green line). (b) Photograph of hole-only devices fabricated using varying molar equivalents of BCF. A clear red shift is observed by increasing the molar equivalents of BCF.

Next, the absorption properties of **DTS-Py**:**BCF** films were evaluated using various molar equivalents of **BCF** (with respect to the repeat unit mass) (Figure 8.4) in order to confirm the formation of the Lewis acid-base adduct. All films were processed using solutions of **DTS-Py** and the appropriate amount of **BCF** in chlorobenzene. Consistent with previous reports on related systems, a significant red-shift reminiscent of doped polymer films is observed upon addition of **BCF** (Figure 8.4).[15,16] As more **BCF** is added, there is a gradual decrease in the main absorption peak centered at 522 nm of the pristine polymer and a growth in the adduct peak at 627 nm with an apparent isosbestic point at 585 nm.

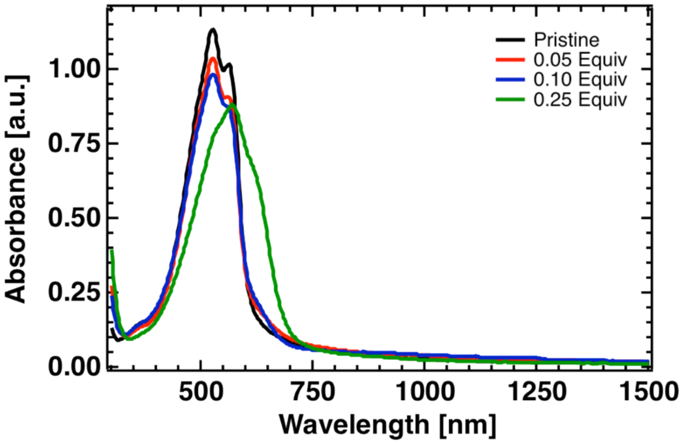

Figure 8.5 Visible-to-near IR optical absorption of DTS-Py with the following molar equivalent (with respect to repeat unit) additions of BCF: 0.00 (black line), 0.05 (red line), 0.10 (blue line), and 0.25 (green line). No new peaks are observed in the region between 1000 and 1500 nm.

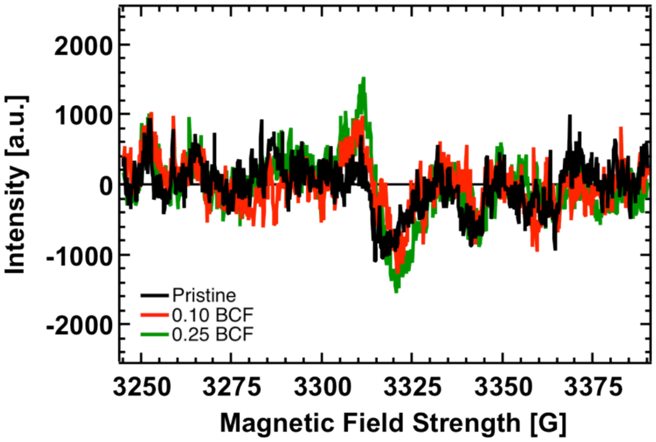

Figure 8.6 EPR spectra for 4% chlorobenzene solutions of DTS-Py (black line) and DTS-Py:BCF with 0.10 (red line) and 0.25 (green line) equivalents of BCF. The response of each sample is comparable to the background noise of the instrument.

With increasing amounts of **BCF**, no new peaks emerge in the near infrared (1000-1500 nm), typical for halogen doped conjugated polymers (Figure 8.5). This is substantiated by electron paramagnetic resonance (EPR) measurements that reveal no stable radicals exist in solution (Figure 8.6).[17] This observation is in stark contrast to systems doped via charge transfer interactions.

8.3 Hole-Only Diodes

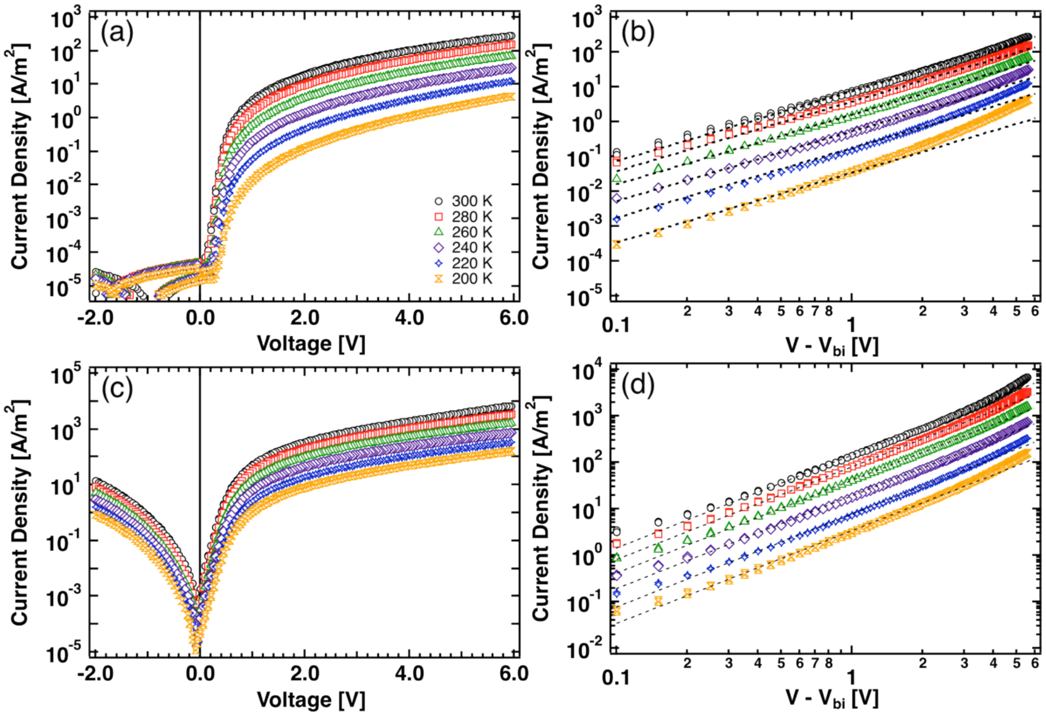

Figure 8.7 (a,c) Temperature dependent hole current of a pristine DTS-Py device (L = 237 nm). (b,d) Temperature dependent hole-current in a DTS-Py device with 0.02 equiv BCF (L = 376 nm). The symbols represent the following temperatures: 300 K (black circles), 280 K (red squares), 260 K (green triangles), 240 K (purple diamonds), 220 K (blue stars), and 200 K (orange hourglasses). Plots (a) and (b) include fits to the trap-free Mott-Gurney Law (dashed black lines). Plots in (a) and (c) highlight the reverse bias injection characteristics for the pristine DTS-Py and DTS-Py with 0.02 equiv BCF, respectively.

To probe the temperature dependent hole mobility of **DTS-Py** and **DTS-Py** upon adduct formation, hole-only devices were fabricated using a general structure of

Au/**DTS-Py** + X mol. equiv. **BCF**/Au. The bottom Au is treated with UV/Ozone and serves as the ohmic injecting contact while the top Au serves as the electron blocking contact.[18,19] Due to problems of Lewis basic compounds with poly(3,4-ethylenedioxythiophene):poly(styrenesulfonate) (PEDOT:PSS), this hole-injection layer is omitted in the device architecture.[20] For low electrical fields and in the absence of traps, the hole mobility is considered to be constant and the current density-voltage (*J-V*) characteristics follow the Mott-Gurney Law for space-charge limited current given by [21]:

$$J = \frac{9}{8}\varepsilon_0 \varepsilon_r \mu_h \frac{V^2}{L^3} \tag{1}$$

where ε_0 is the vacuum permittivity, ε_r is the relative dielectric constant of the material, μ_h is the hole mobility, and L is the active layer thickness. The device current is corrected for the built-in voltage (V_{bi}) that arises from the difference in work function between the anode and cathode contacts. It is important to remember that the work function of metals is highly dependent on the surface composition; for example, the work functions of the top and bottom Au electrodes used in this study have different effective work functions.

The temperature dependent *J-V* characteristics of hole-only devices of pristine **DTS-Py** show typical behavior for disordered conjugated polymers, with a trap-free space-charge mobility of 3.2×10^{-9} m^2/Vs with an Arrhenius-type activation energy of 277 meV, in agreement with previous reports on the universality of temperature activated transport in disordered organic semiconductors.[22] The free-hole density, ρ, in the pristine film is estimated to be roughly 10^{21} m^{-3}.[23] The temperature-dependent current density-voltage characteristics along with trap-free space-charge limited current fits of the pristine hole-only devices are shown in Figure 8.7a. Of note is the excellent rectification of the hole-only devices, consistent with undoped films (Figure 8.7c).

Next, hole-only devices incorporating 0.02 molar equivalents **BCF** were fabricated using he same architecture as the pristine devices. The temperature dependent current and trap-free space-charge limited current fittings are shown in Figure 8.7c,d. Surprisingly, an incredible enhancement of the reverse bias current is observed, as shown in Figure 8.7c, an observation wholly consistent with doped systems where sensitivity of the active layer to electrode work functions is reduced.[24] For example, this effect was observed for F_4TCNQ doped poly(phenylene vinylene) devices.[9] In the **DTS-Py**:**BCF** devices, the mobility is enhanced an incredible 2 orders of magnitude, reaching a value of 3×10^{-7} m^2/Vs with a significantly *reduced* activation energy of 194 meV.

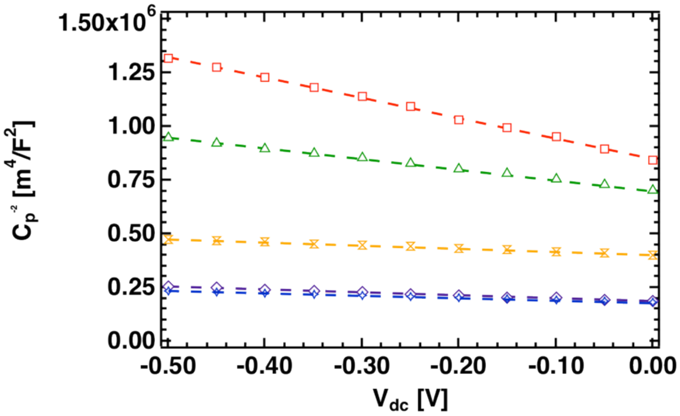

Figure 8.8 Schottky-Mott plot of the depletion capacitance of hole-only devices containing 0.01 (red squares), 0.02 (green triangles), 0.05 (purple diamonds), 0.10 (blue stars), and 0.25 (orange hourglasses) equivalents of BCF. From the slope (dotted lines, Equation 2), the charge density was extracted. Charge densities found using this measurement appear in Table 8.1.

In order to estimate the carrier density in the layer, Schottky-Mott analysis of the device's depletion capacitance was employed using BCF additions that included 0.01, 0.02, 0.05, 0.10, and 0.25 equivalents. This was performed using an impedance analyzer using an alternating voltage of 100 mV while the direct-current voltage was swept from 0 to -0.5 volts. At the same time, the frequency was swept between 100 Hz to 20 MHz. By modeling the device as two RC circuits connected in parallel (one for the device and one for the depletion region), the depletion capacitance (Cp) could be extracted at each DC voltage. The resulting data (Figure 8.8) could be fit to the following equation to determine the background density, denoted as $N_{D:}$[25]

$$N_D = \frac{2}{q\varepsilon_0\varepsilon_r}\left[-\frac{1}{d(1/C_p^2)/dV}\right] \tag{2}$$

where q is the elementary charge. This model is only applicable if the depletion region in the film is smaller than the device thickness. As such, this model cannot be applied to the pristine film. Schottky-Mott analysis of the device's depletion capacitance reveals that by adding 0.02 equivalents of **BCF** the free-hole density in the **DTS-Py** layer is increased to an incredible 10^{24} m^{-3}, though this number may be a 1 order of magnitude overestimation. This shows that the improved mobility observed is merely a consequence of the enhancement in the ρ through the layer.[26,27]

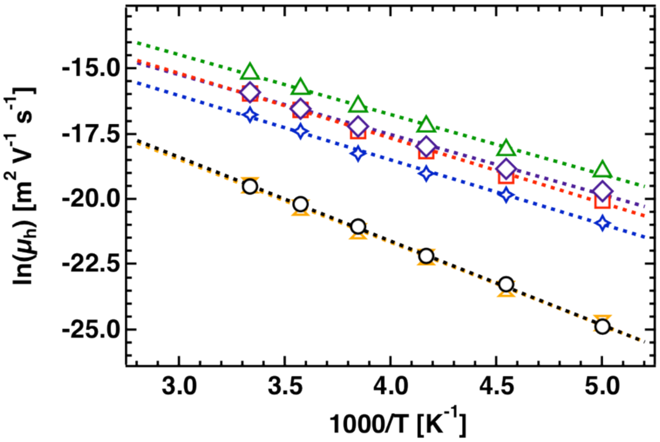

Figure 8.9 Arrhenius plot showing the temperature-dependent mobilities for DTS-Py (black circles) and DTS-Py:BCF films incorporating 0.01 (red squares), 0.02 (green triangles), 0.05 (purple diamonds), 0.10 (blue stars), and 0.25 (orange hourglasses) equivalents BCF. The solid-lines are fits to the Arrhenius equation. The extracted activation energies appear in Table 8.1.

To verify these interesting observations, we explored the temperature dependent mobility for several additions of **BCF**: 0, 0.01, 0.02, 0.05, 0.10, and 0.25 molar equivalents to gain further insight into the doping behavior of this system. These devices were fabricated in the same way at the pristine and 0.02 equivalents **BCF** devices. The extracted trap-free space charge limited current mobilities and temperature dependences are shown as a function of **BCF** additions are displayed in Figure 8.9 and summarized in Table 8.1.

As expected, the increase in mobility concomitantly follows the reduction in activation energy. Addition of low amounts of **BCF** (0.01, 0.02, 0.05 equivalents) results in a two orders of magnitude enhancement of the hole mobility from 3.2×10^{-9} m^2/Vs to 2.5×10^{-7} m^2/Vs and a concomitant reduction of the activation energy from 277 meV to 194 meV. Beyond 0.10 molar equivalents the mobility decreases and the activation energy increases reaching values which are similar to those of pristine films, possibly as a result of disrupted solid-state ordering caused by the bulkiness of **BCF** or by a density-of-states broadening by high doping levels.[28] This issue is addressed in the following subsection.

Table 8.1 Summary of parameters extracted from the temperature-dependent behavior of hole-only devices incorporating various amounts of BCF. The carrier densities were determined using Schottky-Mott analysis of the depletion capacitance (Figure 8.8).

mol. equiv. **BCF**	μ_h [m^2/Vs]	Activation Energy [meV]	Carrier Density [m^{-3}]	V_{bi} [V]
0.00	3.2×10^{-9}	277	3×10^{21}	0.46
0.01	1.5×10^{-7}	212	5×10^{23}	0.33
0.02	2.5×10^{-7}	194	1×10^{24}	0.30
0.05	1.5×10^{-7}	198	4×10^{24}	0.28
0.10	8.2×10^{-8}	204	4×10^{24}	0.22
0.25	3.1×10^{-9}	266	3×10^{24}	0.24

8.4 Morphological Characterization

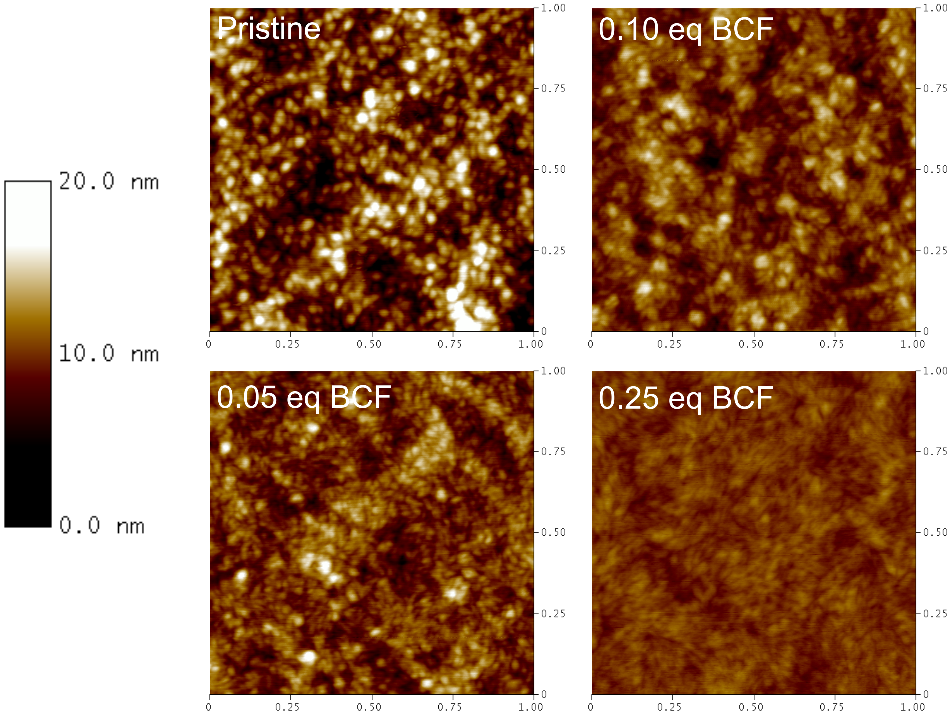

Figure 8.10 Atomic force microscopy images of the surface of DTS-Py and DTS-Py:BCF films. The rms roughness for each film is as follows: 2.9 nm (pristine), 3.0 nm (0.05 eq), 2.9 nm (0.10 eq), and 0.9 nm (0.25 eq). The scan size 1 × 1 µm.

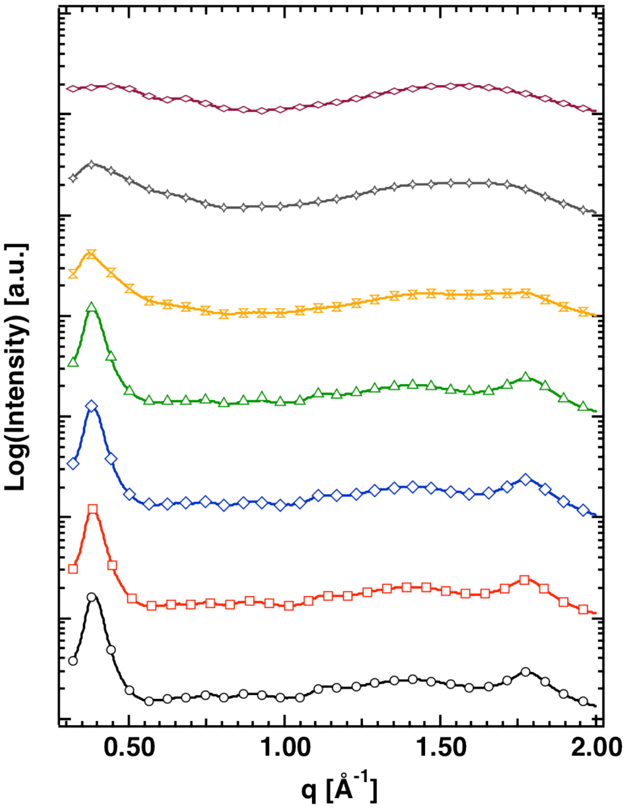

Figure 8.11 Integrated GIWAXS line-scans of DTS-Py and DTS-Py:BCF films containing, from bottom to top, 0.00 (black circles), 0.02 (red squares), 0.05 (blue diamonds), 0.10 (green triangles), 0.25 (orange), 0.50 (gray), and 1.00 (burgundy) molar equivalents of BCF. The alkyl-chain stacking peak appears at about 0.40 Å^{-1} and the π-π stacking peak appears at 1.80 Å^{-1}.

The surface morphology of the devices was examined by tapping-mode atomic force microscopy (Figure 8.10). The pristine film shows some signs of order. However, after adding **BCF** the surface root-mean-square (rms) roughness reduces from 2.9 nm to 0.9 nm for the pristine film and 0.25 molar equivalent **BCF** devices, respectively. Intermediate additions of 0.05 and 0.10 equivalents **BCF** give surface

RMS roughnesses of 3.0 and 2.9 nm, similar to the pristine film. The smoother 0.25 equivalent **BCF** film is smooth, suggesting that addition of **BCF** result in a loss of local order.

In order to further prove this hypothesis, grazing incidence wide-angle x-ray scattering (GIWAXS) measurements was used (Figure 8.11). This was to further confirm that adduct formation disrupts the organization of **DTS-Py**; causing noticeable changes after 0.10 molar equivalents and nearly complete loss of alkyl chain and π-π stacking peaks at 0.25 molar equivalents. This is more extreme for 0.50 and 1.00 molar equivalents of **BCF**, which render the alkyl chain and π-π stacking peaks virtually non-existent.

8.5 Conclusions

With all these observations, it has been shown that *p*-type doping in **DTS-Py** is readily achieved through simple addition of a Lewis acid, specifically **BCF**. These systems do not suffer from the solubility issues of F_4TCNQ-doped systems, where complete solvation of **BCF** and even enhanced solubility of the polymer adduct can be achieved.[9,12] Extraordinarily, a two-orders of magnitude increase in mobility is observed by only adding 0.02 molar equivalents of **BCF**. The increased free hole density on the polymer is realized without observing common features of charge-transfer doping, such as near-infrared absorption or EPR signatures. Addition of high amounts of **BCF** (> 0.10 equivalents) results in a loss of molecular ordering, causing a drop in the hole mobility despite the high background carrier density.[28]

This breakthrough helps to realize the possibility of processing doped polymer layers using large-scale fabrication methods such as roll-to-roll or ink-jet printing. This is primarily due to the solubility of the **DTS-Py**:**BCF** complex in common processing solvents. This methodology holds promise for use in the fabrication of new device structures in different classes of organic electronic devices such as OLEDs, solar cells, or field-effect transistors.

Future studies should revolve around three main themes: mechanisms, synthesis, and application. Mechanistic studies would include evaluation of the doping efficiency (using a variety of different polymer systems), bulk morphological studies (for example, evaluation of **BCF** distribution in the film, changes in crystallinity, etc.), and theoretical calculations of both molecular and bulk properties. Synthetic efforts should focus on inclusion of new functionalities on the Lewis acids that can be stimuli responsive (ideally for sensing applications) and the design of new polymer structures with lone pairs of electrons to accommodate adduct formation. Additional synthetic efforts could also be the design of Lewis acidic polymers, in hopes of *n*-type doping using Lewis bases; the opposite of the system that has been have studied. Finally, applications could be extended to fabrication of new device structures using this new method of doping – creation of hole-injection layers, organic field-effect transistors, or even fabrication of *p*-*n* junctions for light emitting devices or solar cells.

8.6 Experimental Methods

Materials: Anhydrous chlorobenzene was obtained from Acros Organics and used as received. **BCF** was purified by sublimation before use.

Synthesis of ***DTS-Py***: 5,5'-Bis(trimethylstannyl)-3,3'-di-2-ethylhexylsilylene-2,2'-bithiophene (220 mg, .295 mmol) and 2,5-dibromopyridine (70 mg, 0.295 mmol) were added to a 5 mL microwave tube with $Pd(PPh_3)_4$ (cat. 5 mol %) and toluene (3 mL) in a N_2 filled glovebox and sealed with a Teflon® cap. The reaction mixture was heated to 120 °C for 3 minutes, 140 °C for 3 minutes, and 160 °C for 60 minutes, using a Biotage microwave reactor. 2-(tributylstannyl)thiophene was then added using a syringe and the mixture was heated to 120 °C for 3 minutes, 140 ºC for 3 minutes, and 160 °C for 15 minutes in the microwave reactor. 2-bromothiophene was then added using a syringe and the mixture was heated to 120 °C for 3 minutes, 140 ºC for 3 minutes, and 160 °C for 15 minutes in the microwave reactor. Upon completion, the mixture was precipitated in stirring methanol, filtered, and purified using Soxhlet extraction in methanol, acetone and hexanes. **^{1}H NMR** ($CDCl_3$): $\delta =$ 8.8 (m, 1H), 7.8 (m, 1H), 7.7-7.5 (m, 2H), 7.3 (m, 1H), 1.6-1.5 (m, 2H) 1.4-1.2 (m, 16H), 1.1-1.0 (m, 4H), 0.9-0.7 (m, 12H). **GPC** (1,3,5-trichlorobenzene, 150 °C): M_n = 12 kg/mol.

Hole-Only Device Fabrication: Corning glass substrates were scrubbed thoroughly with detergent and sonicated in acetone and isopropanol. Following the cleaning procedure, patterned contacts consisting of 1 nm of Ti and 30 nm of Au were deposited onto the substrates in a thermal evaporator at a pressure of less than 1×10^{-6} torr. The Au substrates were treated to 30 min of UV/Ozone to improve the wetting of the polymer solution. The **DTS-Py**:**BCF** solutions were spin-coated from chlorobenzene solutions atop the patterned substrates and spun at a variety of speeds in a nitrogen atmosphere. The 60 nm thick Au top contact was deposited in a thermal evaporator, also at a pressure of less than 1×10^{-6} torr.

Electrical Measurements: The temperature-dependent *I-V* characteristics of the hole-only devices were measured using a Keithley 4200 semiconductor analyzer with the sample placed in a variable temperature probe station (Lake Shore Cryotronics, Inc.) and measured at a pressure of $< 1 \times 10^{-6}$ torr. Impedance analysis was performed using a Solartron SI 1260. Film thicknesses were determined using an Ambios XP-100 profilometer.

GIWAXS: GIWAXS was performed at Stanford Synchrotron Radiation Lightsource beamline 11-3 using a photon energy of 12.7 keV, a MAR345 image plate area detector, a helium filled sample chamber and an incident angle of approximately 0.12˚. For GIWAXS measurements films were spin cast on Si wafers from solutions identical to those used for electrical measurements. GIWAXS measurements were done by Alexander Sharenko (UCSB).

Other Characterization: Thin-film absorption was measured using a Perkin-Elmer Lambda 750 UV-Vis spectrometer. The EPR spectra were collected using a Bruker EMXplus EPR spectrometer. All atomic force microscopy images were measured under an inert atmosphere of nitrogen. Images were obtained using a MultiMode AFM (Veeco). Silicon probes with a spring constant of ~5 N/m and resonant frequencies of 75 kHz (Budget Sensors) were used for tapping mode measurements. Cyclic voltammetry (CV) of **DTS-Py** was performed using a glassy carbon working electrode, a Pt wire counter electrode, and an Ag reference electrode. The supporting electrolyte was 0.1 M Bu_4NPF_6 in dichloromethane and the scan rate was 100 mV/s. The determined HOMO and LUMO values were -5.00 and -3.45 eV, respectively (See appendix Figure 8.12 for CV spectrum).

8.7 Appendix

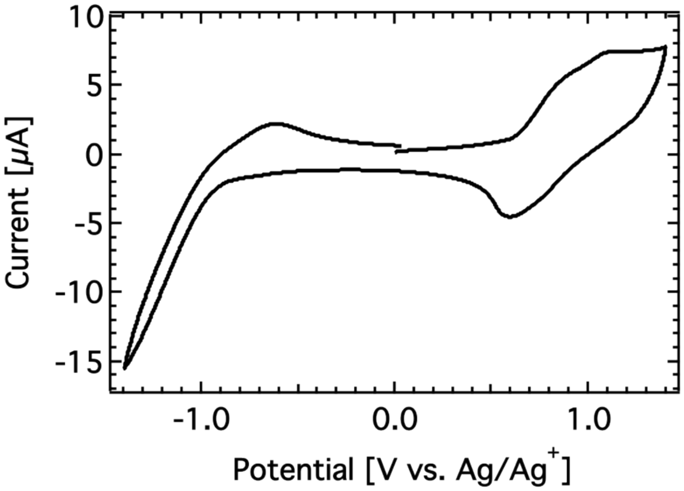

Figure 8.12 Cyclic voltammogram (CV) of pristine DTS-Py as measured in dichloromethane using a glassy carbon working electrode, Pt wire counter electrode, and an Ag reference electrode. The supporting electrolyte is 0.1 M Bu_4NPF_6 in dichloromethane and the scan rate was 100 mV/s.

8.8 References

(1) Sze, S. M. *Physics of semiconductor devices*; 3rd ed.; Wiley-Interscience: Hoboken, N.J, 2007.

(2) Guo, S.; Kim, S. B.; Mohapatra, S. K.; Qi, Y.; Sajoto, T.; Kahn, A.; Marder, S. R.; Barlow, S. *Adv. Mater.* **2012**, *24*, 699–703.

(3) Walzer, K.; Maennig, B.; Pfeiffer, M.; Leo, K. *Chem. Rev.* **2007**, *107*, 1233–1271.

(4) Pfeiffer, M.; Leo, K.; Zhou, X.; Huang, J. .; Hofmann, M.; Werner, A.; Blochwitz-Nimoth, J. *Org. Electron.* **2003**, *4*, 89–103.

(5) Shirakawa, H.; Louis, E. J.; MacDiarmid, A. G.; Chiang, C. K.; Heeger, A. J. *J. Chem. Soc. Chem. Commun.* **1977**, 578.

(6) Blochwitz, J.; Pfeiffer, M.; Fritz, T.; Leo, K. *Appl. Phys. Lett.* **1998**, *73*, 729–731.

(7) Yim, K.-H.; Whiting, G. L.; Murphy, C. E.; Halls, J. J. M.; Burroughes, J. H.; Friend, R. H.; Kim, J.-S. *Adv. Mater.* **2008**, *20*, 3319–3324.

(8) Sivaramakrishnan, S.; Zhou, M.; Kumar, A. C.; Chen, Z.-L.; Png, R.-Q.; Chua, L.-L.; Ho, P. K. H. *Appl. Phys. Lett.* **2009**, *95*, 213303.

(9) Zhang, Y.; de Boer, B.; Blom, P. W. M. *Adv. Funct. Mater.* **2009**, *19*, 1901–1905.

(10) Méndez, H.; Heimel, G.; Opitz, A.; Sauer, K.; Barkowski, P.; Oehzelt, M.; Soeda, J.; Okamoto, T.; Takeya, J.; Arlin, J.-B.; Balandier, J.-Y.; Geerts, Y.; Koch, N.; Salzmann, I. *Angew. Chem. Int. Ed.* **2013**, *52*, 7751–7755.

(11) Welch, G. C.; Coffin, R.; Peet, J.; Bazan, G. C. *J. Am. Chem. Soc.* **2009**, *131*, 10802–+.

(12) Welch, G. C.; Bazan, G. C. *J. Am. Chem. Soc.* **2011**, *133*, 4632–4644.

(13) Zalar, P.; Henson, Z. B.; Welch, G. C.; Bazan, G. C.; Nguyen, T.-Q. *Angew. Chem. Int. Ed.* **2012**, *51*, 7495–7498.

(14) Lakowicz, J. R. *Principles of fluorescence spectroscopy*; 3rd ed.; Springer: New York, 2006.

(15) Furukawa, Y. *J. Phys. Chem.* **1996**, *100*, 15644–15653.

(16) Holt, A. L.; Leger, J. M.; Carter, S. A. *J. Chem. Phys.* **2005**, *123*, 044704.

(17) Krinichnyi, V. I. *Synth. Met.* **2000**, *108*, 173–222.

(18) Rentenberger, S.; Vollmer, A.; Zojer, E.; Schennach, R.; Koch, N. *J. Appl. Phys.* **2006**, *100*, 053701.

(19) *Physics of organic semiconductors*; Brütting, W.; Adachi, C.; Holmes, R. J. D., Eds.; 2nd completely new rev. ed.; Wiley-VCH: Weinheim, 2012.

(20) Garcia, A.; Welch, G. C.; Ratcliff, E. L.; Ginley, D. S.; Bazan, G. C.; Olson, D. C. *Adv. Mater.* **2012**, *24*, 5368–5373.

(21) Lampert, M. A. *Current injection in solids*; Electrical science; Academic Press: New York, 1970.

(22) Craciun, N.; Wildeman, J.; Blom, P. *Phys. Rev. Lett.* **2008**, *100*, 056601.

(23) Craciun, N.; Brondijk, J.; Blom, P. *Phys. Rev. B* **2008**, *77*, 035206.

(24) Zhang, Y.; de Boer, B.; Blom, P. W. M. *Phys. Rev. B* **2010**, *81*, 085201.

(25) Rhoderick, E. H. *Metal-semiconductor contacts*; Monographs in electrical and electronic engineering; 2nd ed.; Clarendon Press ; Oxford University Press: Oxford [England] : New York, 1988.

(26) Pasveer, W.; Cottaar, J.; Tanase, C.; Coehoorn, R.; Bobbert, P.; Blom, P.; de Leeuw, D.; Michels, M. *Phys. Rev. Lett.* **2005**, *94*, 206601.

(27) Tanase, C.; Meijer, E. J.; Blom, P. W. M.; de Leeuw, D. M. *Phys. Rev. Lett.* **2003**, *91*, 216601.

(28) Arkhipov, V.; Heremans, P.; Emelianova, E.; Bässler, H. *Phys. Rev. B* **2005**, *71*, 045214.

9.0 Reduced Langevin Recombination in Small Molecule Organic Solar Cells

In this chapter, the recombination dynamics in two benchmark small molecule bulk heterojunction solar cell systems are studied using steady state measurements of the hole, electron, and effective mobility. In literature, it has been shown that recombination in polymer bulk heterojunction solar cells rarely follow from the predicted recombination rate that would follow from Langevin kinetics. To compensate for this difference, a so-called reduction factor is multiplied by the Langevin rate to arrive at the true recombination rate. Naturally, for a high performance solar cell it is preferred to have as small of a reduction factor as possible, since it means that the layer can accommodate more charges than the space charge limit would allow. Many researchers have posited that this reduction factor originates in the morphology of the bulk heterojunction. For example, these might be the formation of pure and crystalline donor and acceptor domains or morphology motifs such as lamellae. In this work it is shown that formation of these structures, as determined by techniques such as transmission electron microscopy or x-ray diffraction techniques, do not necessarily lead to reduction factors. The conclusions in this chapter suggest that larger reduction factors have less to do with bulk morphologies and more to do with donor:acceptor interfaces and system-specific energetics (i.e. offset between the lowest unoccupied molecular orbitals of the donor and acceptor).

9.1 Introduction

Progress in increasing the power conversion efficiency (PCE) of organic bulk heterojunction (BHJ) solar cells can primarily be attributed to efforts in developing novel π-conjugated donor materials. However, of late, researchers are willing to stop to specifically quantify and understand the mechanisms that lead to a certain device performance. For charge carriers, thermodynamics play a big role. For example, Planck's Law for black body radiation is an unavoidable loss mechanism that forces carriers to recombine.[1]

Most efforts understanding carrier recombination in organic solar cells have focused on understanding the recombination of *free* carriers.[2] From external quantum efficiency (EQE), photoluminescence (PL), and electroluminescence (EL) experiments, it has been shown that the majority of recombination events occur at the donor:acceptor interface through a so-called charge transfer (CT) state.[3] The energetics of the emissive charge transfer state strongly correlates with the open-circuit voltage (V_{oc}) that is observed under one sun. This observations points to the fact that recombination through the CT state is more significant than just dictating the V_{oc} and photocurrent losses in a solar cell.[4]

In general, to realize optimize organic BHJ solar cells, the electron and hole distribution through the layer should be equal; in other words, more closely following the injected plasma limit.[5] This situation would allow the active layer of the solar cell to hold more free charges than the space-charge limit would traditionally allow.[6] Unfortunately, this ideal distribution hardly exists. This is mostly due to factors such as energetic disorder and prevalence and distribution of percolation pathways that ultimately lead to varying recombination strengths through the active layers of actual devices.[7] In the absence of traps, the maximum recombination strength possible in organic semiconductors, and more specifically in an organic BHJ is defined by Langevin recombination. Langevin recombination is defined as being the characteristic diffusion of free electrons and holes toward one another in a mutual Columbic field.[8] The Langevin recombination rate is defined by the following equation:

$$k_L = \frac{q}{\varepsilon_0 \varepsilon_r}\left(\mu_e + \mu_h\right) \tag{1}$$

where k_L is the Langevin recombination rate, q is the elementary charge, e_0 is the vacuum permittivity, ε_r is the relative dielectric constant, and μ_e and μ_h are the electron and hole mobilities respectively. It's important to note that the recombination rate will depend on temperature (T), carrier density (ρ), and electrical field (E). This is due to the mobility's dependence on these parameters.[6,9]

In a stroke of luck, several polymer:fullerene BHJs have recombination strengths that do not follow from the predicted Langevin rates.[2] This is a surprising result considering Langevin-type recombination has been theoretically predicted for systems with a combination of Gaussian disorder, trap-free, and low carrier mobilities for electrons and holes.[7] This is due to the idea that typically hopping distances for charges (1-2 nm) is much smaller than the Columbic capture radius in organic materials. In any case, deviations from Langevin recombination necessitate the introduction of a reduction factor, γ_{pre}, which scales the Langevin rate to arrive at the true recombination rate, k_R (2). This pre-factor is usually between 10^{-3} and 10^{-1} and strongly depends on the donor:acceptor system and processing conditions used.[6,10–12]

$$k_R = \gamma_{pre} k_L \tag{2}$$

From this relationship, a smaller γ_{pre} is desirable as it leads to weaker recombination strengths than the Langevin rate would predict. The consequence of this is that more charges can be extracted in the active layer. The value of γ_{pre} has been hypothesized to be related to mostly morphological effects. For example, when the active layer has pure donor and acceptor domains with an adequate amount of phase separation.[11] Another hypothesis supposes that 2-D Langevin recombination in lamellae such as those found in poly(3-hexylthiophene-2,5-diyl):[6,6]-phenyl C_{61} butyric acid methyl ester (P3HT:PC_{61}BM) blends may also cause a smaller γ_{pre}.[13] However, these theories have not been proven and are only speculative. This is why only with further investigation of structurally and morphologically diverse systems that one can start to gain insight into what factors influence the γ_{pre} in these systems.

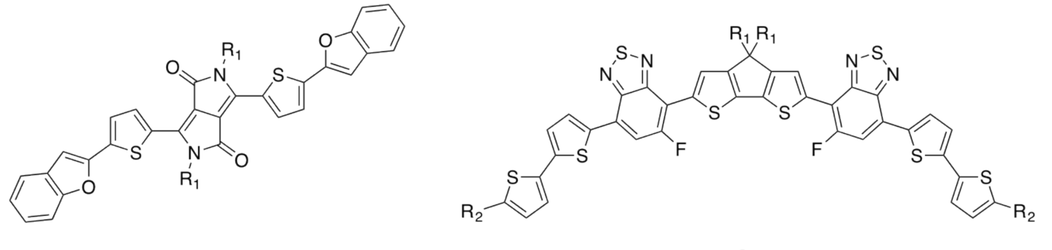

DPPBFu **DTSFBT**

Figure 9.1 Chemical structures of DPPBFu and DTSFBT. R_1 = 2-ethylhexyl and R_2 = n-hexyl.

In small molecules, the recombination behavior has been largely unexplored even though their PCEs have improved rapidly to 8.1% in the span of four years. Two examples of these systems are the donors: 3,6-bis(5-(benzofuran-2-yl)thiophen-2-yl)-2,5-bis(2-ethylhexyl)pyrrolo[3,4-c]pyrrole-1,4-dione, (**DPPBFu**), and 7,7′-(4,4-bis(2-ethylhexyl)-4H-silolo[3,2-b:4,5-b′]dithiophene-2,6-diyl)bis(6-fluoro-4-(5′-hexyl-[2,2′-bithiophen]-5-yl)benzo[c][1,2,5]thiadiazole) (**DTSFBT**).[14,15] In optimized structures, [6,6]-phenyl C_{71} butyric acid methyl ester (PC71BM) acts as the acceptor. The chemical structures of the donor materials appear in Figure 9.1.

Recent research on these systems has focused on optimizing device performance through searches for better processing conditions and device architectures.[16–19] In both **DPPBFu** and **DTSFBT**, structural characterization has attempted to correlate device performance with processing conditions.[20–22] For these small molecule donors, as-cast blends with PC71BM have poor performance that is mainly attributed to homogeneous mixing of donor and acceptor that leads to largely non-existent phase separation.[20,21] Annealing blends with these materials leads to the creation of large crystalline donor domains and the creation of phase separated donor and acceptor domains, resulting in better device performance. In the same manner, addition of high boiling solvent additives to **DTSFBT**, such as 1,8-diiodooctane (DIO) resulted in slightly smaller domain sizes, leading to PCEs that were close to 7%.[15]

In summation, this previous work has shown that the PCE of small molecule BHJs is incredibly sensitive to the set of processing conditions and device architecture utilized. Compared to polymeric systems, small molecule BHJs can achieve a higher degree of crystallinity. This is an indication that regions of relatively pure and optimally sized donor and acceptor domains are created and that the interfacial orientation between donor:acceptor molecules is likely more favorable. Since the crystallinity in these systems can be relatively easily controlled, they provide a good platform for understanding the effect of BHJ morphologies on charge carrier recombination mechanisms and dynamics.

Most literature reports that deal with carrier recombination in organic BHJs relies on the use of transient techniques like time-of-flight (TOF), photo-charge extraction by linearly increasing voltage (CELIV), and double-injection transients.[23,24] Recently, a new steady-state technique has emerged where γ_{pre} can be determined from single- and double-carrier devices using the extracted trap-free hole, electron, and effective mobilities (Equation 3). This equation is a least-squares approximation of the two limits of slow (infinitesimal recombination, injected plasma limit) and infinite (back to back diode) recombination.[6]

$$\gamma_{pre} = \frac{16\pi}{9} \frac{\mu_e \mu_h}{\mu_d^2 - \left(\mu_e + \mu_h\right)^2} \tag{3}$$

In this equation, μ_e, μ_h, and μ_d are the electron, hole, and effective (dual carrier) mobilities. By inserting the obtained γ_{pre} into Equation (2), the total recombination rate for the system, can be obtained. A caveat of Equation (3) is that the electron, hole, and dual carrier devices must have trap-free conduction – meaning that trap-assisted recombination can be neglected. In organic solar cells this is reasonable since the V_{oc} typically scales with the light intensity with a slope of kT/q. Slopes greater than *kT/q* are caused by trap-assisted Shockley-Read-Hall recombination, as nicely exemplified for polymer light-emitting diodes.[25,26] The advantage of the steady-state approach in Equation (3), relative to the transient techniques, is that only three types of devices must be fabricated (electron-only, hole-only, and dual carrier) in dimensions similar to bulk devices and determination of charge carrier mobilities proceeds using well-established models. In this chapter, determination of carrier mobilities is done using the Mott-Gurney Law in the space charge limited current regime (Equation 4):[27]

$$J = \frac{9}{8}\varepsilon_0 \varepsilon_r \mu \frac{V^2}{L^3} \tag{4}$$

where μ is the zero field mobility and L is the device thickness. Uses of Murgatroyd or Poole-Frenkel type field-dependent mobility models are completely incorrect. Use of these models may lead to gross overestimations in the carrier mobility. These models are incorrect due to the stronger carrier density dependence of mobility than on electrical field.[28] This is even more especially true for high mobility systems.

9.2 Bulk Recombination Mechanism

In both **DPPBFu** and **DTSFBT** solar cells, it has been suggested a large density of charge traps that originate from grain boundaries or interface traps influences carrier recombination.[16,19,29] As mentioned previously, by measuring the V_{oc}'s dependence on light intensity, it is straightforward to differentiate between trap-free and trap-assisted recombination.[26] At V_{oc}, all generated carriers recombine, thus giving Equation (5) as originally proposed by Schiff:[30]

$$V_{oc} = \frac{E_{gap}}{q} - \frac{kT}{q}\ln\left(\frac{(1-P)k_L N_{cv}^2}{PG}\right) \qquad (5)$$

where E_{gap} is the effective band-gap, q is the elementary charge, k is the Boltzmann constant, T is temperature, P is the dissociation probability of electron-hole pairs, G is the generation rate of bound-electron hole pairs, and kT/q is the thermal voltage. The presence of trap-assisted recombination increases the slope to values greater than kT/q, as first shown by Mandoc.[26]

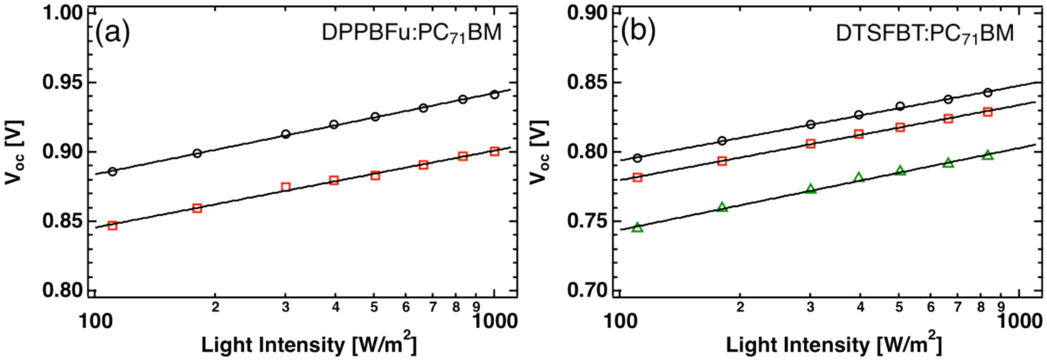

Figure 9.2 The V_{oc} as a function of light intensity for: as-cast (black circles, kT/q = 1.00) and annealed (red squares, kT/q = 0.94) DPPBFu:PC71BM devices (a) and as-cast (black circles, kT/q = 0.91), annealed (red squares, kT/q = 0.92), and DIO (green triangles, kT/q = 1.00) DTSFBT:PC71BM devices (b). The black solid lines are fits to Equation (5).

The V_{oc}-light intensity dependence for **DPPBFu** and **DTSFBT** blends, processed from various conditions, were measured using conventional solar cell architectures of: indium-tin-oxide (ITO)/ poly(3,4-ethylenedioxythiophene):poly(styrenesulfonate) (PEDOT:PSS)/active layer/Ca/Al.

The resulting data from this experiment is shown in Figure 9.2. All the V_{oc}s depend on a *kT/q* that is between 0.90 and 1.00 *kT/q* for all processing conditions: as-cast and annealed for **DPPBFu**:PC71BM and as-cast, annealed, and DIO for **DTSFBT**:PC71BM. This data means that the presence of trap-assisted recombination is negligible in all processing conditions. It is important to stress that for these measurements the diode quality must be very high or in other words, that the leakage currents are very low. At low light intensities, leakage currents can affect the measured V_{oc}. This is the primary reason the results presented herein disagree with published literature.[19,31] Recent reports that conclude that cathode thickness modify the degree of trap-assisted recombination in these systems is incorrect and are simply a consequence in changes in the diode quality.

This observation can later be further confirmed by single-carrier measurements that should show both hysteresis free current density-voltage (*J*-*V*) curves and by considering the current and thickness scaling according to the Mark and Helfrich formalism.[32,33] This check of the V_{oc}-light intensity scaling gives sufficient motivation to continue to determination of the steady-state carrier mobilities and recombination dynamics, as will be shown in the following subsections

9.3 Hole, Electron, and Double Carrier Transport in Small Molecule Blends

In order to properly use Equation (3), accurate measurements of the hole, electron, and effective mobilities is paramount. Usually, increasing the thickness of the active layer in a device would help to extend the space-charge region of the curve. However, processing small molecules with adequate thicknesses is challenging due to either their poor solubility or low solution viscosity. Additionally, BHJ solar cells typically optimize at thicknesses of only 100 – 150 nm. An accurate measurement of the mobility in this thickness range is necessary to mimic real working solar cell devices.

An important detail in reference 6 is the use of Au as an anode contact for hole-only and double-carrier devices. The higher conductivity and lower series resistance of an Au contact relative to ITO contact should allow for larger current densities and thus a larger voltage range over which Equation (4) can be fit. Larger series resistances may dampen the device currents, complicating analysis. For this study, Au contacts are used since the mobilities and reduction factors cannot be known *a priori*.

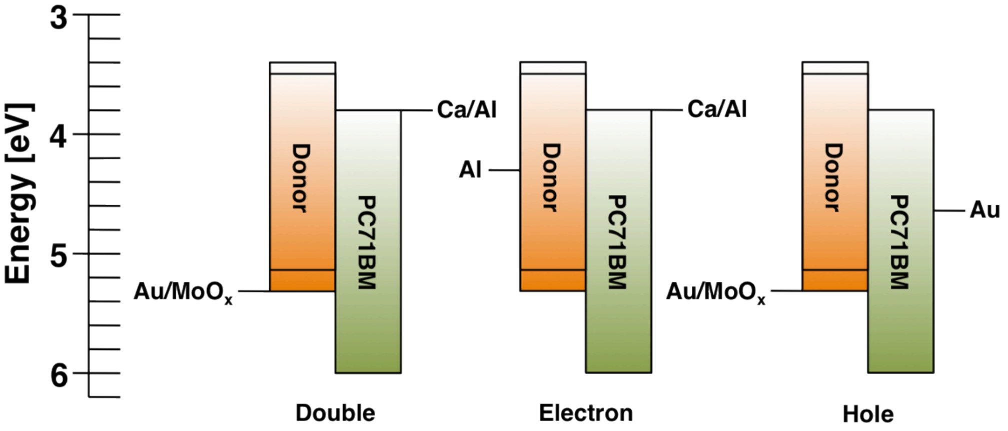

Figure 9.3 Energy level diagram showing the device architectures for hole-only, electron-only, and double carrier diodes for DPPBFu:PC71BM and DTSFBT:PC71BM blends. The work function of Ca is -2.8 eV. The work function of MoO$_x$ is -5.4 eV, as shown in reference 34. The HOMO and LUMO levels of DPPBFu, DTSFBT, and PC71BM were acquired from references 14 and 15.

So that the transport in **DPPBFu**:PC71BM and **DTSFBT**:PC71BM blends can be properly determined, the following device structures were used: Au/MoO$_x$/active layer/Au (hole-only diode), Al/active layer/Ca/Al (electron-only diode), and Au/MoO$_x$/active layer/Ca/Al (double-carrier diode). A summary of these device architectures is shown in Figure 9.3.

In all measurements, the devices show clear diode behavior, with linearly scaling leakage current at low voltages, followed by an exponential regime that transitions to the space-charge limited current regime at just beyond the built-in voltage (V_{bi}). The V_{bi} roughly matches the difference between the work functions of the anode and cathode. In the double-diode device, this is quite close to the V_{oc} measured at one sun. After correcting for the built in voltage, the *J-V* traces can be fit to the Mott-Gurney Law (Equation 4).

A. DPPBFu:PC71BM Blends

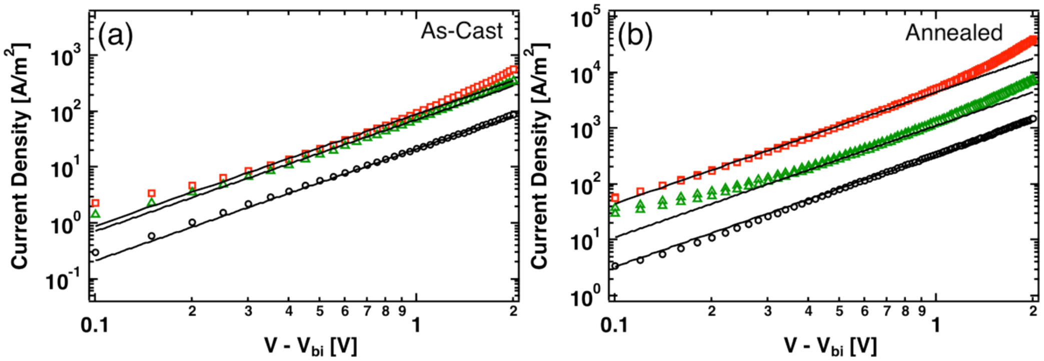

Figure 9.4 Room temperature (295 K) *J-V* characteristics of hole-only (black circles), electron-only (green triangles), and double-diode (red squares) devices of as-cast (a, L = 167 nm) and annealed (b, L = 162 nm) DPPBFu:PC71BM blends. The black solid lines are fits to the Mott-Gurney Law (Equation 4).

Figure 9.4 shows a complete summary of typical *J-V* traces for single- and double-carrier diodes of **DPPBFu**:PC71BM blends as measured in the as-cast and annealed conditions. The values obtained for hole, electron, and double carrier mobilities appear in Table 9.1, at the end of this section. In the same way that thermal annealing improves the device performance of bulk BHJ devices, it also has a large influence on the hole, electron, and effective mobilities. In these categories, thermal annealing of **DPPBFu**:PC71BM blends realizes an increase in all mobilities of roughly one order of magnitude. In the hole transport this translates to an increase from 3.4×10^{-9} to 4.7×10^{-8} m^2/Vs. These values contradict previous publications that claim that thermal annealing does not cause any changes in hole mobility, but this discrepancy can be attributed to a lack of using Au/MoOx bottom contacts.[14] In the electron mobility, the increase is from 1.0×10^{-8} to 1.6×10^{-7} cm^2/Vs. The effective mobility rises from 1.0×10^{-8} to 6.3×10^{-7} m^2/Vs after annealing.

Using Equation (3) shown earlier, the reduction factor and resulting recombination rate can be readily obtained. Surprisingly, the as-cast reduction factor is ~ 1, meaning that the bimolecular recombination rate follows directly from Langevin predictions. Quantitatively, this means that for as-cast blends, $k_R = k_L = 7.0 \times 10^{-17}$ m^3/s. After thermal treatment, the calculated reduction factor is 0.12, giving a recombination rate of 1.3×10^{-16} m^3/s. See Table 9.2 for a summary of all recombination parameters for the DPPBFu:PC71BM blends.

The change in reduction factor seems to correlate well with structural analysis which shows as-cast blends are a homogenous mixture of donor and acceptor with little phase separation.[20] After thermal annealing, phase separated donor-rich and acceptor-rich domains emerge. This observation seems to support hypothesized relationships between phase separation and reduced Langevin recombination. In spite of this, it will be shown that for **DTSFBT**:PC71BM blends, these correlations that could be drawn from bulk structural analysis are most likely invalid.

B. DTSFBT:PC71BM Blends

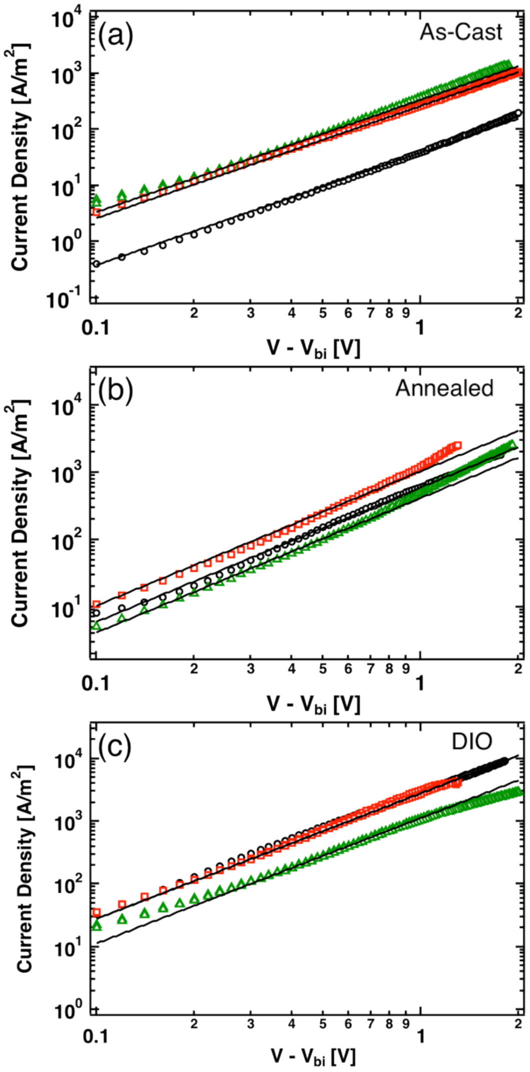

Figure 9.5 Room temperature (295 K) J-V characteristics of hole-only (black circles), electron-only (green triangles), and double-diode (red squares) devices of as-cast (a, L = 95 nm), annealed (b, L = 100 nm), and DIO (c, L = 79 nm) processed DTSFBT:PC71BM blends. The black solid lines are fits to the Mott-Gurney Law.

The recombination **DTSFBT**:PC71BM blends in the same way that **DPPBFu**:PC71BM blends were using identical device structures for all measurements (Figure 9.3). The typical J-V characteristics for **DTSFBT**:PC71BM blends in the as-cast, annealed, and DIO processed conditions are shown in Figure 9.5. The parameters extracted from these devices are shown in Table 9.1 and Table 9.2.

Just like **DPPBFu**:PC71BM blends, thermal annealing lead to one order increases in the hole mobility, from 1.1 × 10^{-9} to 2.2 × 10^{-8} m^2/Vs. Love *et al.* suggested that a higher electrical field was needed for charges to be swept out of the film causing a low fill factor (*FF*); a signature of low or imbalanced mobilities.[24] Annealing and processing from DIO alleviates this problem. Processing **DTSFBT**:PC71BM blends using DIO caused a moderate increase in hole mobility to 4.6 × 10^{-8} m^2/Vs. The higher mobility observed as a consequence of processing conditions is consistent with the increases in device performance (from the as-cast 1.8% to the DIO 7%) and *FF*s. For all processing conditions, the electron mobility remains fairly constant at about 1.0 × 10^{-8} m^2/Vs. Even though transmission electron microscopy characterization implies that the as-cast blends lack phase separation, this does not affect the electron transport. Even without observable phase separation, there are sufficient percolative networks in PC71BM to achieve high electron mobilities.

The double carrier mobilities were also determined for **DTSFBT**:PC71BM blends. For all conditions, the double-carrier current matches with the current of the single-carrier diode with the higher mobility. The effective mobilities determined were 7.1 × 10^{-9}, 3.5 × 10^{-8}, and 4.6 × 10^{-8} m^2/Vs for the as-cast, annealed, and DIO processed films, respectively. Clearly, by inspecting Equation (3) and the *J-V* traces in Figure 9.5, the recombination factor for all three processing conditions of **DTSFBT**:PC71BM blends is 1. This is a remarkable observation, since the grazing incidence wide-angle scattering (GIWAXS) and TEM measurements of the blends show vastly different solid-state organization and phase separation.[21,22] These differences do not then reach further into the transport and recombination behavior in the device.

Previous publications on **DTSFBT**:PC71BM blends show that the main origin for improvements in device performance as a function of processing condition is related to the generation and dissociation of excitons. Thus, the changes in device performance among the three conditions can be rationalized in the following way. In the as-cast condition, the device is mainly hampered by imbalanced mobilities. In the annealed condition, large domains (significantly larger than the exciton diffusion length) limit the device performance and lower the photocurrent. The use of DIO changes the domain size, resulting in higher photocurrent yields compared to the annealed device.[21] In combination with the field-dependence of geminate recombination for the as-cast and annealed conditions and a lack of for the DIO condition, changes in performance for **DTSFBT**:PC71BM blends can be explained without needing a variable recombination reduction factor.[34]

Table 9.1 Mobilities of DPPBFu:PC71BM and DTSFBT:PC71BM blends at 295 K.

Donor	Condition	μ_h [m^2/Vs]	μ_e [m^2/Vs]	μ_d [m^2/Vs]
DPPBFu	As-Cast	3.4×10^{-9}	1.0×10^{-8}	1.0×10^{-8}
	Annealed	4.7×10^{-8}	1.6×10^{-7}	6.3×10^{-7}
DTSFBT	As-Cast	1.1×10^{-9}	9.4×10^{-9}	7.1×10^{-9}
	Annealed	2.2×10^{-8}	1.3×10^{-8}	3.5×10^{-8}
	DIO	4.6×10^{-8}	1.9×10^{-8}	4.6×10^{-8}

Table 9.2 Recombination parameters for DPPBFu:PC71BM and DTSFBT:PC71BM at 295 K.

Donor	Condition	γ_{pre}	k_L [m^3/s]	k_R [m^3/s]
DPPBFu	As-Cast	1	7.0×10^{-17}	7.0×10^{-17}
	Annealed	0.12	1.1×10^{-15}	1.3×10^{-16}
DTSFBT	As-Cast	1	5.5×10^{-17}	5.5×10^{-17}
	Annealed	1	1.8×10^{-16}	1.8×10^{-16}
	DIO	1	3.4×10^{-16}	3.4×10^{-16}

9.4 Conclusions

To conclude, whereby most studied systems in literature have exhibited reduced non-geminate recombination, observations for two small molecule systems with different chemical structures and solid state organization suggest that reduced recombination does not arise simply from favorable morphologies. In as-cast blends of **DPPBFu**:PC71BM and **DTSFBT**:PC71BM, the donor and acceptor molecules are intimately mixed, giving reduction factors that are ~ 1. This means that electrons and holes recombine following the Langevin equation.

After thermal annealing the two systems at 110 ºC, the hole, electron, and effective mobilities increase by about one order of magnitude. These changes in mobility occur along with significant changes in solid-state organization, where the donor and acceptor form crystalline domains and begin to phase segregate. For **DPPBFu**:PC71BM, the reduction factor reduces to 0.12 after thermal treatment. However, for **DTSFBT**:PC71BM the reduction factor remains 1 in spite of radical changes in solid-state morphology. Even after processing the **DTSFBT**:PC71BM blends from DIO, the reduction factor does not change and is again 1. This is contrary to reports that claim that desirable morphologies correlate with smaller reduction factors.

As for the origin of the reduction factor, it has been hypothesized that reduced recombination may original from a temperature activated carrier recombination event at the donor:acceptor interface.[6,36] In this situation, recombination of free carriers would be at first diffusion limited, but then have to traverse through a temperature-activated state. This type of behavior would emphasize the individual energetics and orientation of molecules at interfaces rather than the fraction or distribution of phases or crystals within a bulk film.[37]

The promise of this type of work is that by characterization of diverse BHJ systems of both polymer and small molecule types, along with various processing conditions, more insight can be drawn to correlate molecular design and morphologies with observed reduction factors. Ideally, if researchers could get control over the macroscopic electrical properties of BHJ solar cells, even better device performances could be realized.

9.5 Experimental Methods

Materials: Anhydrous chlorobenzene, chloroform, and 1,8-diiodooctane were bought from Acros Organics and used as received. **DPPBFu** and **DTSFBT** were purchased from 1-Material (Dorval, Canada). $PC_{71}BM$ was purchased from Solenne B. V. (Groningen, The Netherlands) and used as received.

Device and Film Fabrication: Corning glass substrates were scrubbed thoroughly with detergent and sonicated in acetone and isopropanol. For solar cell devices, the glass substrates were patterned with 140 nm of ITO. For solar cell devices, a 50 nm layer of PEDOT:PSS (H. C. Stark GmbH) coats the ITO. Following the cleaning procedure, patterned contacts consisting of 1 nm of Ti and 30 nm of Au were deposited (hole-only and double-carrier devices) onto the substrates in a thermal evaporator at a pressure of less than 1×10^{-6} torr. The Au substrates were treated to 30 min of UV/O_3. Directly afterwards, a 10 nm layer of MoO_x was thermally deposited atop the Au contacts a pressure of less than 1 x 10^{-6} torr. Electron-only devices were prepared using the same glass substrates followed by spin-coating of a 50 nm layer of PEDOT:PSS.[38] Atop the layer of PEDOT:PSS patterned contacts of 30 nm thick Al completes the bottom contact. Films of **DPPBFu**:PC71BM in the as-cast and annealed conditions were prepared according to reference 14. Films of **DTSFBT**:PC71BM in the as-cast, annealed, and DIO conditions were prepared according to reference 15. The 60 nm thick Au top contact (hole-only devices) or 5 nm Ca capped with 70 nm Al (solar cell, electron-only, double-carrier devices) were deposited in a thermal evaporator, also at a pressure of less than 1×10^{-6} torr.

Electrical Characterization: Room temperature *J–V* characteristics of the hole-only devices were measured using a Keithley 4200 semiconductor analyzer with the sample placed in a variable temperature probe station (Lake Shore Cryotronics, Inc.) and measured at a pressure of $< 1 \times 10^{-6}$ torr. Solar cells were characterized under simulated 1000 W/m^2 AM1.5G irradiation from a 300 W Xe arc lamp with an AM1.5G global filter and with a Keithley 2400 source-measure-unit. Film thicknesses were determined using an Ambios XP-100 profilometer.

9.6 References

(1) Shockley, W.; Queisser, H. J. *J. Appl. Phys.* **2004**, *32*, 510–519.

(2) Proctor, C. M.; Kuik, M.; Nguyen, T.-Q. *Prog. Polym. Sci.* **2013**, *38*, 1941–1960.

(3) Veldman, D.; Meskers, S. C. J.; Janssen, R. A. J. *Adv. Funct. Mater.* **2009**, *19*, 1939–1948.

(4) Vandewal, K.; Tvingstedt, K.; Gadisa, A.; Inganäs, O.; Manca, J. V. *Nat. Mater.* **2009**, *8*, 904–909.

(5) Sze, S. M. *Physics of semiconductor devices*; 3rd ed.; Wiley-Interscience: Hoboken, N.J, 2007.

(6) Wetzelaer, G.-J. A. H.; Van der Kaap, N. J.; Koster, L. J. A.; Blom, P. W. M. *Adv. Energy Mater.* **2013**, *3*, 1130–1134.

(7) Groves, C.; Greenham, N. *Phys. Rev. B* **2008**, *78*, 155205.

(8) Langevin, M. P. *Ann. Chim. Phys.* **1903**, 433.

(9) Kniepert, J.; Lange, I.; van der Kaap, N. J.; Koster, L. J. A.; Neher, D. *Adv. Energy Mater.* **2014**, *4*, 1301401.

(10) Clarke, T. M.; Peet, J.; Denk, P.; Dennler, G.; Lungenschmied, C.; Mozer, A. J. *Energy Environ. Sci.* **2012**, *5*, 5241.

(11) Albrecht, S.; Janietz, S.; Schindler, W.; Frisch, J.; Kurpiers, J.; Kniepert, J.; Inal, S.; Pingel, P.; Fostiropoulos, K.; Koch, N.; Neher, D. *J. Am. Chem. Soc.* **2012**, *134*, 14932–14944.

(12) Murthy, D. H. K.; Melianas, A.; Tang, Z.; Juška, G.; Arlauskas, K.; Zhang, F.; Siebbeles, L. D. A.; Inganäs, O.; Savenije, T. J. *Adv. Funct. Mater.* **2013**, *23*, 4262–4268.

(13) Juška, G.; Genevičius, K.; Nekrašas, N.; Sliaužys, G. *Phys. Status Solidi C* **2010**, *7*, 980-983.

(14) Walker, B.; Tamayo, A. B.; Dang, X.-D.; Zalar, P.; Seo, J. H.; Garcia, A.; Tantiwiwat, M.; Nguyen, T.-Q. *Adv. Funct. Mater.* **2009**, *19*, 3063–3069.

(15) Van der Poll, T. S.; Love, J. A.; Nguyen, T.-Q.; Bazan, G. C. *Adv. Mater.* **2012**, *24*, 3646–3649.

(16) Kyaw, A. K. K.; Wang, D. H.; Gupta, V.; Zhang, J.; Chand, S.; Bazan, G. C.; Heeger, A. J. *Adv. Mater.* **2013**, *25*, 2397–2402.

(17) Cambarau, W.; Viterisi, A.; Ryan, J. W.; Palomares, E. *Chem. Commun.* **2014**, *50*, 5349-5351.

(18) Walker, B.; Tamayo, A.; Duong, D. T.; Dang, X.-D.; Kim, C.; Granstrom, J.; Nguyen, T.-Q. *Adv. Energy Mater.* **2011**, *1*, 221–229.

(19) Gupta, V.; Kyaw, A. K. K.; Wang, D. H.; Chand, S.; Bazan, G. C.; Heeger, A. J. *Sci. Rep.* **2013**, *3*, 1965.

(20) Sharenko, A.; Kuik, M.; Toney, M. F.; Nguyen, T.-Q. *Adv. Funct. Mater.* **2014**, DOI: 10.1002/adfm.201304100.

(21) Love, J. A.; Proctor, C. M.; Liu, J.; Takacs, C. J.; Sharenko, A.; van der Poll, T. S.; Heeger, A. J.; Bazan, G. C.; Nguyen, T.-Q. *Adv. Funct. Mater.* **2013**, *23*, 5019–5026.

(22) Perez, L. A.; Chou, K. W.; Love, J. A.; van der Poll, T. S.; Smilgies, D.-M.; Nguyen, T.-Q.; Kramer, E. J.; Amassian, A.; Bazan, G. C. *Adv. Mater.* **2013**, *25*, 6380–6384.

(23) Juška, G.; Arlauskas, K.; Sliaužys, G.; Pivrikas, A.; Mozer, A. J.; Sariciftci, N. S.; Scharber, M.; Österbacka, R. *Appl. Phys. Lett.* **2005**, *87*, 222110.

(24) Pivrikas, A.; Juška, G.; Mozer, A.; Scharber, M.; Arlauskas, K.; Sariciftci, N.; Stubb, H.; Österbacka, R. *Phys. Rev. Lett.* **2005**, *94,* 176806.

(25) Wetzelaer, G. A. H.; Kuik, M.; Nicolai, H. T.; Blom, P. W. M. *Phys. Rev. B* **2011**, *83*, 165204.

(26) Mandoc, M. M.; Kooistra, F. B.; Hummelen, J. C.; de Boer, B.; Blom, P. W. M. *Appl. Phys. Lett.* **2007**, *91*, 263505.

(27) Mott, N. F.; Gurney, R. W. *Electronic processes in ionic crystals*; Dover: New York, NY, 1964.

(28) Blom, P. W. M.; Tanase, C.; Leeuw, D. M. de; Coehoorn, R. *Appl. Phys. Lett.* **2005**, *86*, 092105.

(29) Kyaw, A. K. K.; Wang, D. H.; Luo, C.; Cao, Y.; Nguyen, T.-Q.; Bazan, G. C.; Heeger, A. J. *Adv. Energy Mater.* **2014**, *4*, 1301469.

(30) Schiff, E. *Sol. Energy Mater. Sol. Cells* **2003**, *78*, 567–595.

(31) Kyaw, A. K. K.; Wang, D. H.; Wynands, D.; Zhang, J.; Nguyen, T.-Q.; Bazan, G. C.; Heeger, A. J. *Nano Lett.* **2013**, *13*, 3796–3801.

(32) Mark, P.; Helfrich, W. *J. Appl. Phys.* **1962**, *33*, 205.

(33) Craciun, N. I.; Zhang, Y.; Palmaerts, A.; Nicolai, H. T.; Kuik, M.; Kist, R. J. P.; Wetzelaer, G. A. H.; Wildeman, J.; Vandenbergh, J.; Lutsen, L.; Vanderzande, D.; Blom, P. W. M. *J. Appl. Phys.* **2010**, *107*, 124504.

(34) Sun, Y.; Welch, G. C.; Leong, W. L.; Takacs, C. J.; Bazan, G. C.; Heeger, A. J. *Nat. Mater.* **2011**, *11*, 44–48.

(35) Proctor, C.; Albrecht, S.; Neher, D.; Nguyen, T.-Q. *Adv. Energy Mater.* **2014**, DOI: 10.1002/aenm.201400230.

(36) Ferguson, A. J.; Kopidakis, N.; Shaheen, S. E.; Rumbles, G. *J. Phys. Chem. C* **2011**, *115*, 23134–23148.

(37) Savoie, B. M.; Rao, A.; Bakulin, A. A.; Gelinas, S.; Movaghar, B.; Friend, R. H.; Marks, T. J.; Ratner, M. A. *J. Am. Chem. Soc.* **2014**, *136*, 2876-2884.

(38) Steyrleuthner, R.; Bange, S.; Neher, D. *J. Appl. Phys.* **2009**, *105*, 064509.

10.0 Conclusions & Outlook

This thesis describes a variety of experiments done in order to help understand the optical and electronic properties of various novel π-conjugated molecules for application in a wide variety of device architectures.

Chapter 1 gives a general overview of organic electronics will be given – starting with a primer on the materials that make this field possible. Then, brief summaries will be presented on charge transport in organic semiconductors as well as the basic operation of a variety of device structures including light-emitting diodes, solar cells, and field-effect transistors. The end of this chapter concludes with a brief summary on basic design principles to achieve complete control over energetic band gaps in organic semiconductors.

Chapter 2 describes the way that all samples and devices in this thesis were prepared and evaluated will be described in detail. Among the experimental techniques described and used in this thesis include: UV-visible absorption spectroscopy, photoluminescence spectroscopy, photoluminescence lifetime measurements, photoluminescence quantum yield measurements, atomic force microscopy (AFM), conducting AFM (c-AFM), x-ray diffraction, ultraviolet/X-ray photoelectron spectroscopy, thermal evaporation, impedance spectroscopy, and conventional current-voltage measurements. Electronic devices fabricated include: polymer light-emitting diodes (PLEDs), polymer and small molecule photovoltaics, polymer field-effect transistors, and single-carrier diodes.

In Chapter 3, the optical and electrical characterization of a novel small-molecule π-conjugated electrolyte, a quinacridone salt, is described. The absorption and photoluminescent properties of the molecule were probed to evaluate the molecules' behavior in the solution and solid states. AFM was used to probe the surface topology of the quinacridone salts atop the emissive layer of the PLED. Electron-only devices were fabricated to evaluate the electron mobility of the materials. These data were then correlated to polymer light-emitting diode behavior where the quinacridone salt acts as a electron injection layer, improving device performance by enhancing the light output. This work was published in *The Journal of Physical Chemistry C*.

In Chapter 4, recycled deoxyribonucleic acid (DNA) from the waste products of the Japanese salmon catch was used as an electron injection layer in PLEDs. The current-voltage and luminescence-voltage behavior was measured, along with the electroluminescence time response. In addition, the surface topology and conductivity of the DNA layers atop the emissive layer of the PLED was also probed by AFM and c-AFM. This work was published in *The Journal of The American Chemical Society*.

In Chapter 5, the use of processing additives, that had become a standard processing condition for many organic photovolatics, was extended for use in single-component field-effect transistors. The dependence of the field-effect transistor device figures of merit (such as mobility and threshold voltage) on additive concentration was evaluated. In this work, various processing additives were screened to evaluate which additive gave the best field-effect transistor performance. The surface topology of the resultant polymer layers as a function of additive concentration was also evaluated. This work was submitted as a United States patent, in cooperation with Mitsubishi Chemical Corporation (Japan).

In Chapter 6, the regioregular polymers containing entantiopure and racemic side chains were compared side-by-side in field-effect transistors. The absorption and aggregation properties were studied using UV-visible spectroscopy and circular dichroism. Atomic force microscopy confirmed the presence of fibers that were associated with formation of chiral aggregates. Finally, the unique aggregation behavior extended to the electrical properties of the films, as determined using field-effect transistors. In short, the field-effect mobility could be increased by a factor two, while lowering the threshold voltage. This work was submitted as a United States patent, in collaboration with Mitsubishi Chemical Corporation (Japan).

In Chapter 7, as a proof of concept, Lewis acids were used to not only modulate the absorption characteristics of a high quantum-yield π-conjugated polymer, but also the photoluminescent and electroluminescent properties. Using Lewis acids, the energetic band-gap of the polymer could be effectively tuned, negating the need for rigorous synthesis of various polymer structures to arrive at the desired band gaps. The most important part of this work was extending this methodology beyond solution and film studies, but also demonstrating this approach's feasibility in *working* devices. This work was published in *Angewandte Chemie International Edition*.

In Chapter 8, the electrical properties of a Lewis acid modified polymer were evaluated using careful measurements of single-carrier diodes as a function of Lewis acid loading. The measurements included optical absorption, photoluminescence, and temperature dependent current-voltage and impedance measurements. This work was published in *Advanced Materials*.

Finally, in Chapter 9, the electrical properties of two small molecule bulk heterojunction systems were evaluated using a novel device structure that improved device yields and circumvented potential problems for hole-injection and series resistance at the anode. Thorough electrical characterization of hole-only, electron-only, and double-carrier (dark) diodes allowed for the simple calculation of recombination rates and Langevin reduction factors. This work showed that Langevin reduction factors *cannot* necessarily be correlated with changes in solid-state organization and that these Langevin reduction factors may be the result of complex donor-acceptor interaction in the film. This work is now published in *Advanced Energy Materials*.

The work presented in this thesis comprehensively shows the broad applicability and problems that can be solved in organic electronics. Clever and simple chemistry often led to interesting and novel properties with significant promise for future application. Even more importantly, the wealth of information and perspective that can be achieved using relatively simple characterization techniques, such as single carrier diodes and temperature or light intensity dependences cannot be underestimated.